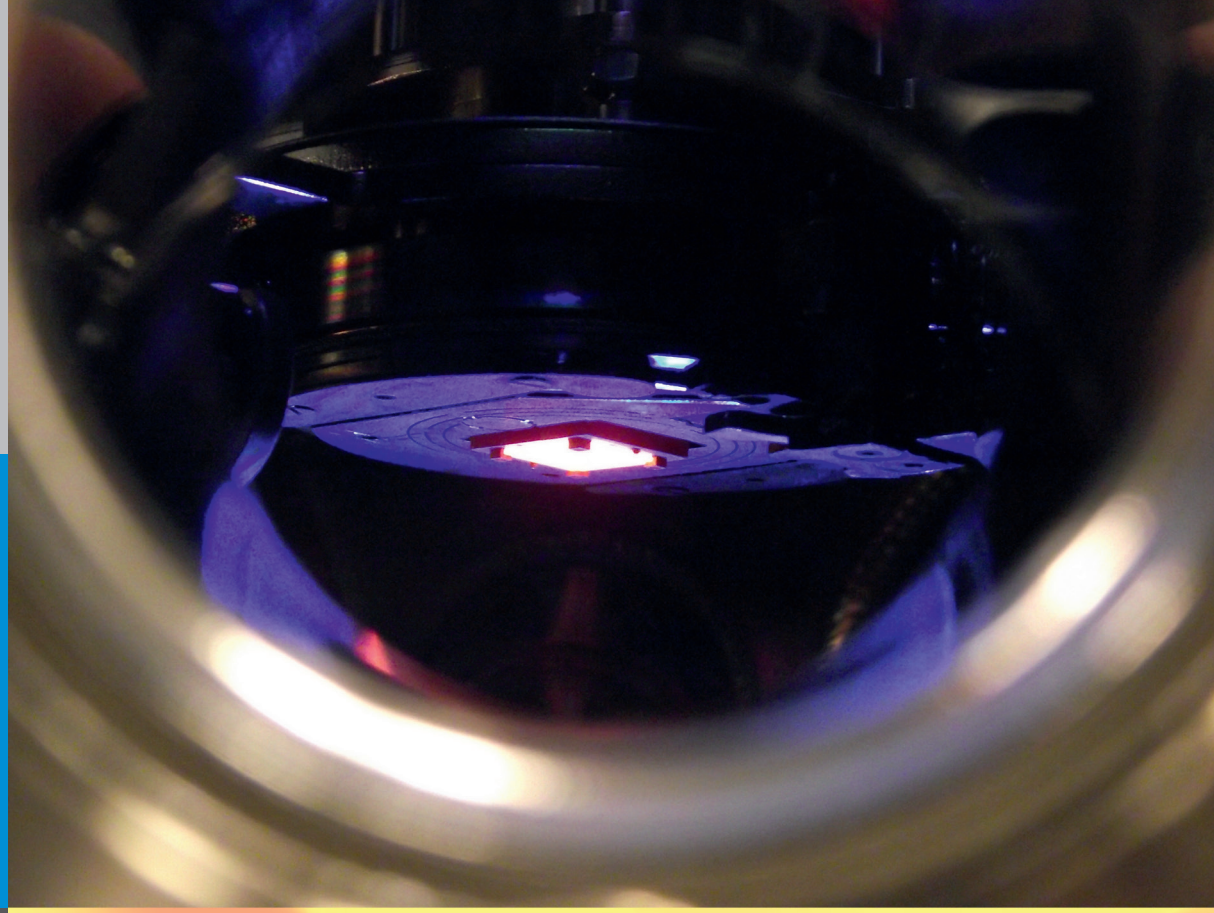

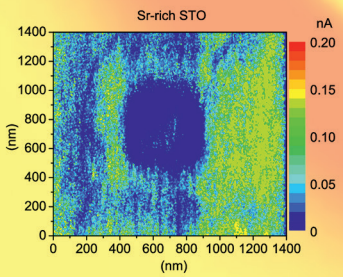


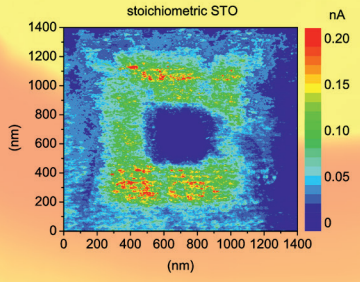


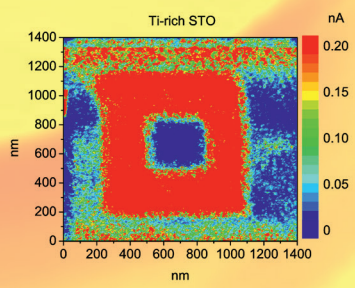


# Defect Engineering of $SrTiO_3$ thin films for resistive switching applications

Sebastian Wicklein

JÜLICH
FORSCHUNGSZENTRUM

Member of the Helmholtz Association

Schriften des Forschungszentrums Jülich
Reihe Information Band / Volume 35

Forschungszentrum Jülich GmbH
Peter Grünberg Institute (PGI)
Elektronische Materialien (PGI-7)

# Defect Engineering of $SrTiO_3$ thin films for resistive switching applications

Sebastian Wicklein

Schriften des Forschungszentrums Jülich
Reihe Information

Band / Volume 35

ISSN 1866-1777

ISBN 978-3-89336-963-8

Bibliographic information published by the Deutsche Nationalbibliothek.
The Deutsche Nationalbibliothek lists this publication in the Deutsche Nationalbibliografie; detailed bibliographic data are available in the Internet at http://dnb.d-nb.de.

Publisher and Distributor: Forschungszentrum Jülich GmbH
Zentralbibliothek
52425 Jülich
Tel: +49 2461 61-5368
Fax: +49 2461 61-6103
Email: zb-publikation@fz-juelich.de
www.fz-juelich.de/zb

Cover Design: Grafische Medien, Forschungszentrum Jülich GmbH

Printer: Grafische Medien, Forschungszentrum Jülich GmbH



Schriften des Forschungszentrums Jülich
Reihe Information, Band / Volume 35

D 8 (Diss., Christian-Albrechts-Universität zu Kiel, 2013)

ISSN 1866-1777
ISBN 978-3-89336-963-8

The complete volume is freely available on the Internet on the Jülicher Open Access Server (JUWEL) at www.fz-juelich.de/zb/juwel

## ABSTRACT

As a matter of fact, the importance of (transition) metal oxides for modern applications in the field of energy and information technology (IT) for e.g. novel energy storage systems and solid state electronic devices is increasing. Previous studies discovered the importance of defects in an oxide for their functionality and emphasized the impact of stoichiometry on the oxide performance.

A new field of interest of the memory technology sector is the so-called resistive switching phenomena where a voltage stimulus causes a thin oxide (≤ 10nm) to change its resistance state from a high resistance state to a low resistance state and back. So called resistive RAM (ReRAM or RRAM) are deemed to be the future replacement (2015) for contemporary FLASH memory technology due to its extremely low energy consumption, its very fast read/write time (ns) and its possible node size <10nm.

A key challenge for the investigation of oxides and their electronic properties is the management and controlled incorporation of defects in the thin film oxide.

Within this work, $SrTiO_3$ was used as an oxide model material and was deposited by pulsed laser deposition (PLD) onto doped and undoped $SrTiO_3$ single crystals to investigate the formation of defects as a function of the process parameters. By combining structural and chemical thin film analysis with detailed PLD plume diagnostics and modeling of the laser plume dynamics, it was possible to elucidate the different physical mechanisms determining the stoichiometry of $SrTiO_3$ during PLD. Deviations between thin film and target stoichiometry are basically a result of two effects, namely, incongruent ablation and preferential scattering of lighter ablated species during their motion towards the substrate in the $O_2$ background gas. It is shown that the $SrTiO_3$ system reacts to a non-stoichiometry with the systematic incorporation of titanium and strontium vacancies which could be detected by positron annihilation lifetime spectroscopy. The role of extrinsic dopands such as Fe is shown to have more complicated effects on the $SrTiO_3$ system than portrayed by theoretical considerations.

The effect of defects on the resistive switching properties of $SrTiO_3$ was investigated by local conductivity AFM. Defect engineered $SrTiO_3$ depict variations of the resistive switching properties for different defect constellations within the system. More stable resistance switching was achieved for systems with an increased defect content. The mechanism of the resistance change was attributed to the rearrangement of oxygen vacancies within $SrTiO_3$ and a theory devised where the rearrangement of the oxygen vacancies causes a reversible transition of the oxide from p- to n-type. Whereas a p-type oxide depicts a high resistance and a n-type oxide a low resistance.

## KURZFASSUNG

Seit einiger Zeit hat die Bedeutung von (Übergangs-) Metalloxiden für moderne Anwendungen im Bereich der Energietechnik oder der Informationsverarbeitung (IT) für neuartige Energiespeicher Systeme oder Halbleiterbauteile zugenommen. Kürzlich präsentierte Untersuchungen haben gezeigt, dass Defekte im Oxid eine Wichtige Rolle für deren Funktionalität spielen, und über die Stöchiometrie des Oxids komntroliert werden können.

Ein neuer Interessenbereich der IT Branche ist das sogenannte Phänomen des Widerstands-schaltens. Hiebei erzeugt eine Spannungsstimulus eine reversible Widerstandsänderung einer dünnen Oxidschicht (~10nm). Diese kann von einem hoch-homigen Zustand in einen nieder-ohmigen Zustand überführt werden und wieder zurück. Sogenannte Widerstands-Speicherbausteine (ReRAM, RRAM) werden also zukünftigen Ersatz für zeitgenössische FLASH Speicherbausteine angesehen aufgrund ihres sehr geringen Energieverbrauchs, schnellen Schreib- und Auslesezeiten und der sehr kleinen Bausteingröße (~10nm).

Eine wichtige Herausforderung für die Untersuchung der elektronischen Eigenschaften ist das sog. Defekt Management und der damit verbundene kontrollierte Einbau von Defekten in das Oxid.

Im Rahmen dieser Arbeit wurde $SrTiO_3$ als Modelmaterial eingesetzt und mittels gepulster Laserablation (PLD) auf dotierte und un-dotierte $SrTiO_3$-Einkristalle abgeschieden. Dabei wurde die Entstehung von Defekten als Folge unterschiedlicher Prozessparameter untersucht. Durch die Kombination von Strukturanalysemethoden und chemischen Analysemethoden und die Anwendung von sog. „plume" Betrachtungen wie optische Emissionsspektroskopie sowie mittels Modellrechnungen für die Plume-dynamik die Mechanismen entschlüsselt werden, die die Stöchiometrie des Systems bestimmen.

Die resultierenden Abweichungen zwischen Target- und Filmstöchiometrie sind das Resultat von von zwei Effekten. Zum einen die inkongruente Ablation des Targetmaterials als Funktion der Laserenergie, und zum anderen die Streuung von leichte Plume-Partikelen wie z.B. Ti während der Flugphase durch das Hintergrundgas ($O_2$).

Es wurde anhand von Positron-Annihilationsexperimenten gezeigt, dass das $SrTiO_3$-System mit dem systematischen Einbau von Titan- und Strontiumleerstellen auf eine Nichtstöchiometrie reagiert. Die Rolle und der Effekt von extrinsischen Dotierungen wie z.B. Eisen auf das $SrTiO_3$-system zeigte sich komplizierter als von theoretischen Modellen vorhergesagt.

Der Effekt solcher Defekte auf das resistive Schalten wurde mittels lokaler Leitfähigkeitsuntersuchungen (LC-AFM) analysiert. $SrTiO_3$, mit gezielt eingebauten Defekten, zeigte eine deutlich Abhängigkeit des Schaltverhaltens von der Defektkonstellation. Stabiles Schalten wurde in Systemen mit erhöhtem Defektgehalt beobachtet. Der Schaltmechanismus wurde auf die Umordung von Sauerstoffleerstellen zurückgeführt, die eine Umwandlung von p-leitendem SrTiO3 in ein n-leitendes SrTiO3 ebewirken. Eine p-Leitfaehigkeit zeigt einen hohen Widerstand wohingegen eine n-Leitfähigkeit einen geringen Widerstand zeigt.

# Contents

# 1 Introduction

Complex transition metal oxides are becoming more attractive for innovative applications due to their large variety of remarkable physical properties such as high temperature superconductivity, piezoelectricity, ferroelectricity, magnetism, and multiferroicity and resistance switching phenomena. These physical properties are strongly influenced by the defect structure and the stoichiometry of the oxide respectively. Therefore, the understanding and control over the formation of defects and stoichiometry is key for investigating the fundamentals of the physical properties of such oxides.

A common way to deposit such complex oxides for scientific investigations is pulsed laser deposition (PLD). Although it was generally accepted that PLD yields a stoichiometric transfer of target species to the substrate, over time, evidence was created that this is actually not the case and that process parameters strongly impact the stoichiometry and the physical properties of the oxide [1, 2]. Moreover, it was observed that the PLD oxide thin films comprise point defects in the anion and cation sub-lattice [3, 4] which are responsible for the alteration of the physical properties of the oxide [5]. Cation vacancies usually act as acceptors and tend to trap charge carriers and can influence and even suppress donor doping activity as demonstrated in [6, 7]. Therefore it is imperative to determine the underlying mechanisms that are responsible for the defect formation in complex oxide thin films deposited by PLD.

Although defects are inherently deemed as disadvantageous for most applications of complex oxides there is a specific effect where defects in the oxide are essential which is called "resistive switching". Here, a thin oxide (~10nm – 20nm) is sandwiched between two metallic electrodes, forming a two-terminal cell, and the resistance of the oxide can be decreased and increased again by applying a voltage to the electrodes. This effect is especially distinct for transition metal-oxides where a resistance change is caused due to a valence change or a controlled electrical breakdown.

Earlier works have [8-10] discussed and demonstrated that point defects in the complex oxide are regarded as a premise for the RS phenomenon and extended defects play the key role in the RS effect. The resistance switching (RS) phenomenon is an intriguing process that is pursued by many parties in the memory industry. So called resistance RAM (RRAM or ReRAM), based on this resistance change, are considered to revolutionize the future memory technology due to their low energy consumption and short (ns) response and trigger times.

Hence, questions regarding the interaction of these two defect types need to be answered to further elucidate the RS mechanism. Also, to incorporate defects into the oxides in a controlled fashion is still a challenge.

**UHV-Cluster engineering**

Although there is a plethora of complex oxides and other materials to be investigated for many different applications, their common denominator is their need for in-situ investigation of their physical properties and the deposition process. Especially for the investigation of the RS effect, it is imperative to preserve engineered oxidation states in the system to make out the switching mechanism.

Therefore, a UHV-cluster was setup to allow a precise investigation of complex material systems on the nanoscale without the perturbation of the material system from external parameters such as ambient oxygen, particles and chemical adsorbates. The UHV-cluster system comprises flexible deposition tools such as PLD, sputtering and e-beam PVD to apply oxides, nitrides, metals and other material combinations. For in-situ chemical analysis, XPS and PEEM technology is attached to the system along with a standard SEM. Topological and electrical properties, such as their resistive switching properties can be investigated in-situ by a SPM tool that comprises various AFM and STM techniques, also in UHV.

**Defect engineering**

By so-called defect engineering the deposition process is investigated with respect to the resulting defect structure of the oxide. For that reason, critical process parameters like oxygen background gas pressure ($pO_2$), laser fluence ($f_L$), target to substrate distance ($D_{TS}$) and substrate temperature ($T_S$) were systematically varied and the resulting defect structure analyzed. The origin of the defects in the oxide was correlated to the deposition process conditions by applying in-situ investigation methods such as reflection high energy electron diffraction (RHEED) or optical emission spectroscopy (OES) with fast imaging of the PLD plume. For defect analysis several methods were employed such as x-ray diffraction (XRD) and positron lifetime annihilation lifetime spectroscopy (PALS) and x-ray photoelectron spectroscopy (XPS).

**Resistance switching properties**

The oxide thin films were investigated in-situ for their RS properties by local conductivity (LC-AFM) and ex-situ by so-called metal/oxide/metal (MIM) structures. For the in-situ investigations of the RS properties, the specimen was transferred under UHV conditions to the UHV LC-AFM after deposition. Post annealing processes, quenching and the transfer in UHV environment allowed freezing-in states into the oxide and analyzing their impact on the RS properties without the interference from the environment.

**Contents**

Chapter 2 portrays the necessary physical and chemical background of a complex oxide system. Especially a brief introduction to the so-called defect chemistry is given. In chapter 3 the UHV cluster system and its components are described and shown. Within chapter 4 the experimental methods, utilized for the defect engineering and investigation of the physical and chemical properties as well as the in-situ deposition process, are explained in detail. The defect engineering by PLD process management is discussed in chapter 5 where the effect of the single process parameters is deciphered. The effect of doping the oxide ($SrTiO_3$) with Fe is presented in chapter 6 where the defect structure of Fe doped STO is elucidated. The effect of the defects

on the growth of the oxide is then portrayed in chapter 7 where it is shown that with the help of in-situ investigation methods, such as RHEED, the defect structure of the thin film can be deduced during the growth. The effect of the defect structure on the resistive switching properties is demonstrated in chapter 8 where the in-situ investigation by LC-AFM is compared to ex-situ studies. The final conclusion are given in chapter 9 where the major aspects of all findings are evaluated.

# 2 Background

Within this chapter the fundamentals are considered that are necessary to discuss the observations presented in the following chapters.

## 2.1 $SrTiO_3$

Strontium titanate, $SrTiO_3$ (STO), is a ternary transition metal oxide with a perovskite structure of **$ABO_3$**. STO exhibits a cubic crystal structure (space group: Pm3m) at room temperature (300K) with (a = b = c) as shown in Figure 2-1 with the $Ti^{4+}$ ion in the center of the unit cell. In the <100> direction the crystal is made up of alternating $TiO_2$ and SrO planes. The center $Ti^{4+}$ ion is surrounded by a sixfold coordination of $O^{2-}$ ions forming a $TiO_6$ octahedra that exhibits a weak covalent bonding character. This is due to hybridized O-2p states bonding to Ti-$3d^0$ states [11]. Because the $Sr^{2+}$ and $O^{2-}$ ions exhibit ionic bonding character the $SrTiO_3$ crystal has a mixed ionic-covalent bonding character.

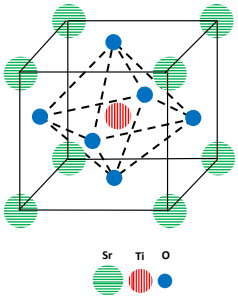


| Physcial property | | Unit | Value |
|---|---|---|---|
| Lattice constant at RT | **a** | [nm] | 0.3905 |
| Dielectric constant | **ε** | | 300 |
| Band gap | **$E_g$** | [eV] | 3.25 |
| Thermal expansion | | [Å/°C] | $9.5 \cdot 10^{-6}$ |
| Density | **ρ** | [g/cm³] | 5.12 |
| Thermal conductivity | | [W/m·K] | 12 |
| Young's modulus | **E** | [GPa] | 189.7 |
| Poission's ratio | **ν** | | 0.232 |

**Figure 2-1:** Unit cell of $SrTiO_3$ and the physical properties at $T_S$ = 300K.

## 2.2 Defect chemistry of $SrTiO_3$

Stoichiometry variations and defects play a crucial role respectively in complex oxides and determine their physical properties. Especially the electrical properties of $SrTiO_3$ depend on its defect structure. For that reason, Schottky defects will be considered in particular since the formation of Frenkel defects (interstitials) are energetically not favorable for STO.

By utilizing the so called defect chemistry model by [12] and Kröger-Vink notation [13, 14] the equations based on charge neutrality, thermodynamic equilibrium and law of mass action by [15] are considered in the following. The constituents responsible for the electrical characteristics in $SrTiO_3$ are listed with their chemical and their according Kröger-Vink notation below and will be used throughout the following chapters.

| Narrative | Constituent | Chemical notation | Kröger-Vink |
|---|---|---|---|
| Atoms on a regular lattice site | Oxygen ion | $O^{2-}$ | $O_O^x$ |
| | Strontium ion | $Sr^{2+}$ | $Sr_{Sr}^x$ |
| | Titanium ion | $Ti^{4+}$ | $Ti_{Ti}^x$ |
| Anion Vacancy (Schottky defect) | Oxygen vacancy | $O_{3-\delta}^{2-}$ | $V_O^{\bullet\bullet}$ |
| Cation Vacancies (Schottky defect) | Strontium vacancy | $Sr_{1-\delta}^{2+}$ | $V_{Sr}^{//}$ |
| | Titanium vacancy | $Ti_{1-\delta}^{4+}$ | $V_{Ti}^{////}$ |
| Intrinsic free charge carriers | Electron | n / $e^-$ | $e^/$ |
| | Hole | p / $O^0$ | $h^\bullet$ |
| Extrinsic charge carriers | Donor | i.e. $Nb_{Ti}^{5+}$, $La_{Sr}^{3+}$ | $D^\bullet$ |
| | Acceptor | i.e. $Fe_{Ti}^{3+}$, $In_{Ti}^{3+}$, $Sc_{Ti}^{3+}$, $V_{Ti}^{3+}$ | $A^/$ |

**Table 2-1:** Chemical and Kröger-Vink notation of lattice sites, charge carriers and Schottky-type defects in $SrTiO_3$. The symbols here within denote in the exponent a *neutral charge* $^x$, a *negative charge* $^/$ and a *positive charge* $^\bullet$. The subscript in the Kröger-Vink notation indicates the lattice site.

It is important to note, that a un-doped STO system is inherently considered as acceptor doped (A′) due either i.e. background impurities (Fe, Cr, V, etc.) or cation vacancies ( $V_{Sr}''$, $V_{Ti}''''$ ) in the system which arise during the manufacturing process of the $SrTiO_3$ specimen.
Therefore only two cases, namely, acceptor doped STO and donor doped STO are addressed in the following.

### 2.2.1 Defect chemical equilibrium & reactions for $SrTiO_3$

As an ionic crystal, $SrTiO_3$ is dependent on charge neutrality which entails the (re-) arrangement of charged ions, defects and free charge carriers as a consequence of an extrinsic impetus which can be a function of oxygen partial pressure $p_{O2}$, temperature $T$ or impurity atoms. The charge neutrality condition for bulk STO is expressed by the following equation, see also [12].

$$e^/ + 2\left[V_{Sr}^{//}\right] + 4\left[V_{Ti}^{////}\right] + \left[A^/\right] = h^\bullet + 2\left[V_O^{\bullet\bullet}\right] + \left[D^\bullet\right] \quad \textbf{(2.1-a)}$$

$$n + \left[A^/\right] = p + 2\left[V_O^{\bullet\bullet}\right] \quad \textbf{(2.2-b)}$$

The equation exemplifies that the incorporation of acceptors in general and the formation of cation vacancies in particular is possible if electrically compensated by e.g. oxygen vacancies. This rather simple rule of charge neutrality however, cannot be utilized solely to determine defect chemical reactions in STO.

In the STO compound, simple electronic compensation mechanisms are feasible at room temperature that do not require a chemical stimulus or ionic compensation, such as the formation of electron-hole pairs or the ionization of oxygen vacancies.

$$e^{/} + h^{\bullet} \leftrightarrow 0 \qquad \textbf{(2.3-a)}$$

$$V_O^x \leftrightarrow V_O^{\bullet\bullet} + 2e^{/} \qquad \textbf{(2.4-b)}$$

By external excitation an electron-hole pair can be created with a free hole $h^{\bullet}$ in the valence band where the electron $e^{/}$ is excited either into the conduction band or trapped by an acceptor within the band gap. Due to their small ionization energy [16] oxygen vacancies are usually doubly ionized at room temperature where the electron is excited (~0.22eV) into the conduction band.

Defect chemical reactions that involve rearrangements of ions in the anion and/or cation sublattice are either *Redox-reactions* where oxygen is exchanged between the STO crystal and the environment or the formation or annihilation of cationic defects which is described by the so called *Schottky-disorder-reaction* or the *Schottky-defect-equilibrium* also described in [17].
The thermodynamic equilibrium of these defect chemical reactions can be expressed by the so called law of mass action (LMA) according to [12] with following expression,

| Chemical reaction | Mass action | |
|---|---|---|
| $aA + bB \leftrightarrow cC + dD$ | $\frac{[C]^c \cdot [D]^d}{[A]^a \cdot [B]^b} = K_0 \exp\left(-\frac{\Delta H}{k_B T}\right)$ | **(2.5)** |

The defect chemical reactions and the according mass actions for STO and Fe-doped STO according to [12, 18] [17, 19]and [20] are listed below.
By the mass actions it is possible to derive the direction of the chemical reaction for equilibrium and the resulting formation of ionic species. For example the reduced Schottky reaction reveals in the mass action that the incorporation of oxygen vacancies ($V_O^{\bullet\bullet}$) results in the suppression of the formation of strontium vacancies $V_{Sr}''$ when SrO phase/plane is formed. This indicates that the growth of a defect-free SrO-phase is facilitated in a reducing environment. The thermal activation of the reduction and oxidation reaction is for $T \geq 750K$ and the Schottky reaction needs a thermal activation of $T \geq 1250K$.
Acceptor doping, for instance by Fe can lead to p-type as well as n-type behavior depending on the oxygen partial pressure [17] due to different compensation mechanism of $Fe^{4+}/Fe^{3+}$ and $Fe^{3+}/Fe^{2+}$.

| Narrative | Defect-Chemical-Reaction | Mass Action | |
|---|---|---|---|
| Electron-Hole generation | $0 \leftrightarrow e' + h^{\bullet}$ | $n \cdot p = N_e(T) \cdot N_p(T) \exp\left(-\frac{E_g(T)}{k_B T}\right)$ | (2.6) |
| Reduction | $O_O^x \leftrightarrow \frac{1}{2} O_2 + V_O^{\bullet\bullet} + 2e'$ | $p(O_2)^{1/2} \cdot \left[V_O^{\bullet\bullet}\right] \cdot n^2 = K_0^{red} \exp\left(-\frac{\Delta H_{red}}{k_B T}\right)$ | (2.7) |
| Oxidation | $\frac{1}{2} O_2 + V_O^{\bullet\bullet} \leftrightarrow O_O^x + 2h^{\bullet}$ | $\frac{p^2}{(pO_2)^{1/2} \cdot \left[V_O^{\bullet\bullet}\right]} = K_0^{ox} \exp\left(-\frac{\Delta H_{ox}}{k_B T}\right)$ | (2.8) |
| Schottky reaction | $Sr_{Sr}^x + Ti_{Ti}^x + 3O_O^x \leftrightarrow V_{Sr}'' + V_{Ti}'''' + 3V_O^{\bullet\bullet} + SrTiO_3$ | $\left[V_{Sr}''\right] \cdot \left[V_{Ti}''''\right] \cdot \left[V_O^{\bullet\bullet}\right]^3 = K_0^S \exp\left(-\frac{\Delta H_S}{k_B T}\right)$ | (2.9) |
| Reduced Schottky reaction | $Sr_{Sr}^x + O_O^x \leftrightarrow V_{Sr}'' + V_O^{\bullet\bullet} + (SrO)_{secondary\text{-}phase}$ | $\left[V_{Sr}''\right] \cdot \left[V_O^{\bullet\bullet}\right] = K_0^{RS} \exp\left(-\frac{\Delta H_{RS}}{k_B T}\right)$ | (2.10) |
| Acceptor (Fe) doping | $Fe_{Ti}^x \leftrightarrow Fe_{Ti}' + h^{\bullet}$ (p-type) | $p \cdot \left[Fe_{Ti}'\right] = K_0^{Fe} \exp\left(-\frac{\Delta H_{Fe}}{k_B T}\right)$ | (2.11) |
| | $Fe_{Ti}^x \leftrightarrow Fe_{Ti}'' + V_O^{\bullet\bullet}$ (n-type) | $\left[V_O^{\bullet\bullet}\right] \cdot \left[Fe_{Ti}''\right] = K_0^{Fe} \exp\left(-\frac{\Delta H_{Fe}}{k_B T}\right)$ | (2.12) |
| Donor (Nb) doping | $Nb_{Ti}^x \leftrightarrow Nb_{Ti}^{\bullet} + e'$ (free) | $n \cdot \left[Nb_{Ti}^{\bullet}\right] = K_0^{Nb} \exp\left(-\frac{\Delta H_{Nb}}{k_B T}\right)$ | (2.13) |
| | $Nb_{Ti}^x \leftrightarrow Nb_{Ti}^{\bullet} + A'$ (trapped) | $\left[A'\right] \cdot \left[Nb_{Ti}^{\bullet}\right] = K_0^{Nb} \exp\left(-\frac{\Delta H_{Nb}}{k_B T}\right)$ | (2.14) |

**Table 2-2:** Defect chemical reactions for STO and doped STO with their respective mass actions.

### 2.2.2 Conductivity of $SrTiO_3$

The electrical conductivity of STO depends on the defect structure and can be derived by utilizing the charge neutrality condition from equation (2.2-b) and substituting it into the according mass action law (equations (2.6) - (2.14) for different $\mathbf{p_{O2}}$ and temperature **T** conditions as demonstrated by [21-23, 20].

Below temperatures T < 750K the anion and cation sub-lattice is considered as frozen where no exchange of oxygen ions or rearrangement of cations is possible. Therefore the conductivity considerations presented in the following are states for **T** ~ 1000K. The derived states can be captured by quenching the STO system to room temperature.

Table 2-3 shows the charge neutrality conditions for a acceptor doped system and for a donor doped system.

| | ACCEPTOR DOPED | | DONOR DOPED | |
|---|---|---|---|---|
| | Charge neutrality condition | | Charge neutrality condition | |
| **Extremely reducing conditions** | $n \cong 2\left[V_O^{\bullet\bullet}\right]$ | (2.15) | $n \cong 2\left[V_O^{\bullet\bullet}\right]$ | (2.16) |
| **Reducing conditions** | $\left[A^{/}\right] \cong 2\left[V_O^{\bullet\bullet}\right]$ | (2.17) | $n \cong \left[D^{\bullet}\right]$ with $\left[D^{\bullet}\right] = const.$ | (2.18) |
| **Oxidizing conditions** | | | | |

**Table 2-3:** Charge neutrality conditions for acceptor doped STO for different oxygen partial pressures at T = 1000K

To determine the conductivity and the charge carriers as a function of oxygen partial pressure the equations presented in Table 2-3 have to be substituted into the according mass action laws of equation (2.7) & (2.8) for the corresponding reducing and oxidizing conditions. The result of this process is presented below in Figure 2-2.

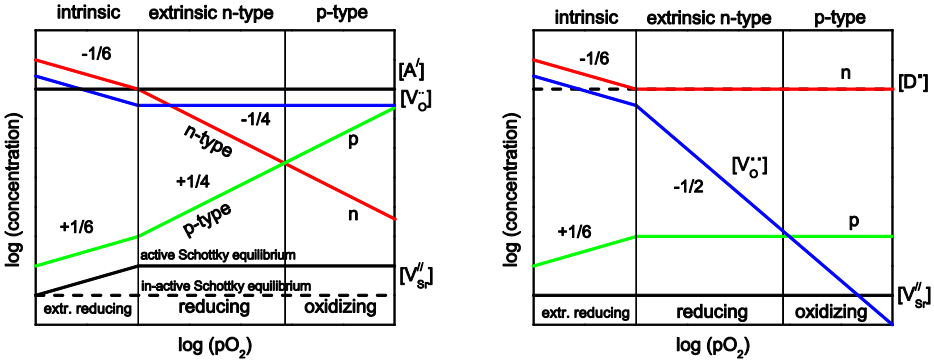


**Figure 2-2:** Schematic diagram of the charge carrier concentration in **a)** acceptor doped $SrTiO_3$ and **b)** donor doped $SrTiO_3$ as a function of oxygen pressure for 750K < $T_S$ < 1250K.

In general the total conductivity **σ** is the product of the charge carrier concentration and their mobility **μ**. For STO the conductivity can therefore be expressed by equation (2.19) with $q_e$ as the electron charge.

$$\sigma_{STO} = q_e e^{/} \mu_e + q_e \left[h^{\bullet}\right] \mu_h + 2 q_e \left[V_O^{\bullet\bullet}\right] \mu_{V_O^{\bullet\bullet}} \qquad (2.19)$$

The mobility of the different charge carriers are depicted versus temperature in Figure 2-3. It becomes clear that especially at room temperature (300K) the electron and hole mobility exceed the oxygen vacancy mobility by ~14 orders of magnitude, determined according to [17, 24].

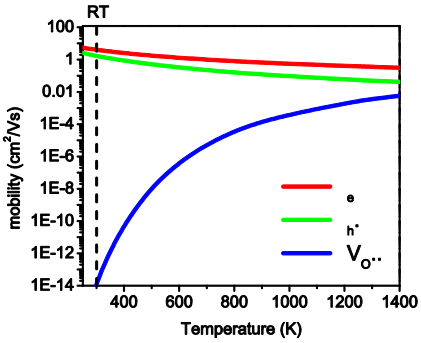


**Figure 2-3:** Charge carrier motilities of electrons $\mu_e$, holes $\mu_h$ and oxygen vacancies $\mu V_O^{\bullet\bullet}$ as a function of temperature.

### 2.2.3 Electronic structure of $SrTiO_3$

$SrTiO_3$ is a band insulator with a band gap of $E_g$ = 3.25eV although theoretical computations resulted in a direct band gap of $E_g$ = 2.28eV. Therefore, the electronic properties of STO depend on the electronic states near the valence band (VB) and the conduction band (CB). The valence band consists of filled O-2p orbitals whereas the conduction band comprises empty Ti-$3d^0$-states. Electronic states within the bandgap $\boldsymbol{E_g}$ can be introduced by defects as described in the previous chapter. Energy levels of theses defects [16] and the density of states (DOS) for oxygen vacancies [25] are shown below.

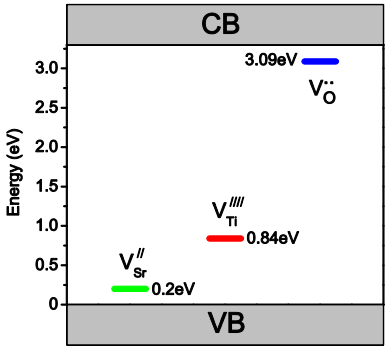


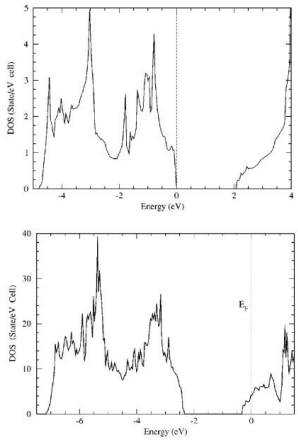


**Figure 2-4: a)** Energy levels of strontium vacancies $V_{Sr}''$, Titanium vacancies $V_{Ti}''''$ and oxygen vacancies $V_O^{\bullet\bullet}$ in $SrTiO_3$. *Adoped from* [16]. **b)** DOS of $SrTiO_3$ and $SrTiO_{2.875}$. *Adopted from* [25]

Oxygen vacancies are ionized at room temperature and their electrons are released into the conduction band and cause an n-type doping of STO. The DOS of an oxygen vacancy doped system is shown in Figure 2-4 (b). When oxygen vacancies are in the vicinity of strontium vacancies they can form di- and tri-vacancies, $V_{Sr}''$-$V_O^{\bullet\bullet}$ or $2V_O^{\bullet\bullet}$-$V_{Ti}''''$ and electrons are locally trapped by the cation vacancies.

As demonstrated in the previous chapter, the conducting mechanism can be p-type when cation vacancies are compensated by holes $h^{\bullet}$ which can be found in the valence band. Electrons from holes can either be excited into the conduction band or trapped by cation vacancies.

### 2.2.4 Electrical doping of $SrTiO_3$ by B-site cations

Just like a common semiconductor, STO can be electrical doped by donor type cations ($Nb^{5+}$, $Ta^{5+}$) or acceptor type cations ($Fe^{3+}$, $Al^{3+}$). Because Nb doped STO and Fe doped STO are discussed in the following chapters their effect within the STO compound is briefly explained; below are the defect chemical reactions for both doping scenarios.

$$Nb^{5+} \rightarrow Nb^{4+}: \quad Nb_{Ti}^{x} \leftrightarrow Nb_{Ti}^{\bullet} + e^{/} \tag{2.20}$$

$$Fe^{3+} \rightarrow Fe^{4+}: \quad Fe_{Ti}^{x} \leftrightarrow Fe_{Ti}^{/} + h^{\bullet} \tag{2.21}$$

$Fe^{3+}$ has a lower oxidation level than the host $Ti^{4+}$-sites and needs to be oxidized further to occupy the Ti-site and therefore misses an electron which turns it into an acceptor.
With the Fe doping concentration $\boldsymbol{x_{Fe}}$ the band gap energy $\boldsymbol{E_g}$ of STO changes parabolic as depicted in equation (2.22), according to [26].

$$E_g^0 = 3.25 - 1.9x + 0.5x^2 [eV] \tag{2.22}$$

The Fe concentrations described later on within this thesis are about $0 < \boldsymbol{x_{Fe}} \leq 0.1$ which result in a maximum band gap change of -0.185eV with a reduced band gap of $E_g = 3.065eV$.

Because $Nb^{5+}$ exhibits a higher oxidation level than the host $Ti^{4+}$-sites it can donate one electron and causes therefore an n-type behavior for Nb doped STO (Nb:STO) with the energy level of $Nb^{5+}$ close to the conduction band according to [27]. Depending on the doping level of Nb; Nb:STO can exhibit a metallic conductivity with $n^{+}$-characteristics for Nb concentrations $\boldsymbol{x_{Nb}} >$ 0.2wt%.

## 2.3 Space charge considerations

The concentration of defects in the bulk under a thermodynamic equilibrium can be described very well with the defect chemical equations presented in the foregoing chapters. However, the electrostatic properties can be different near the surface of the bulk. This is the case when charged species pile up near the surface and are forced to diffuse into the bulk system upon a chemical gradient. Then the electroneutrality condition needs to be replaced by the more universal Poisson equation [20, 19] shown below.

$$\nabla^2 \phi = -\frac{Q_{CD}}{\varepsilon_0 \varepsilon_r} \tag{2.23}$$

With $\phi$ denoting the electrostatic potential, $Q_{CD}$ the local charge density, and $\varepsilon_0$ and $\varepsilon_r$ as the vacuum and specific dielectric constant respectively. When there is a buildup of charged species near the surface the local space charge $\rho$ differs from 0, $\rho \neq 0$, and builds up an electric field $E$ influencing the flux $j$ of particles. The ambipolar diffusion described by equation (2.24) accounts for the chemical and the electrical gradient.

$$j = j_{diff} + j_{field} \quad \text{with} \quad i_{diff} = -D\frac{dC}{dx}(Fick'slaw), \text{ and } i_{field} = q\mu CE \qquad (2.24)$$

$D$ denotes the diffusion coefficient, $C$ the concentration and $q$ the charge number with the charge mobility $\mu$. The interaction of chemical gradients and electric fields result in the formation of concentration gradients of charged species near the surface which can stretch 100 – 150nm into the bulk. A more detailed description of the formation of space charge layers can be found in [23] [19] [28, 24, 29]

## 2.4 Non-stoichiometry, Lattice distortions and 2nd phase formation in $SrTiO_3$

As mentioned in the previous chapters, non-stoichiometry and its accommodation in $SrTiO_3$ requires the arrangement of charged species in the STO system accordingly. With the major ionic bonding characteristic, the crystalline structure of $SrTiO_3$ strongly depends on Coulomb interaction of the charged species. Theoretical computations by [30] [31] and experimental observations by [32] present the impact of the Coulomb interaction on the crystalline structure of STO.
Moreover, Jahn-Teller effects can contribute to lattice distortions as shown by [33] and also size effects of doping cations as presented in[34].

### *Non-stoichiometry and lattice distortion*

According to [31, 16], the overall reaction to a deviation $\delta$ of stoichiometry, causing vacancy type defects, is an outward response of the first nearest neighbor atoms (NN) due to Coulomb repulsion causing a chemical induced strain $\varepsilon_C$.

| Defect | $\varepsilon_C/\delta$ [31] | Distance [Å]➔ [%][16] |
|---|---|---|
| $V_O^{\cdot\cdot}$ | 0.001 | 2.06 (1.93 NN Ti) ➔ 6.3% |
| $V_{Ti}^{''''}$ | 0.402 | 2.03 (1.93 NN O) ➔ 4.95% |
| $V_{Sr}^{''}$ | 0.03 | 2.83 (2.73 NN Sr) ➔ 3.5% |
| **Defect** | | $\varepsilon_C/\delta$ [31] |
| $V_{SrO}$ | -0.008 | with $\Delta\varepsilon_C/\delta$ = -0.038 |
| $V_{TiO}^{''}$ | -0.26 | with $\Delta\varepsilon_C/\delta$ = -0.142 |

**Table 2-4:** Induced strain $\varepsilon_C$ and outward response of nearest neighbor atoms NN for certain vacancies in $SrTiO_3$.

The strain tensor for $V_{Sr}''$ is lower than for $V_{Ti}''''$ causing a lower chemical strain for $V_{Sr}''$ compared to $V_{Ti}''''$. Although an oxygen vacancy tends to cause a relatively large lattice expansion the resulting strain is low since the elongation is predominantly along the Ti-$V_O^{\bullet\bullet}$-Ti direction [31] and attraction along the O-$V_O^{\bullet\bullet}$-O direction; both reaction almost zero each other out.
Moreover, if an oxygen vacancy is introduced near a cation vacancy to form a di-vacancy the strain tensor is reduced since the oxygen vacancy locally compensates and shields the electrostatic potential and reduces the chemical strain as shown above in Table 2-4.

The chemical strain results in a lattice distortion which can be calculated according to [32] and elegantly derived by Gunkel in [22].

$$\sigma_x = \frac{E}{1-\nu}\frac{a_s - a_0}{a_0} \tag{2.25}$$

with

$$a_0 = \frac{(1-\nu)a_z + 2\nu a_s}{1+\nu} \tag{2.26}$$

Where E is the Young's modulus, ν the Poission's ratio and $\boldsymbol{a_z}$ the measured out of plane lattice parameter, $\boldsymbol{a_s}$ is the bulk lattice parameter. $\boldsymbol{a_0}$ is the intrinsic stress-free lattice parameter. Depending on the values of $\boldsymbol{a_z}$ and $\boldsymbol{a_s}$ equation (2.25) can yield a negative stress value or a positive stress value which results in compressive or tensile strain respectively.

***2nd phase formation***

When non-stoichiometry in $SrTiO_3$ is excessive a secondary phase can form. This can happen for Fe- Nb- and Ti- and Sr-excess.

In the case of Sr excess, so called Ruddlesden-Popper (RP) phases can form [35] with the nominal composition of $Sr_{n+1}Ti_nO_{3n+1}$ where one SrO layer is placed between *n*-$SrTiO_3$ perovskite layers [36]. The insertion of the SrO layer affects predominantly the TiO layer in contact with it which should happen randomly. When the SrO-layer is inserted the ***a*** and ***b*** lattice constant remain constant. The lattice constant ***c*** shifts to higher values and depends linearly on the Sr/Ti ratio in the system [36]. The shift of the lattice constant ***c*** for a RP-phase with n = 1 is schematically drafted in Figure 2-5. The incorporation of the additional SrO-layer can be either a results of the dissociation of $SrTiO_3$ according to the Schottky reaction or, as mentioned before, as a result of excess Sr. The defect chemical reaction for both scenarios is given below in equation (2.27) & (2.28).

Bulk reaction $$SrTiO_3 \leftrightarrow V_{Sr}^{//} + Ti_{Ti}^{x} + 2O_O^x + V_O^{\bullet\bullet} + SrO_{RP-phase} \tag{2.27}$$

Sr excess reaction $$Sr_{Sr}^{x} + SrTiO_3 + \tfrac{1}{2}O_2(g) + 2e^{/} \leftrightarrow V_{Sr}^{//} + Sr_2TiO_4 \tag{2.28}$$

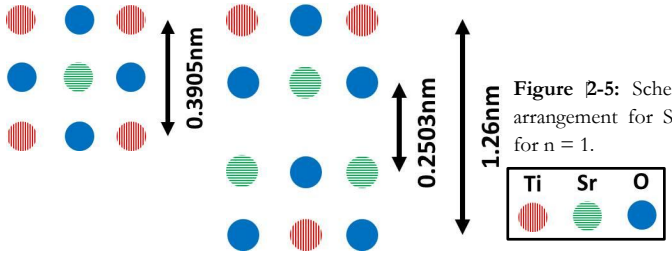


**Figure 2-5:** Schematic layout of the atomic layer arrangement for STO and $Sr_{n+1}Ti_nO_{3n+1}$ (RP-Phase) for n = 1.

STO – unit cell RP-unit cell for n = 1

It is also expected that the band gap $E_g$ of the STO compound slightly decreases with the incorporation of additional SrO-layers. With $E_g$ = 3.05eV, 2.9eV, 2.85eV for n = 1, 2, 3 respectively, according to [36].

A surplus of Ti-ions or dopants like Fe and Nb can cause precipitations and clustering of non-stoichiometric areas. Excess Ti can lead to $TiO_2$ precipitations.
If the concentration of Fe increases the likelihood of $SrTi_{1-x}Fe_xO_{3-y}$ phases increases which could result in the formation of extended defects and locally varying electronic properties [26]. A clustering of Nb in STO is possible which could lead to the local variation of the electronic properties of Nb:STO.

## 2.5 Resistive switching oxides for future memory devices

Up to now most random access memory (RAM) devices used for the data processing and storage in computers, cell phones and other electronic appliances are based on large-capacity flash memories and fabricated using metal-oxide semiconductors (MOS). For future devices a sandwiched metal oxide ought to be used to store information by changing its resistance upon a voltage stimulus to the metallic electrodes.
It was reported by the 1960's that some oxides change/reduce their resistance upon an applied voltage and the resistance could be "switched" back to a higher resistance. Because of this switching behavior they were referred to as resistive switching (RS) oxides. Since present storage devices are running into a scaling limit [37] and RS based devices would circumvent such limits, future RAM devices based on the resistance change are devised, called RRAM or ReRAM. It was demonstrated in [38] that the RS phenomena can be based on several physical mechanisms as shown in Figure 2-6.

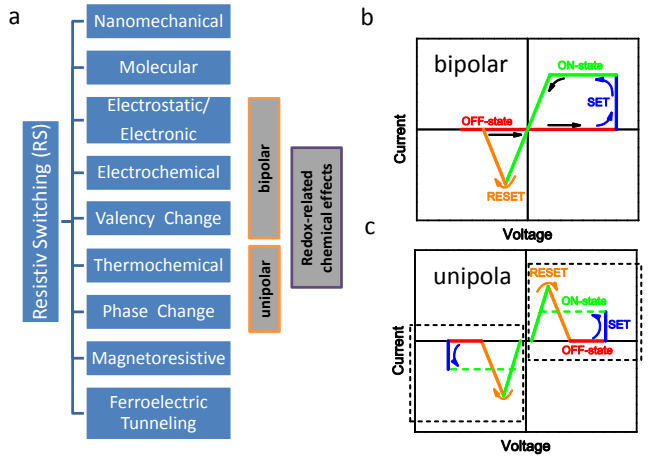


**Figure 2-6: a)** Resistive switching operation mechanisms **b)** Bipolar RS schematics **c)** Unipolar RS schematics. *Adopted from* [38]

The bipolar schematics show that the system switches for a certain polarity into the ON-state during the SET-process. When the polarity is reversed, the system switches back into the OFF state during the RESET-process. When a system depicts a unipolar RS mechanism the system switches for a specific polarity into the ON-state during the SET-process. When the same polarity is applied again the system switches then during the RESET-process into the OFF-state when reaching a specific threshold voltage.

***$SrTiO_3$ as a model system for valence change RS systems***

Although there is a plethora of metal oxides that exhibit resistance switching properties [39], $SrTiO_3$ is a suitable model material because it shows a stable resistive switching mechanism based on a valence change.

The resistance and valence change of STO can be assigned to the removal of oxygen and the incorporation of oxygen vacancies. Even a small concentration of $V_O^{\cdot\cdot}$ in STO causes an insulator-metal transition for the STO system. Upon the introduction of oxygen vacancies, Ti changes its valence state from $Ti^{4+}$ to $Ti^{3+}$.

The resistance switching mechanism of STO is based on the transport and aggregation of oxygen vacancies. When a STO thin film (d = 20 - 200nm) is sandwiched in between two electrodes oxygen vacancies are moved by applying an electric field. Oxygen vacancies drift towards the cathode and accumulate, which is referred to as a virtual cathode growth.

The accumulation of oxygen vacancies is possible if the electrode is blocking for the ionic current but sufficiently transparent for the electronic current. This means that the STO system switches into the ON-state when a negative potential is applied to the ion-blocking electrode and $V_O^{\cdot\cdot}$ accumulate until the growing virtual cathode reaches the counter electrode (anode). The system can be reset by applying a positive voltage to the ion blocking electrode, forcing the oxygen vacancies back into the thin film. This process defines the switching polarity which is

known as counter-8-wise switching. The switching polarity of the STO system can change and can exhibit also an 8-wise switching polarity. This is the case when the system switches into the ON-state for a positive polarization applied to the ion-blocking electrode.

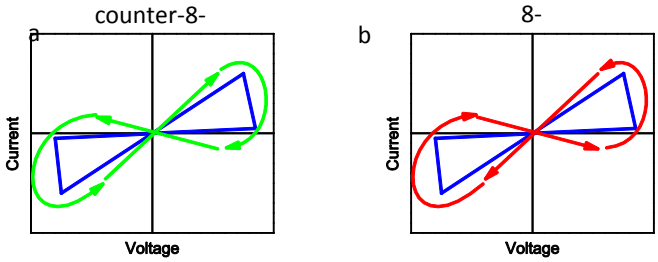


**Figure 2-7: a)** schematic for a system with virtual cathode and a counter-8-wise switching mechanism. **b)** schematics for a homogeneous switching mechanism with a 8-wise switching polarization.

Both switching polarities have been observed within a system [40]. It is suspected that different defect states in the thin film cause different switching polarizations. When fast oxygen vacancy movement is possible along extended defects in the oxide a counter-8-wise polarity is the result. When the system shows only point defects with a low oxygen vacancy mobility the system depicts an 8-wise switching mechanism. The resistance change is then based on the lowering of the Schottky barrier at the electrode interface.

Because the resistance change is based on the underlying arrangements on the nanoscale it is difficult to elucidate the principal cause for the resistance change. With universal techniques such as common spectroscopy methods or electrical testing methods the resolution on the nanoscale is hardly achievable. Therefore new and refined spectroscopy and electrical testing techniques have to be devised to elucidate the effects within the oxide after and especially during the resistance change.

# 3 Setup of a UHV-oxide Cluster-Tool

For in-situ investigation of thin oxide films a cluster tool was established from scratch which comprises 3 deposition tools, 4 analysis instruments and 4 sub-units (RHEED, OIRD, electrical testing, and sample preparation). The devices were consecutively installed and put into commission and were connected via a UHV transfer system to move samples to any tool attached to the system quasi in-situ.

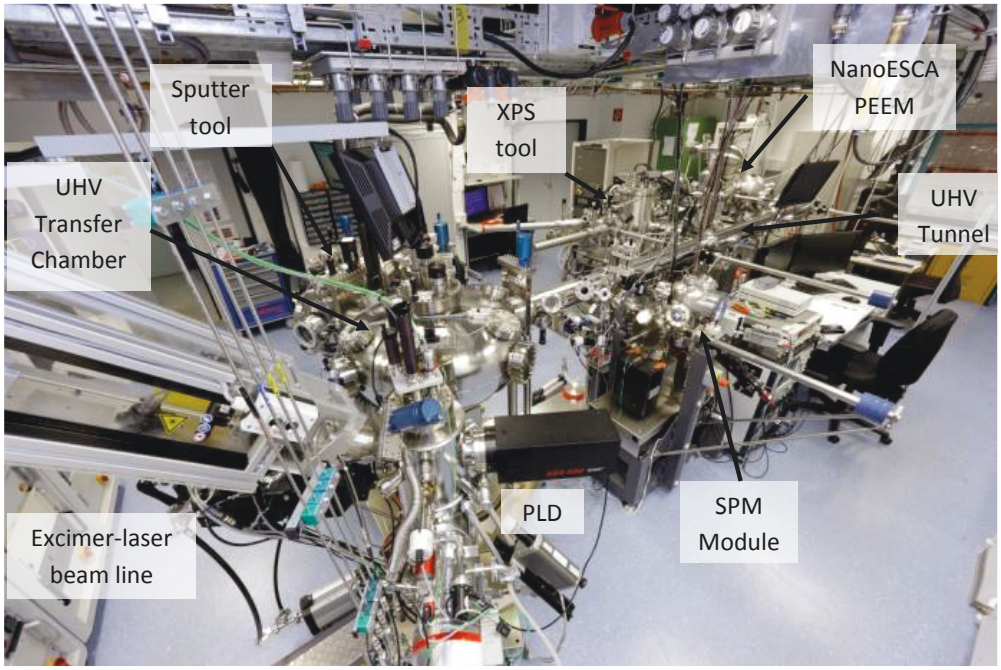


**Figure ß-1: View 1** UHV cluster tool with PLD, RHEED & OIRD, Sputter tool, SPM module, XPS and NanoESCA with PEEM

The cluster tool is presented in Figure ß-1 and Figure ß-2 with the deposition and analysis tools, the UHV transfer tunnel and the UHV distribution chamber. The fundamentals and working principle of the components are described in detail in the following.

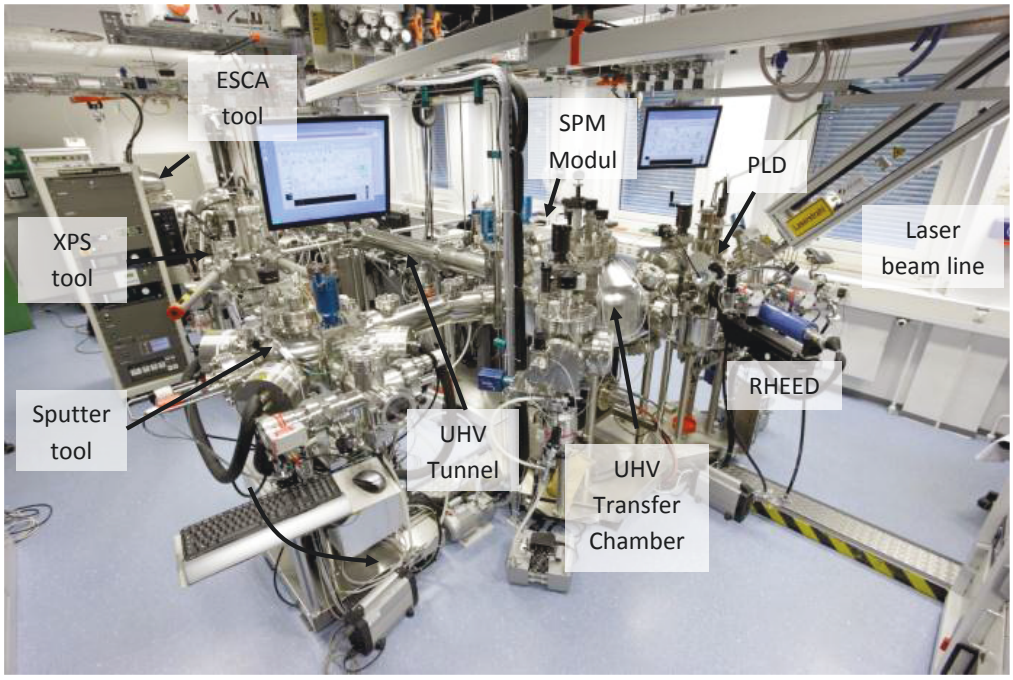


**Figure 3-2: View 2** UHV cluster tool with PLD, RHEED & OIRD, Sputter tool, SPM module, XPS and NanoESCA with PEEM

## 3.1 Deposition-Tools

With the deposition tools, complex oxides, nitrides or metals can be applied to substrates with a maximum area of 10x10mm. Thin film thicknesses can range from 0.2nm – 2000nm.

### 3.1.1 PLD (Laser-MBE) with RHEED and OIRD

A pulsed laser deposition (PLD) system (*Surface Technology*) was installed for the deposition of complex oxide thin films of high crystalline quality with excellent control of the film stoichiometry.

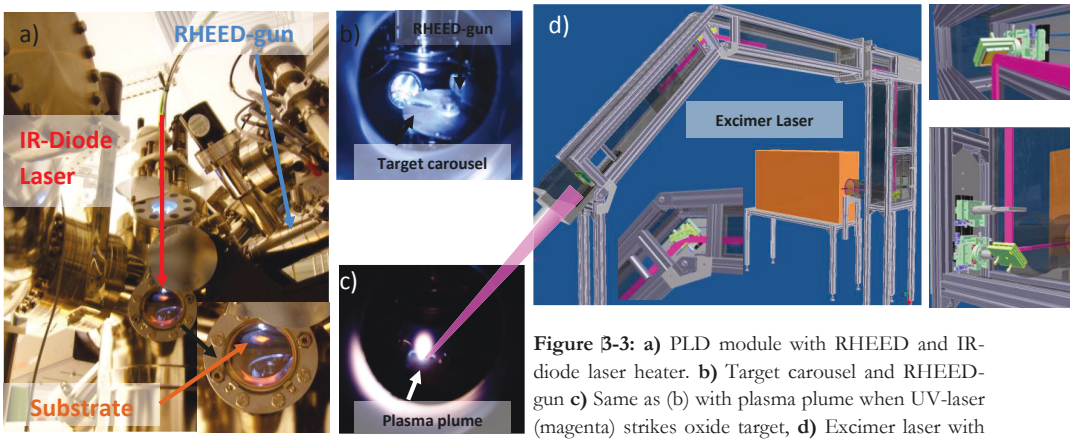


**Figure 3-3: a)** PLD module with RHEED and IR-diode laser heater. **b)** Target carousel and RHEED-gun **c)** Same as (b) with plasma plume when UV-laser (magenta) strikes oxide target, **d)** Excimer laser with beam line

The PLD system shown above is for the deposition of substrates with a size up to 10x10mm. The base pressure of the system is at ~$10^{-9}$mbar. The process pressure can be varied between $10^{-8}$mbar – 0.5mbar. The PLD-system can also be utilized for annealing experiments with ambient pressures of up to 500mbar and substrate temperatures of ~1500K in $O_2$, $N_2$ or $Ar/H_2$ environment.

Attached to the system is an excimer laser (*Compex Pro 205F - COHERENT*) for target ablation and thin film deposition respectively. The laser allows the ablation of any oxide without droplet generation which is needed for atomic scale deposition [41]. The ablation plume is shown in Figure 3-3 (c). The beamline for the laser was designed and engineered to guide the excimer laser into the PLD chamber and to focus the laser beam accordingly onto the target.

The substrate is heated by an IR-diode laser (140W, 925nm) which is fed via fiber into the UHV-chamber. With the IR-laser the substrate can be heated up to 1900K. The IR-laser setup allows the sample to be quenched from its deposition temperature. When the laser is turned off the sample cools down rapidly due to is low individual mass. The quenching allows freezing non-equilibrium states into the system.

### *Reflection high energy electron diffraction (RHEED)*

The deposition process is in-situ monitored via a reflective high energy electron diffraction tool (RHEED) that allows gauging atomic diffusion of ad-atoms during growth and surface/thin film morphology analysis as well as determination of the actual growth mode [42, 43]. The RHEED system comprises the electron gun and the fluorescent screen and a camera with a computer system (*kSA-400*) that captures and analyzes the diffraction pattern of the scattered electrons from the substrate as shown below.

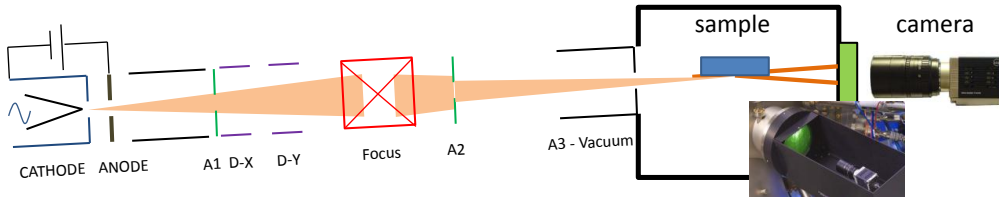


**Figure 3-4:** RHEED gun; electrons are accelerated from cathode to anode with ~ 30kV. Electron beam (~40µA) passes aperture A1 and can be deflected in X and Y direction by D-X and D-Y respectively. The electron beam is then focused onto the sample and passes aperture A2 and the vacuum aperture A3. Electrons are partly reflected and diffracted by the sample and captured by the fluorescent screen. An external camera captures the intensity pattern of the reflected and diffracted electrons.

### *Oblique Incidence optical reflectivity difference (OIRD)*

With the OIRD tool the change of the dielectric constant can be monitored in-situ during the epitaxial growth of oxide thin films which can be used to determine the e.g. the chemical kinetics. The relative reflectivity change of s- and p- polarized laser light (He-Ne, 633nm, 0.3mW) is measured at oblique incidence (~7°). The relative reflectivity is a function of optical dielectric constant of the surface which is in part a function of the oxygen vacancy concentration. The difference in the relative reflectivity change between s- & p- polarized light is being used to determine the oxidation of the growing oxide film. The setup of the system is shown and described below [44-46].

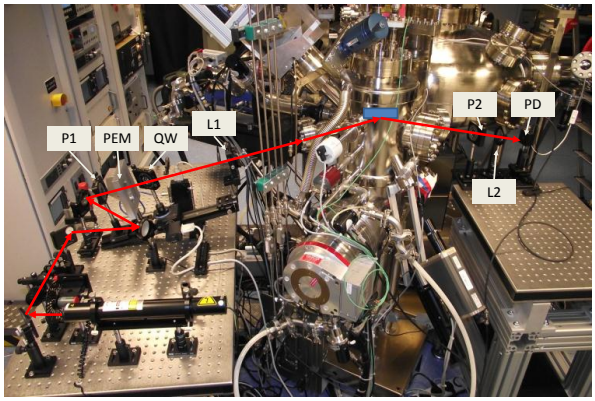


**Figure 3-5:** OIRD setup for relative reflectivity measurements for PLD processes. Laser passes through polarizer P1 to become p-polarized, then p- and s-polarized by a PEM with 50kHz and a quartz window for adjusting the s-polarization relative to the p-polarization. The reflected laser from the substrate is then captured by the photodiode (PD) after passing a second polarizer (P2).

The laser light is initially p-polarized by a polarizer (P1) and then directed through the photo elastic modulator (PEM). As a result the laser is p- and s-polarized at a frequency of 50kHz. The polarization-modulated beam then passes through a quartz window (QW) on a rotation stage. Hereby, the s-polarized component can be reduced relative to the p-polarized component. The beam is then focused by a lens (L1) and enters the UHV chamber through a fused silica window and strikes the substrate surface and is reflected. The beam exits the chamber through a fused silica window, passes through a polarizer again (P2), is focused (L2) and detected by a photodiode. The photocurrent is then analyzed by a lock-in amplifier.
By adjusting the polarizer and the quartz window the reflected p- and s-polarized light can be set to zero. During deposition the reflectance changes and the difference of reflected s- & p-polarized light is used for analysis.

### 3.1.2 Sputtering tool

The sputtering tool (*Surface Technology)* is utilized for the deposition of metals, oxides ($TiO_x$ $WO_x$) and nitrides (TiN) for example. The system comprises 4 sputter guns (magnetrons). The guns can be operated in the DC or RF mode at up to 600W. Substrates can be up to 25x25mm large and heated up to 900K. The base pressure is at about $10^{-8}$mbar.

### 3.1.3 E-beam PVD

An E-beam tool was designed for the in-situ deposition of extremely thin metallic films which can be used as top electrodes for RS experiments for example. The base pressure of the system is at $10^{-9}$mbar. Additionally, the system also serves the purpose of being a preparation chamber for single crystals of complex oxides for STM and XPS analysis. The samples can be heated up to 1300K and treated by $Ar^+$-ions from an ion gun to treat and modify the surface of the crystal for example. Additionally the system has evaporation cells attached to deposit exotic composites on the substrate surface.

a) b)

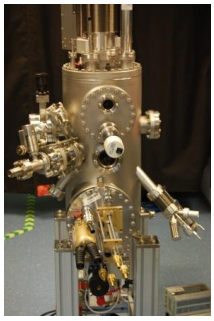

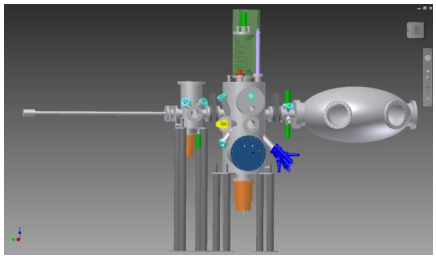

**Figure 3-6: a)** E-Beam PVD tool after assembly, **b)** CAD construction of the E-beam tool and the LEED chamber

## 3.2 Characterization-Tools

In order to investigate the specimen for their electronic, chemical and morphological properties several in-situ characterization tools are attached to UHV cluster. The specimen can be transferred under UHV conditions via a "Piggy-bag" system to the analysis tools. This allows to avoid (re)-oxidation or contamination by adsorbates in ambient.

### 3.2.1 SPM-Tool with LC-AFM, NC-AFM, STM & Q-plus

With the in-situ UHV SPM tool the topography and the local electric properties of a sample can be investigated. Additionally the ferroelectric properties of a specimen can be probed as well. The tool combines various probing techniques such as contact-AFM which is used for topography scans as well as local conductivity measurements (LC-AFM). The topography can also be inspected via non-contact AFM which has some chemical sensitivity.
Also general STM & STS is possible to measure e.g. the LDOS of a specimen. With the Q-plus sensor the topographic and tunneling aspects can be combined.The tool allows measurements only in UHV atmosphere. The sample can be cooled down via liquid helium to about 30K and heated up to 600K. Any temperature in between 30 – 600K is possible by combining both mechanisms.
Attached to the system is an electrical testing system (*Aixacct*) to apply ultra fast voltage pulses to the AFM tip (ns-range) and to do standard I(V) scans with an extended scanning range for the current (mA) for i.e. resistive switching investigations.
The tool was used for local RS experiments on STO films which will be shown later. By the LC-AFM and STS the RS mechanism can be investigated on the nanometer scale which is hard to come by with generic approaches.

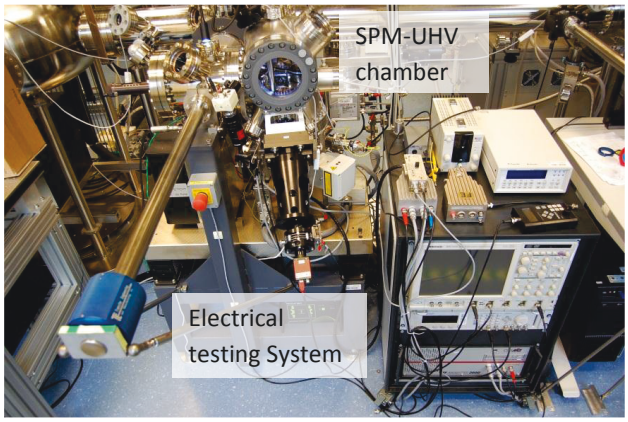


**Figure 3-7:** SPM tool with UHV chamber for in-situ analysis of topography and electronic testing of thin films by LC-AFM, contact AFM, non-contact AFM, Q-Plus sensing and STM.

### 3.2.2 X-ray photoemission spectroscopy (XPS)

The in-situ XPS tool (*Versa-Probe* by *PHI*) is used for chemical analysis of the substrate/thin film. Valence state as well as electronic states can be detected. To meet the actual requirements of probing

small areas the system comes with a spatial resolution of 10µm and a high count rate due to high transmission. For navigation on structured samples surface SXI mapping is possible.
Since mostly insulating oxides are being investigated the tool comes with a dual beam neutralization (flood gun, Ar-ion gun). Additionally the system can do depth profiling and for organic specimen UPS is possible as well.

### 3.2.3 Nano-ESCA / PEEM

With the NanoESCA (*OMICRON*) tool chemical state mapping (XPS) with a very high lateral resolution can be achieved (<500 nm under laboratory conditions). The instrument gives chemical state information beyond the limits of other high lateral resolution techniques such as scanning Auger and TOF SIMS. Real time sample navigation is ensured by PEEM technique which operates in the secondary electron regime. The PEEM mode allows finding small features easily on a large sample area and provides high resolution (< 50 nm resolution). In addition the PEEM mode provides quantitative information on the very local work function and local sample charging.

a) b)

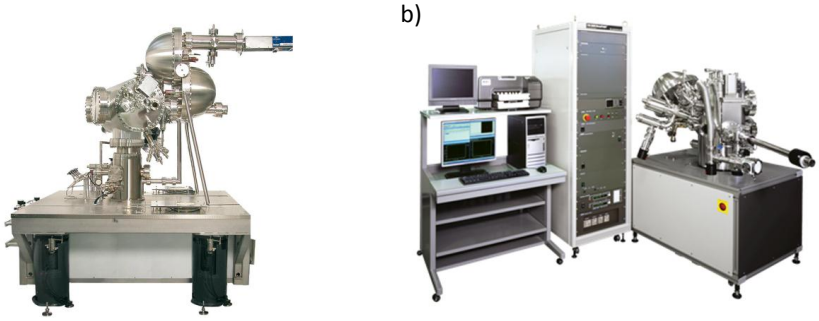

**Figure 3-8: a)** NanoESCA / PEEM by *OMICRON* for elemental and chemical analysis on the nanoscale as well as XPS-imaging. **b)** XPS system by *PHI* for chemical analysis

### 3.2.4 LEED

A tool for low energy electron diffraction (LEED) system is attached to the E-beam evaporation tool. With this system the atomic structure and the arrangement of the surface can be investigated prior to deposition or STS analysis. In conjunction with the preparation tool attached to the E-beam source the surface arrangement of crystals can for example be altered via temperature or ion bombardment.
An electron beam (20 - 200eV) is directed on the sample surface in a $10^{-9}$mbar ambient. The electrons interact with the sample surface and elastically scattered back onto a fluorescent screen. The resulting diffraction pattern on the screen depicts the reciprocal lattice of the substrate. Thereby lattice parameters of the sample can be determined.

## 3.3 Engineering of a high-temperature (HT) holder

As it was shown above the PLD system is equipped with an IR diode laser source for substrate heating. Because mainly oxides are handled in the system with melting points $T_M$ beyond 1500ºC, process temperatures exceeding 800ºC and strongly oxidizing atmosphere are a likely scenario for e.g. deposition, annealing etc. Usually substrates are glued onto a steel holder (1.4404, 316L) with either Ag-paste or Pt-paste which also serves as the absorber for the IR laser and forwards the absorbed laser energy to the glued on substrate. However, these gluing techniques are not applicable for temperatures exceeding substrate temperatures of 900ºC due to outgassing and decomposition of the paste. For this reason a high temperature (HT) holder was designed that allows heating of the substrate beyond 1300ºC and in-situ analysis by RHEED of the substrate with a high chemo-thermal stability (CTS) in oxidizing environment ($O_2$) and high temperature.

### 3.3.1 Engineering

The holder design has to serve several purposes besides the aforementioned chemo-thermal stability. One aspect is its mechanical stability with respect to handling and in-situ transfer. Therefore, ceramics as a holder material are not suitable. The HT-holder design also has to allow for the RHEED to strike the substrate in a glancing angle without interfering with the $e^-$-beam. The following table summarizes the properties of different possible materials.

| | Refractory metals | Oxide-Ceramics | Carbides | Nitrides | Inconel | Steel | Noble Metals | | 214® Alloy |
|---|---|---|---|---|---|---|---|---|---|
| | W, Mo, Ti | $Al_2O_3$ | | BN, AlN, | | | Au | Pt | |
| **Mechanical stability** | (+) | (-) | (+) | (+) | (+) | (+) | (-) | (+) | (+) |
| **CTS ($O_2$ & HT)** | (-) | (+) | (±) | (±) | (-) | (-) | (+) | (+) | (+) |
| **Chemical inertness** | (-) | (+) | (±) | (±) | (-) | (-) | (+) | (+) | (+) |
| **Tooling properties** | (±) | (-) | (-) | (-) | (+) | (+) | (-) | (±) | (+) |
| **Price, Availablity** | (+) | (+) | (+) | (+) | (+) | (+) | (±) | (±) | (±) |

**Table 3-1:** Summary of possible materials and their properties for the high temperature holder. (+) stands for a good agreement with respect to the actual requirement and (-) for an unfortunate agreement.

The material of choice for the HT holder is alloy-214® with complex composition of several components as shown below which shows overall the best performance.
Due to its metallic character it obtains a good mechanical stability as well as decent tooling properties. The CTS and the chemical inertness towards the substrate complement each other. This is due to the formation of a $Al_2O_3$ layer on the surface of the alloy-214® when exposed to high temperature in an oxygen environment. Aluminum diffuses due to thermal activation and its affinity to oxygen towards the surface and reacts with the environment and forms an $Al_2O_3$ layer. This oxide is chemically stable and does not react with the oxide substrate. If damaged

during handling and transfer it "heals" itself when exposed to high temperature and oxygen again.
The layout of the holder is shown in the following along with its components.

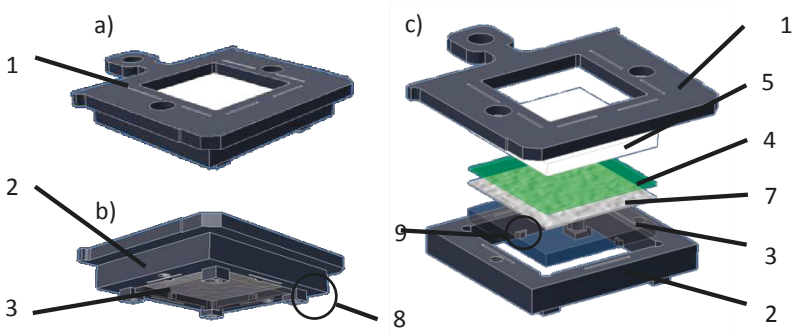


**Figure 3-9:** Substrate holder, **a)** top view, **b)** bottom view, **c)** explosion view

The holder consists of two components namely the top frame (1) and the bottom frame (2) which clamp the stack of the substrate (3), the laser absorber (4) and the heat sink (7) together. The stack is sealed by a sapphire window (5) which prevents e.g. evaporated absorber material which could re-deposit on the IR-laser entrance window. The two frames are fastened by two screws.
To reach substrate surface temperatures beyond 1200°C the area of contact of the substrate with the holder must be minimized. The substrate itself is forced against 4 protrusions (8) on the bottom frame each with an incursion, and is adjusted by 4 ridges (9).
When the IR-laser is directed on the HT-holder it passes the sapphire window (5) and hits the absorber (4). The absorber material effectively converts the laser radiation into heat and forwards the heat towards the heat-sink (7) and the substrate (3).

### 3.3.2 Performance

The performance of the heater was tested by trying out different heat sink materials and combinations. The temperature of the substrate was measured by 2 pyrometers. Pyrometer 1 detected the temperature of the NiO absorber at a wavelength of 2µm. Pyrometer 2 captured the surface temperature of the STO substrate at a wavelength of 8 – 14µm. STO is transparent for wavelength $\lambda < 8\mu m$ and absorbing for wavelength $\lambda > 8\mu m$. By measuring in the range of 8 – 12 µm the real surface temperature of STO can be determined without falsification of the signal by radiation of other heat sources. Figure 3-10 depicts the temperature of the absorber (NiO) and the resulting STO surface as a function of different heat sink materials.

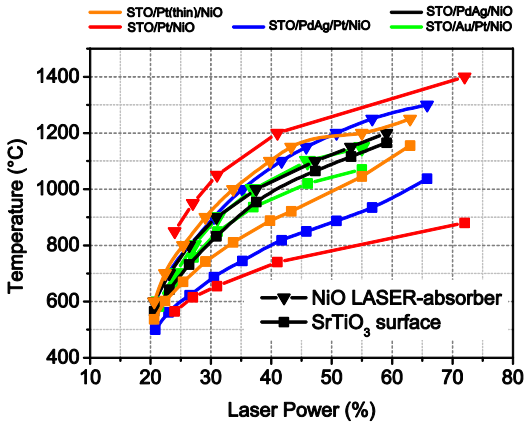


**Figure 3-10:** Substrate temperature (STO) and absorber temperature (NiO) versus IR-laser energy for different heat sink materials and combinations of Pt (80µm), Pt-thin (20µm), PdAg (20µm) and Au (20µm).

The best performance yields the PdAg heat sink. However, PdAg shows a chemical reaction with STO at temperature > 1000°C which deteriorates the STO substrate. Thin Pt foil (20µm) is best suited to reach temperatures ~1200°C. The substrate at a temperature of 1200°C is shown below in Figure 3-11.

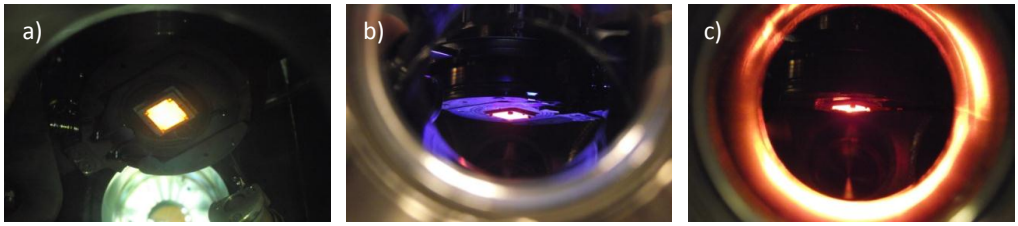


**Figure 3-11:** $SrTiO_3$ Substrat (10x10x1mm) clamped inside the high temperature holder with a substrate temperature of $T_S$ = 1200°C. **a)** Bottom view, **b),c)** Side view

# 4 Experimental

Within this chapter the experimental techniques for $SrTiO_3$ thin film deposition and investigation are described. The necessary theoretical groundwork to explain and simulate the analyzed data is presented as well.

## 4.1 PLD process and in-situ analysis methods for thin film defect engineering

The PLD process described here is the same for all experiments presented here within. For the ablation process a KrF excimer laser with λ = 248nm (*COHERENT, Compex-Pro 205F*) is focused onto the (oxide-) target and enters the PLD-Chamber through a quartz window. The laser beam hits the target with an angle of 45°. The UV-laser pulse lasts about 25 ns and the laser energy can be tuned by a beam attenuator in front of the PLD chamber.
The PLD plume travels through the background gas towards the substrate. The pressure in the chamber can be varied from 1e-8mbar – 400mbar. The substrate is either glued via Ag-paste or clamped to the HT substrate holder. The Substrate holder is heated via the IR-diode laser.

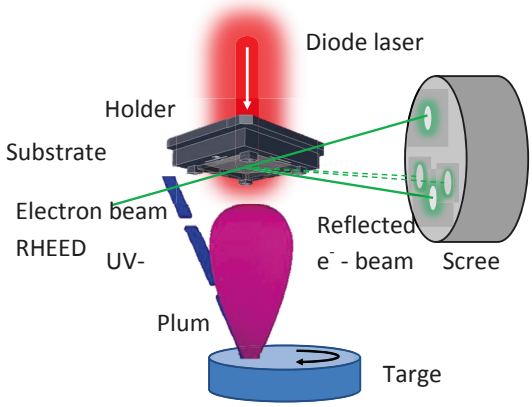


**Figure 4-1:** PLD process schematics. UV-laser (248nm) strikes target in an 45° angle. Plasma plume travels toward substrate. Substrate is heat via laser (925nm). Thin film deposition is monitored by RHEED with electron beam striking the substrate in a glancing angle (1-4°). Electron beam is reflected and partly diffracted.

### 4.1.1 Ablation characteristics

When the focused UV laser beam strikes the target a characteristic plasma plume evolves. The ablated mass $\Delta z_\upsilon$ from the target is a function of the absorbance **A** and the laser fluence $F_L$. The threshold fluence $F_{th}$ defines the minimum energy necessary to ablate a material. The ablation rate can be described according to Amoruso et al. [47] with;

$$\Delta z_\upsilon \approx \frac{A\left(F_L - F_{th}\right)}{\rho L_\upsilon} \quad \text{with} \quad F_{th} \approx \frac{\rho c \Delta T_m L_{th}}{A} \quad \text{and} \quad L_{th} \approx \left(2D\tau_P\right)^{1/2} \quad \text{with} \quad D = \frac{k}{\rho c} \qquad (4.1)$$

The ablation procedure is basically an evaporation process that takes place when $\rho cT$ (density, specific heat, temperature) exceeds $\rho L_v$, where $L_v$ is the latent heat per unit mass. $L_{th}$ describes the penetration depth of the heat necessary to evaporate the material. The heat diffusion $D$ is directly proportional to the thermal conduction $k_{th}$.
The above described linear ablation behavior is one of 3 ablation regions described by Anisimov et al. who showed in [48] that near the threshold the ablation rate shows a so called Arrhenius dependence with $\Delta z_v \sim a \exp(-b/F_L)$.
For $F >> F_{th}$ the ablation rate shows a logarithmic dependence where the evaporable surface is screened by the evolving plume where $\Delta z_v \sim a \ln(F_L/b)$. The laser fluencies for most PLD processes are within the linear dependence.

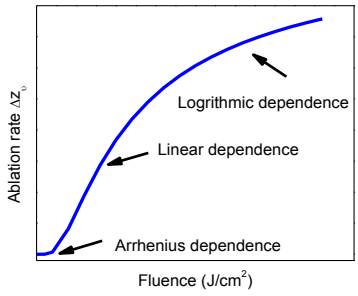


**Figure 4-2:** Schematics of the ablation rate vs. laser fluence for a system based on the thermal model of material removal.

### 4.1.2 In-situ film growth analysis by RHEED

Reflection high energy electron diffraction (RHEED) is a common technique in general to monitor the thin film growth using PLD or MBE systems [49, 43]. The principle of RHEED within the PLD is depicted in Figure 4-1. An electron beam with a diameter of ~ 0.5 mm is accelerated with 30 kV and directed on the substrate surface in gracing angle of < 5°. The electrons with a wavelength $\lambda$ = 0.07 Å and the momentum $k_0$ then interact with the substrate surface and are diffracted, hereby the penetration depth of the electrons are only a few atomic layers.
The diffracted electrons with the momentum $k_D$ then hit the phosphor screen, as can be seen in Figure 4-1. The resulting diffraction pattern is depicted below and described

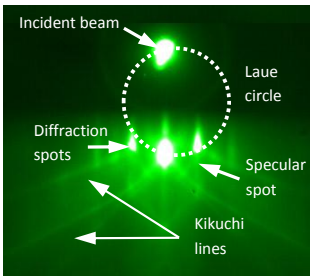


**Figure 4-3:** RHEED diffraction pattern of a vicinal $SrTiO_3$ surface recorded on the phosphor screen. The radius of the Laue-circle and the number of the diffraction spots depends on the incident angle of the $e^-$ -beam.

The diffraction pattern depicts the reciprocal lattice of the STO and is produced when the momentum of the incident beam and the diffracted beam differ by a reciprocal lattice vector $\boldsymbol{G}$ with $G = k_D - k_0$. Elastically scattered electrons can be seen by the so called "Kikuchi lines" in the diffraction pattern. The specular spot is the directly reflected incident electron beam.

The deposition process is monitored in-situ by recording time resolved specular spot intensity oscillations to observe and interpret the 2D growth processes of the growing thin film [43]. The specular spot intensity $\boldsymbol{I}$ of the reflected electron beam is a direct function of the step density $\boldsymbol{S}$ and the surface coverage $\Theta$ on the substrate surface. One complete oscillation indicates the completion of a STO layer with the thickness of a unit cell i.e. 0.3905nm.

When depositing a $SrTiO_3$ thin film on a STO single crystal substrate the intensity variation of the specular spot is a result of the interaction of electrons with ad-atoms of the growing film. This variation of the initial intensity $\boldsymbol{I_0}$ can be discussed using the difference in surface coverage $\Theta$ where the RHEED intensity $\boldsymbol{I}$ can be expressed by [50]:

$$\frac{I}{I_0} = |F_{hkl}|^2 [A(\Theta)]^2 = \left(\sum (-1)^n (\Theta_n - \Theta_{n+1})\right)^2 \qquad (4.2)$$

$\boldsymbol{F_{hkl}}$ is the structure factor, $\boldsymbol{A(\Theta)}$ the scattering amplitude and $\Theta_n$ the coverage of n-th monolayer. When the surface coverage $\Theta$ changes the step density $\boldsymbol{S}$ on the substrate surface changes as well. Because electrons are predominantly scattered by surface steps it makes sense to use the step density as a measure to discuss the RHEED intensity variation. The following model suggested by Stoyanov [51] is used to interpret the RHEED intensity.

$$\frac{I}{I_0} = 1 - \frac{S}{S_{\max}} = 2\sum \sqrt{\pi N_{S,n}(1-\Theta_n)}\sqrt{-\ln(1-\Theta_n)} \qquad (4.3)$$

with

$$S(t) = 2 \cdot \sqrt{\pi \cdot N_{S,n}} \cdot (1-\Theta) \cdot \sqrt{-\ln(1-\Theta)} - C \cdot D_S \cdot \Theta \qquad (4.4)$$

and

$$\Theta(t) = 1 - \exp\left( -\pi \cdot N_s \cdot \left( \int_0^t v_s(\tau) d\tau \right)^2 \right) \qquad (4.5)$$

$\boldsymbol{N_{S,n}}$ is the saturation nucleation density for n-th layer. The relation between step density and the RHEED intensity is verified using STM [52]. Because nucleation of the ad-atoms is not an instantaneous process but requires surface diffusion the step density $\boldsymbol{S}$ of the growing film

relaxes over time until it saturates. This relaxation time is denoted with τ and can be monitored by a relaxation of the specular RHEED intensity ***I*** after each pulse.
In a 2D growth model, the nucleation kinetics can be described with respect to the surface coverage [49]. For low surface coverage the relaxation time τ can be expressed by equation (4.5) where the diffusion in between the nuclei is predominant.

$$\tau \cong \frac{1-\Theta}{D_S \cdot N_S} \qquad (4.6)$$

The surface coverage Θ represents the fraction of islands on the surface, $D_S$ is the diffusion coefficient and $N_S$ the saturated island density.

### 4.1.3 Plume analysis

To get a better understanding of the deposition process the investigation of the PLD plasma plume is helpful since the plume species and their kinetics are significant for the thin film stoichiometry and the growth mechanism. It was shown by many researchers before that the interaction of the plume with the background gas can result e.g. in the separation of plume species or sputtering of the surface due to high energetic plume species.

The plume is therefore investigated by optical means where the plume is imaged by a fast ICCD camera setup. Images of the plume are taken for different propagation states and for specific delay times $\tau$ after the excimer laser was triggered. To intensify the optical signal several frames are taken for each delay time and juxtaposed.

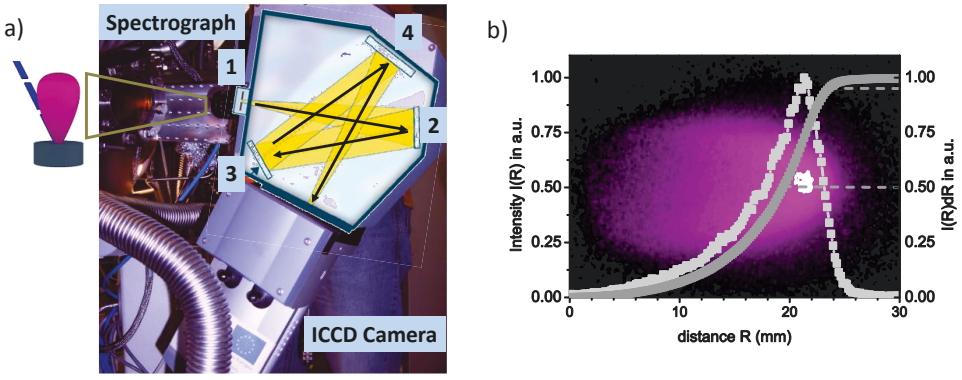


**Figure 4-4: a)** Experimental setup for optical imaging and optical emission spectroscopy of the PLD plume 1) Focusing lens, 2) Mirror / Monochromator, 3) Mirror / Grating, 4) Mirror / Filter. **b)** 2D image for a PLD plume at a delay time τ = 4.5 µs with intensity profile I(R) and integrated intensity profile ∫I(R)dR. The plume front is defined for I(R)dR = 95% and the plume center is defined for I(R)dR = 50% (dashed lines). y = 0 represents the target surface.

The plume and its emission intensity $I_P$ can be plotted versus the propagation distance $R$ as shown in figure (b) above. The plume front is defined when the integrated plume intensity reaches 95%, I(y)dy = 0.95. The plume center is defined for an integrated plume intensity of 50%, I(R)dR = 0.5. This procedure is done for every plume taken at a specific delay time $\tau$. The plume front position $R_F$ and the plume center position $R_C$ can then be plotted versus delay time $\tau$ in so called $R - \tau$ plots.

When the Mirror at position 3 in the spectrograph is substituted by a diffraction grating the emitted light of the plume can be split and diffracted to different angles and yields an emission spectrum of the excited species in the plume, see Figure 4-5.
Each emission line can be assigned to an element. In the case of $SrTiO_3$ the emission of Sr-species and Ti-species can be seen. Oxygen is very volatile and shows only weak intensities in the visible range.

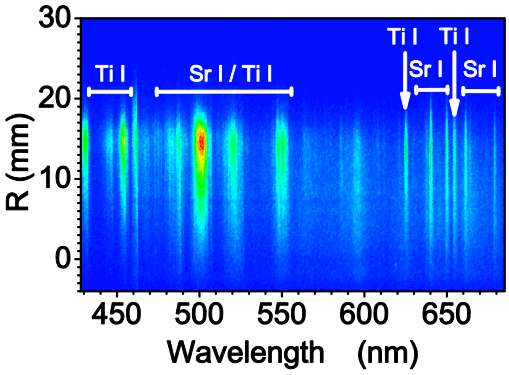


**Figure 4-5:** 1D image of the emission spectrum for a SrTiO3 PLD plume at τ = 4.5 µs. The emission lines for Sr-species and Ti-species are marked.

The emission lines for a $SrTiO_3$ plume are shown in Figure 4-5 above. The majority of the Sr-emission lines are at 630 – 700nm. The majority of the Ti emission lines are at 420 – 450nm. The emission lines/bands at 470 – 560nm are overlapped emissions from Ti- and Sr-species. When the plume species oxidize the emission lines broaden and form so called emission bands and merge into each other eventually.

**Plume kinetics**

In the following the equations for the interaction model of the PLD plume with the background gas are discussed and taken from the approach by Sambri et al. [53, 54].
When the plume expands and interacts with the background gas it is compressed by a dense gas layer at the plume front that exerts a force on the plume that slows it down. This procedure forms a hemispherical plume front with the radius $R$. During this process the plume with its mass $M_p$ accumulates gas molecules with the mass $M_g$ at the plume front. The mass of the added gas is a function of $R$ and is shown below.

$$M_g = \tfrac{2}{3}\pi\rho_g R^3 \qquad (4.7)$$

With $\rho_g$ as the background gas density. With the addition of gas molecules the linear momentum of the plume increases, see equation (4.8). Because the radius $R$ of the plume increases with the addition of gas molecules the drag (force, $-F$) on the plume increases as well. The drag and the change of the plume momentum are related. The velocity of the plume $u$ can be assessed as follows.

Change of the linear momentum $p_p$ of the plume

$$F_p = \frac{dp_p}{dt} = \frac{d}{dt}\left[M_p + M_g(R)\right]\cdot u \qquad (4.8)$$

Drag force by the background gas pressure

$$F_g = -2\pi \cdot R^2 P_g \qquad (4.9)$$

Plume front velocity u(R)

$$u(R) = c_0\sqrt{\frac{b^2}{\left(a^3 + R^3\right)^2} - 1} \qquad (4.10)$$

With the background gas pressure $P_g$, and $a$ as the characteristic scaling length as well as $b$ as a constant.

With $\quad a = \sqrt[3]{\dfrac{3M_p}{2\pi\rho_g}} \qquad b = a^3\sqrt{1+(u_0/c_0)^2} \approx a^3(u_0/c_0) \qquad c_0 = \sqrt{P_g/\rho_g}$

The term $c_0$ is a characteristic scaling velocity and depends on the background gas. The initial plume velocity $u_0$ can vary and depends on the ablation characteristics. With $R(\tau) = \int u\,dt$ the measured R – τ curve can be fitted and the plume mass $M_p$ and the initial velocity $u_0$ as fitting parameters determined.
The plume velocity obviously decreases continuously during the propagation through the background gas and eventually stops. The stopping distance $R_{st}$ can be calculated by

$$R_{st} = \left(\frac{3M_p}{2\pi\rho_g}\left(\frac{u_0}{\sqrt{P_g/\rho_g}} - 1\right)\right)^{1/3} \qquad (4.11)$$

The propagation of the braked plume through the background gas is described by the Point-Blast-Wave (PBW) model where the plume propagates like a shock wave. The 3 regimes of a propagating plume in a background gas are therefore the free expansion, the shock-wave like expansion (PBW) and the diffusion-like expansion. First the plume expands freely and the transforms into a shock-wave-like expansion at a transition point $R_T$. Later the plume transforms at $R_D$ from the shock-wave into the diffusion like expansion.

**Scattering effects of plume species**

When the plume travels through the background gas it interacts with the gas molecules and is compressed. Thereby, the plume species are scattered by the gas molecules which is described by Amoruso et al. in [55].

The number of collisions $k$ of plume species during their propagation towards the substrate is a function of the gas pressure $P$. The probability $\Pi_k$ of a plume species experiencing k-collisions can be expressed by the Poisson distribution given below;

$$\Pi_k(\mu,\lambda) = \left(\frac{P}{P_0}\right)^k \frac{e^{-\frac{P}{P_0}}}{k!} \qquad \text{with} \qquad P_0 = k_B T / \sqrt{2} \cdot x_D \sigma_c \tag{4.12}$$

$P_0$ is a constant that depends on the current PLD settings with the travel distance $x_D$, the ambient temperature $T$ and the background gas with its characteristic scattering cross-section $\sigma_c$. $x_D$ does not resemble the target substrate distance, it basically is the distance from where the plume transforms into the shock-wave like expansion $R_T$ to the substrate; $x_D \sim D_{TS} - R_T$.

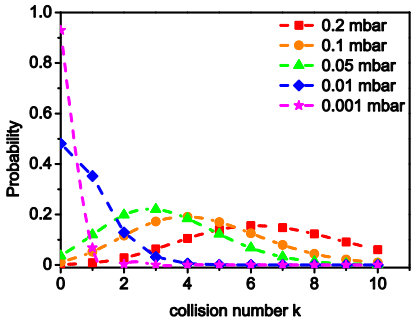


**Figure 4-6:** Qualitative probability of scattering events for plume species and different background gas pressures.

## 4.2 X-ray diffraction analysis

A straight forward method to investigate the crystalline quality of a thin film is its examination by X-ray diffraction (XRD). With this method the crystalline properties are examined and changes in the lattice e.g. changes of the lattice parameters detected. Especially the lattice parameter variations can be a strong indication for the presence of defects in the oxide thin film e.g. $SrTiO_3$ [31, 1-2].

Since the STO films are deposited on single crystal STO substrates, as described above, it can be problematic to extract and tell between the substrate and the thin film. For that reason a fitting procedure is applied to extract the thin film information.

For the XRD measurement a *Phillips PW 3020* diffractometer was used with a Bragg-Brentano geometry. The X-ray spectrum consists of two wavelengths namely Cu $K\alpha_1$ with and $K\alpha_2$ with a satellite peak $K\alpha_{Sat}$. A typical X-ray diffraction pattern for the (002) peak of a STO single crystal

is shown below. The wavelength spectrum of the copper anode must be considered in the analysis of the epitaxial films which comprises also the tail of the bremsberg.
Utilizing Voigt fits [56] the XRD spectra can be fitted for the substrate and the thin film. It is not always expected that the lattice parameter of the STO thin film coincides with the substrate lattice parameters. A change of the lattice parameter is detected by determining the out-of-plane lattice parameter.
Figure 4-7 below depicts the XRD pattern of a homoepitaxial STO system with a 200 nm thick STO film that exhibits a c-axis lattice expansion. The expansion can be assessed by the 2Θ value of the (002) STO film peak.

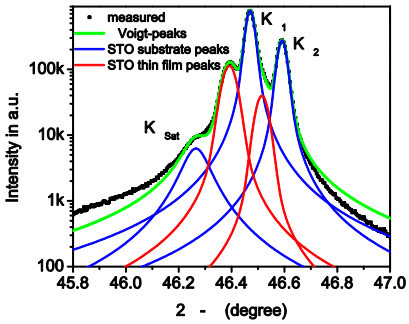


**Figure 4-7:** XRD signal for a homoepitaxial STO film with the fitted XRD peaks for the substrate and the thin film. The STO thin film exhibits in this case an increased out-of-plane lattice parameter compared with the STO substrate.

## 4.3 Positron annihilation analysis

As established before in chapter 2, vacancies are the primary point defects in perovskites and STO respectively. These vacancies can be investigated by utilizing a positron beam. Positron annihilation analysis can have sub ppm level sensitivity and can even provide local structure information. Vacancy-related defects represent an attractive potential for positrons to trap. The probability of trapping is dependent on the defect charge state. When a positron is implanted into the condensed matter and trapped, it annihilates with an electron after a specific lifetime τ and emits two 511 keV γ–rays [57]. The experimental setup is shown below.

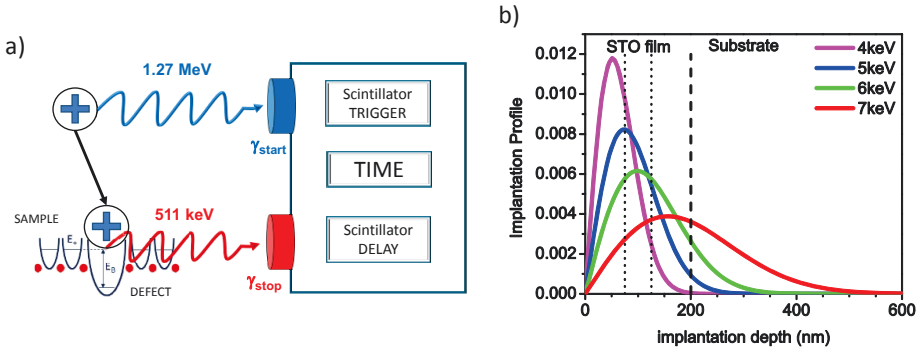


**Figure 4-8: a)** Experimental setup of positron annihilation lifetime measurement **b)** Mahkovian implantation profile for positrons in $SrTiO_3$.

The Mahkovian implantation profiles for positron with different energies are shown above. The profiles broaden with increasing implantation energy. The mean implantation depth of the positrons scales with the positron energy as described below, taken from [57].

$$\bar{z} = E^r \frac{A}{\rho} \qquad (4.13)$$

Where $z$ is the mean implantation depth, $A$ and $r$ are empirical values / constants with $A$ = 4.0mg/cm$^2$keV$^{-r}$ and $r$ = 1.6.

### VE-PALS

Positron lifetime measurements can have sub-ppm sensitivity [57] for vacancy defects and provide defect identification by the characteristic lifetimes. Below are the theoretical characteristic lifetimes listed for various defect sites in a STO-system calculated with DFT by Mackie et al. [58].

| Bulk | $V_O$ | $V_{O-O}$ | $V_{Ti}$ | $V_{Ti-O}$ | $V_{Sr}$ | $V_{Sr-O}$ | $V_{Sr-3O}$ | $V_{Sr-Sr}$ | $V_{Ti-O-Ti}$ | $V_{Ti-3O-Ti}$ |
|---|---|---|---|---|---|---|---|---|---|---|
| **151** | 166 | 178 | 195 | 225 | 279 | 283 | 289 | 283 | 247 | 316 |

**Table 4-1:** Characteristic poistiron lifetimes in (ps) for characteristic defect sites in a STO-system determined by DFT.

The lifetime intensity $I$ is the sum of a specific lifetime signal. The ratio of the lifetime intensities is proportional to the ration of the defect concentrations within the system for a common case where there are only two types of trapping defects and their concentrations are higher than the saturation limit (~50ppm).

$$\frac{I_2}{I_1} = \frac{\kappa_{d2}}{\kappa_{d1}} = \frac{\mu_{d2}[d_2]}{\mu_{d1}[d_1]} \qquad (4.14)$$

$\mu$ depicts the defect specific trapping coefficient and $d$ the defect concentration. $\kappa_d$ therefore represents the rate of positron trapping to a specific vacancy defect. The defect specific trapping coefficient $\mu$ depends on the charge of the defect site.

**Doppler broadening analysis**

The basics of positron annihilation by Doppler broadening annihilation is well described in [57] and for STO systems in [59, 60]. In the following the fundamentals and necessary aspects of this technique are described.

As clarified above an implanted positron annihilates with an electron in the bulk upon trapping. The annihilation results in the emission of two, near antiparallel, γ-rays with 511keV. During the annihilation process the momentum of the electron-positron pair $p$ is transferred to the photon pair. The momentum of the annihilating positron-electron pair in the instant of annihilation is sensitive to the local electronic environment of the positron and effects the broadening. The momentum of the positron-electron pair can cause a Doppler shift of the γ-ray energy and depends on the electron momentum.

When a positron is trapped in a vacancy it tends to annihilate with low momentum valence electrons whereas a delocalized positron rather prefers high momentum valence electrons for annihilation. This manifests in the S- and a W- parameter respectively.

The Doppler-broadening for low momentum annihilation in vacancy-type defects is characterized by the line shape parameter S shown below. The S-value represents the fraction of positrons annihilating with the valence electrons for positron-electron momentums $p_L < 3 \cdot 10^{-3} m_o c$. $p_L$ is the longitudinal positron-electron pair momentum.

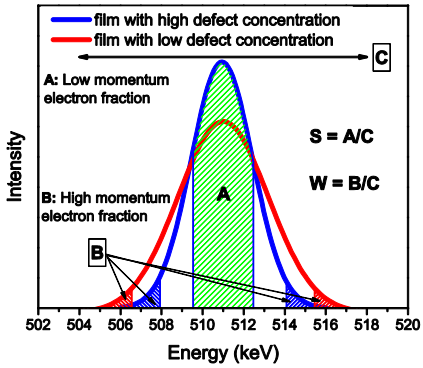


**Figure 4-9:** Doppler-broadening spectra. The S-parameter is described by the ratio of the area of low momentum part of the reference and the sample,
$S_{parameter} = A_{reference} / A_{sample}$.

The S-value is defined as the number of events in the central region of the spectrum divided by the total counts in the 511keV line. The S-parameter is the ratio of the S-value for the reference and the sample with $S = A_{reference}/A_{sample}$.
The S-parameter scales with the positron trapping rate and hence the vacancy defect concentration in a system. Moreover, the S-parameter scales with the size of the vacancy defect.
The magnitude of the S-value increase compared to the reference can provide information on the type and size of defects in a system. The bulk material is denominated with $S_b$ and the bulk positron lifetime of $\tau_b$.

## 4.4 Photo Electron Spectroscopy

Photo (electron) emission spectroscopy techniques were employed to investigate the chemical composition of the oxide and e.g. determine the valence state of ions in the compound. Therefore, X-ray photo-emission spectroscopy (XPS) and Photoelectron emission microscopy (PEEM) are utilized. With PEEM, an imaging of the photoelectrons is possible where secondary emission electrons are used for analysis.

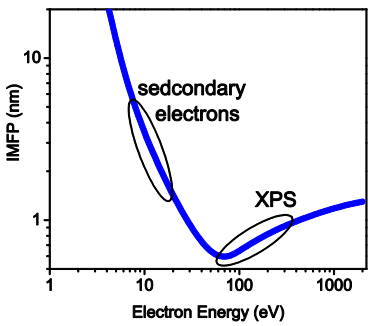


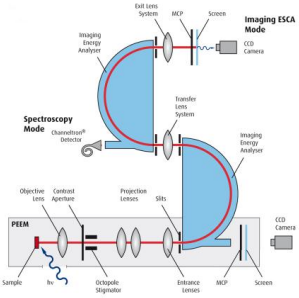


**Figure 4-10: a)** Inelastic mean free path (IMFP) of photo electrons *adopted from [61]*. **b)** Schematic working principle of a PEEM setup - *Taken from Omicron Brochure for NanoESCA 500-V01/2007.*

***XPS***

The monochromatic radiation for XPS analysis is 1.486keV (Al-$K_\alpha$) which results in photoelectrons from depth of ~1nm. Therefore XPS results are very surface sensitive. The binding energy $E_{bind}$ of the emitting atom can be identified by subtracting the measured kinetic energy $E_{kin}$ of the photoelectron and the work function $W$ from the monochromatic x-ray radiation hν, as shown in equation (4.15). The detailed working principle of XPS can be found in [61].

$$E_{kin} = h\nu - E_{bind} - W \qquad (4.15)$$

***PEEM***

With PEEM, secondary electrons are not only detected but imaged. This is possible by employing electron optics to project the photoelectrons onto a screen as depicted in the schematic above in Figure 4-10 (b). Because secondary electrons have a lower energy the information depth is about 2nm – 8nm and chemical information from deeper within the material can be gathered. The gathered information can be directly imaged by electronic lenses onto a screen and monitored with a CCD camera. Energy filter imaging is made possible by a second energy filter.

## 4.5 SPM Analysis

For the electronic and topographic characterization of the oxide films a quasi in-situ SPM tool was applied to carry out Atomic force microscopy (AFM) and Scanning tunneling spectroscopy (STS).

***Local conductivity AFM (LC-AFM)***

LC-AFM was employed to probe for the surface topography and the electrical properties of the oxide on the nano-scale simultaneously. Therefore a cantilever with an AFM-tip made of Pt/Ir coated Si or boron doped diamond (BDD) coated Si tip is scanned over the substrate surface. A SEM picture of a BDD-AFM-tip is shown below in Figure 4-11 with a tip radius of ~10nm.

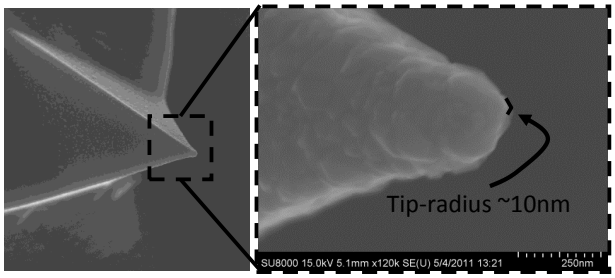


**Figure 4-11:** Diamond (boron doped) coated Si tip. Only the outermost tip touches the surface and therefore the tip has a radius of ~10nm

The AFM-tip is scanned over the substrate surface in contact mode, where the tip touches the surface and the normal force $F_N$ is kept constant. The operating principle is depicted in Figure 4-12.

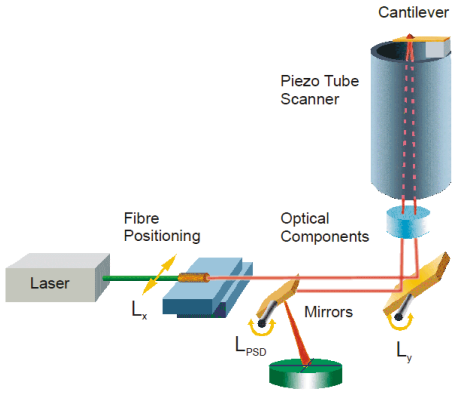


**Figure 4-12:** Working principle schematics of the AFM tool. A laser is positioned by adjusting the fiber $L_x$ and the $L_y$-Mirror onto the backside-end of the AFM cantilever. From the cantilever the laser is reflected back onto the position sensitive detector (PSD). When the AFM-tip is scanned by the Piezo over the sample surface and disturbed by the sample topography the PSD detects this and converts this into a topography signal.
*Picture taken from the OMICRON user manual VT AFM XA User's guide V4.1.*

When the AFM-tip is scanned over the surface and interacts with an obstacle the cantilever is distorted and the laser reflection deflected. The piezo reacts upon the deflection of the laser spot on the PED and corrects the distortion. This signal is used to picture the topography of the surface.

For electrical testing the cantilever is biased with a voltage whereas the substrate holder is grounded. The equivalent circuit diagram is shown below.

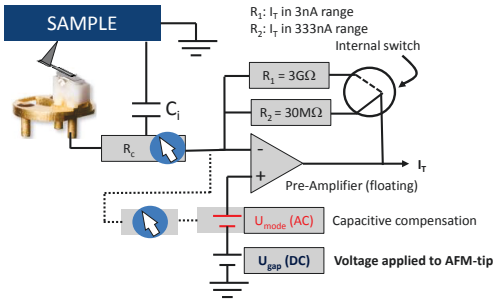


**Figure 4-13:** Circuit diagram for low conductivity AFM (LC-AFM) with Pre-Amplifier. $R_C$: contact resistiance, $C_i$: internal capacitance, $U_{gap}$: applied voltage, $I_T$: Pre-Amplifier Signal

The circuit diagram in Figure 4-13 shows that the electric measurement can be distorted by the parasitic internal capacities $\boldsymbol{C_i}$ and especially the contact resistance $\boldsymbol{R_C}$. This makes it difficult to determine the "true" current values since $\boldsymbol{R_C}$ can vary during the scan and for different setups. Especially for ultra-fast voltages the parasitic capacities can cause an overshot of the voltage during the first few nanoseconds especially for highly resistive surfaces. A high $\boldsymbol{R_C}$ also leads to a current signal drifting in the opposite direction of the physical cause.

***Scanning tunneling microscopy/spectroscopy (STM)/(STS) analysis***

STM and STS is powerful tool for surface analysis and detection local density of electronic states (LDOS) respectively. For the STM/STS measurements the same setup as described above is used where the Pre-Amplifier signal is used to control the piezo. For STM analysis an atomically sharp probe is normally utilized. For reasons explained later the LC-AFM tip was employed for STS analysis on treated oxide surfaces.

The STS measurements are conducted in a UHV atmosphere ($10^{-10}$mbar). The tip is biased with a gap voltage of $\boldsymbol{U_g}$ = 1.5V – 2.5V and $\boldsymbol{I_{Tunnel}}$ = 200pA for the approach of the tip towards the conducting STO film surface where the tunnel current $I_{Tunnel}$ is the control parameter.

If the oxide doesn't exhibit any electric conductivity at all, tunneling microscopy/spectroscopy is not possible.

# 5 Defect formation & accommodation in homoepitaxial $SrTiO_3$ thin films

Stoichiometric variations and defects play a crucial role in complex oxides and determine their physical properties. For complex oxide systems the incorporation and accommodation of defects usually go hand in hand with the development of non-stoichiometry. The defect chemistry of oxides elucidates this intricate relationship. Therefore, the control of stoichiometry for an oxide thin film is imperative for the engineering of functional oxide (hetero-) structures and its defect structure respectively.

## 5.1 Influence of PLD growth parameters on the defect formation

A common way to deposit such oxides is the pulsed laser deposition (PLD) technique. It was shown in the past [1, 10] that by the variation of the PLD process parameters the stoichiometry of a STO thin film can be varied and the physical properties modified. The effect of various PLD conditions on the defect configuration in the STO thin films will be explored in the following. The PLD process, the analysis methods and the results on the defect configuration will be presented.

### 5.1.1 Laser fluence variations

The effect of the laser fluence variation on the thin film stoichiometry of homoepitaxial $SrTiO_3$ thin films was demonstrated before by [1]. There, it was inferred that cation non-stoichiometry in homoepitaxial STO thin films is a function of laser fluence and leads to lattice parameter deviations. By EDS measurements it was concluded that for low fluencies the STO film is Sr-rich and Ti-rich for high laser fluencies. The expansion of the STO c-axis parameter due to non-stoichiometry and the formation of $2^{nd}$ phases are also discussed by [62, 32, 63]. It is assumed that cation vacancies and $2^{nd}$ phase formation is responsible for the lattice expansion. The effect of anion defects i.e. oxygen vacancies on the STO lattice parameters were described [64], calculated [31] and experimentally confirmed [2] to have no measurable effect. The origin of the stoichiometry shift with laser fluence is not clarified yet. Dam et al. [65, 66] argue that there should be a "threshold fluence" where stoichiometric ablation occurs. On the contrary, Ohnishi et al. [1] demonstrate that there is only a specific fluence where the STO thin film exhibits a stoichiometric composition.
In the following the formation and origin of non-stoichiometric deposition and the formation of defects in the thin film are investigated by varying the laser fluence.

The formation of defects is basically restricted to the development of Schottky defects since Frenkel defects are energetically not achievable in a Perovskite. The Schottky type defects are probably vacancy type defects, either cation vacancies or anion vacancies [67][16, 68]. The deposition parameters were varied slightly for various fluence experiments and are given below.

| Parameter | notation | Values & units |
|---|---|---|
| **Laser Fluence** | $F_L$ | $0.6J/cm^2 – 2.5J/cm^2$ |
| **Laser Fluence for deposition of stoichiometric STO thin films** | $F_{LS}$ | -- |
| **Background pressure** | $P_{O2}$ | 0.1mbar – 0.2mbar |
| **Substrate Temperature** | $T_S$ | 720°C – 800°C |
| **Target – Substrate Distance** | $D_{TS}$ | 40mm – 48mm |
| **UV-laser Frequency** | $f_L$ | 1Hz – 5Hz |
| **STO thin film thickness** | $d_{STO}$ | ~ 200nm |

**Table 5-1:** PLD parameters used within the laser fluence sequence

### *5.1.1.1 XRD analysis*

Homoepitaxial STO thin films with $d_{STO}$ ~ 200nm were examined by X-ray diffraction to determine the out-of-plane lattice parameter of the STO film. $2\Theta - \omega$ scans were carried out at the $SrTiO_3$ (002) diffraction peak. Figure 5-1 (a) & (b) shows the X-ray diffraction patterns and the corresponding c-axis lattice parameters of the STO thin films.

.

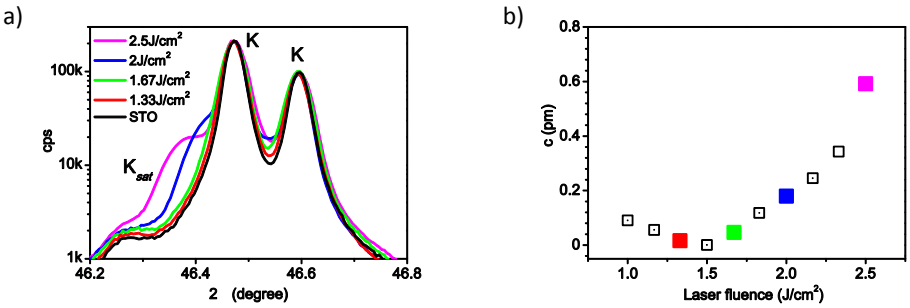


**Figure 5-1: a)** $2\Theta - \omega$ XRD intensity profile around the STO (002) peak for different laser fluencies. **b)** c-axis lattice expansion $\Delta c = c_{film} - c_{STO\text{-}bulk}$ for different laser fluencies. $T_S$: 720°C, $p_{O2}$: 0.2 mbar, $f_L$: 5Hz.

When the c-axis lattice parameter of the film and substrate do no coincide the $2\Theta - \omega$ scan reveals a shift of the $K\alpha_1$ peak for the STO film as can be seen by the bump in the 002-peak in Figure 5-1 (a). The XRD peaks were fitted as described before to decipher the film peak value from the substrate value. The STO films reveal an out-of-plane lattice expansion which depends on the laser fluence as can be seen in Figure 5-1(b). Applying the findings from [1] to the actual results the STO films are Sr-deficient for fluencies > $1.5J/cm^2$ and Sr-rich for $F_L < 1.5J/cm^2$. At $1.5J/cm^2$ where the lattice expansion is essentially zero the Sr/Ti ratio in the STO film is ~ 1.

To search for any possible lattice expansion of the in-plane lattice parameters (a & b) a reciprocal space map was taken for the STO (103) peak for the STO film deposited with 2.5J/cm$^2$.

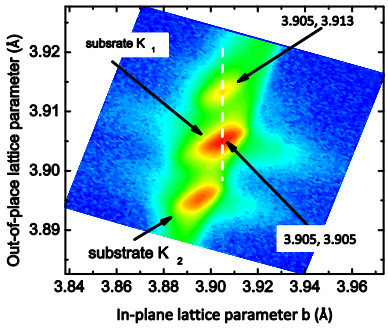


**Figure 5-2:** Reciprocal space map for the STO film grown at $F_L$: 2.5J/cm$^2$ around the STO (103) peak.

The reciprocal space map in Figure 5-2 demonstrates that the in-plane lattice parameter ***b*** still exhibits the bulk parameter of 3.905 Å. Consequently the same should be true for the other in-plane lattice parameter ***a*** and the STO thin film is therefore indeed homo-epitaxial.
Since the lattice parameters ***a*** and ***b*** remain constant and only the out-of-plane lattice parameter ***c*** exhibits an elongation, the unit cell volume effectively increases and the film is therefore strained.

### *5.1.1.2 Positron annihilation lifetime spectroscopy (PALS) investigations*

By using PALS, Schottky defects i.e. cation vacancies ($V_{Ti}''''$ & $V_{Sr}''$) can be identified in the STO thin film. Schottky defects can be a result of the non-stoichiometric deposition of the STO thin films. Variable energy (VE) PALS measurements were performed on the STO films grown at fluencies 1.17 – 2J/cm$^2$ and the positron beam energy was varied in between 1keV – 18keV. Each lifetime spectra contained > 5x10$^6$ counts accumulated with a count rate of ~6x10$^3$s$^{-1}$. The acquired positron lifetimes were analyzed to find the 3 lifetimes with the best $\chi^2$ values.

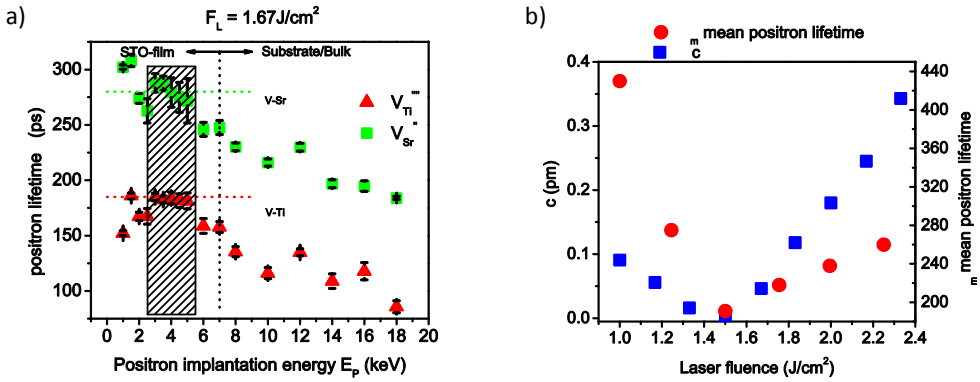


**Figure 5-3: a)** VE-PALS positron lifetime τ - depth profiles (τ - $E_P$ plot) for STO deposited at $F_L$ = 1.67J/cm². The shaded area depicts the range over which the lifetime is averaged for all STO films to retrieve the mean positron lifetime $\tau_m$. **b)** Mean positron limetimes $\tau_m$ vs. lattice expansion for STO films deposited at different laser fluencies.

The variation of the mean positron lifetimes $\tau_m$ for various STO films is shown in Figure 5-3 (a). The mean positron lifetimes are all greater than the lifetime of STO bulk (~155ps) and indicate that all STO films contain vacancy type defects.

The plateaus for the mean positron lifetimes for positron energies from 2.5keV – 5.5keV plotted in Figure 5-3 (a) nicely demonstrate that the defect concentration within the thin film is fairly constant. These plateaus will never be completely straight, even for a constant defect concentration in the film due to the implantation profiles shown in the Makhovian positron implantation profiles shown in chapter 4.3. Figure 5-3 (b) depicts the mean positron life times vs. laser fluence along with the lattice expansion.

Mean positron lifetimes up to 280ps are in the realm of mono-vacancy lifetimes, also see Table 4-1. STO films grown for $F_L \geq 1.5 J/cm^2$ show lifetimes up to 280ps (see Figure 5-3 (b)) whereas the STO films below the optimum fluence $F_{LS} = 1.5 J/cm^2$ exhibit lifetimes beyond 280ps up to 430ps indicating the existence of vacancy clusters for the Sr-rich STO films.

All spectra for the STO thin films were taken above the saturation trapping limit which indicates that the vacancy defect concentration in all STO thin films is higher than in the STO bulk single crystal, surpassing the limit defined by $\mu_d [d]_{Sat} \tau_b \sim 10$. When saturation trapping occurs all implanted positrons trap and therefore it is not possible to determine the absolute defect/vacancy concentration in the system. Even the stoichiometric STO film which exhibits no c-axis expansion showed saturation trapping.

The VE-PALS studies of Keeble et al. [69] on MBE deposited La doped STO films demonstrated that saturation trapping sets on when the vacancy concentration exceeds about 20 – 50ppm.

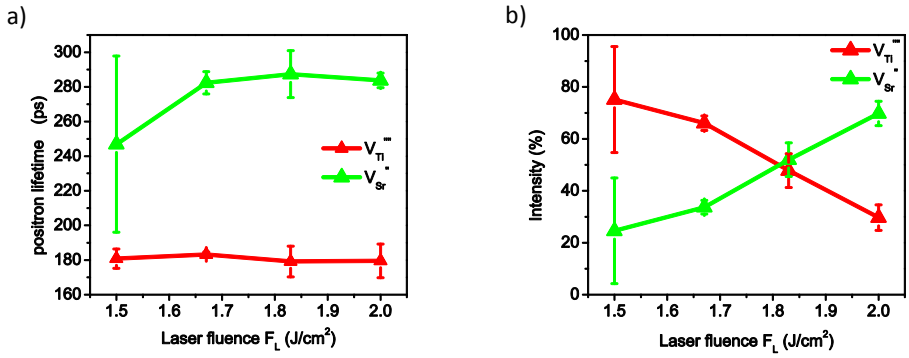


**Figure 5-4: a)** Deconvolved positron lifetimes vs. laser fluence for STO films with $F_L$ > 1.5J/cm². **b)** Relative lifetime intensities of the deconvolved positron lifetimes vs. laser fluence.

By deconvolving the mean positron lifetimes for positron energies between 3keV – 5keV for the films grown at 1.5J/cm² - 2J/cm² two distinct vacancy defect lifetimes can be determined shown in Figure 5-4 (a) namely, $V_{Ti}''''$ with a lifetime of ~180ps and $V_{Sr}''$ with a lifetime of ~280ps. The corresponding relative intensities of the lifetime signals are plotted in Figure 5-4 (b).

The intensity of the strontium vacancies $V_{Sr}''$ increases with the laser fluence suggesting that STO films become virtually Sr-deficient. Additionally, the intensity of $V_{Ti}''''$ decreases with increasing laser energy which demonstrates that the Ti-content in the films above 1.5J/cm² scales with laser energy. The detected lifetimes add up with the EDX measurements in [1].

At 1.5J/cm² the plot in figure Figure 5-4 (b) displays a higher intensity of $V_{Ti}''''$ than for $V_{Sr}''$ lifetimes. However, the trapping coefficient of titanium vacancies $\mu(V_{Ti}'''')$ is higher than the one of strontium vacancies $\mu(V_{Sr}'')$ because of the higher negative charge of $V_{Ti}^{4-}$ versus $V_{Sr}^{2-}$. The value of $\mu(V_{Ti})$ was estimated to be;

$$\mu(V_{Ti}) \sim 3.6 \cdot \mu(V_{Sr}) \qquad \textbf{(5.1)}$$

With equation (4.14) the PALS measurements yield at 1.5J/cm² that the concentration of $V_{Sr}''$ and $V_{Ti}''''$ are equal, $[V_{Sr}'']/[V_{Ti}''''] \sim 1$. Films grown below 1.5J/cm² exhibit a much higher mean positron lifetime. Such enlarged lifetimes could indicate the existence of open volume defects in the film such as nano-voids [59], since their lifetimes are even beyond the lifetimes of the more complex di-, tri- & quadruple vacancy complexes from Table 4-1.

By deconvolving the mean lifetimes for the films at 1.33J/cm² and 1.17J/cm² and fixing 2 of the lifetime values at 281ps for $V_{Sr}''$ and 181ps for $V_{Ti}''''$ a third lifetime component can be fitted which is ~377ps ($I_3$ ~ 16%) and ~410ps ($I_3$ ~ 48%) respectively for the films 1.3J/cm² and 1.17J/cm². As shown in Table 4-1, a 5-fold vacancy comprising 1 Ti-, 1 Sr- and 3 oxygen vacancies result in a DFT determined lifetime of ~316ps. Since the lifetime values obtained for the Sr-rich films are much higher than 316ps the vacancy lacunae must contain more than 5 vacancies.

Vacancy clustering studies in silicon for example [70] reported for a 5-fold vacancy a lifetime of 355ps (similar to the 316ps) and for lifetimes of 420 – 430ps a vacancy cluster comprising 10 – 14 vacancies. Therefore the lifetimes measured for the Sr-rich films indicate fairly large vacancy clusters that can include up to 14 vacancies. Plotted below are the deconvolved lifetimes and their intensities for the complete fluence sequence with $p_{O2}$ = 0.1mbar and $T_S$ = 720°C.

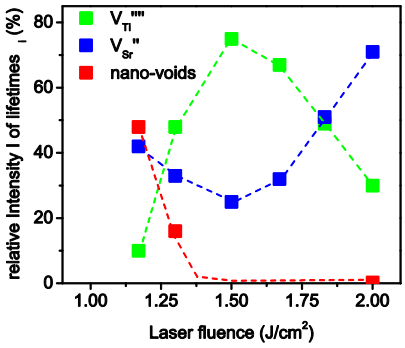


**Figure 5-5:** relative intensities of different cation vacancy lifetimes ($V_{Ti}''''$, $V_{Sr}''$, nano-voids) for STO films with 1.17J/cm² ≤ $F_L$ ≤ 2J/cm². The trapping coefficient is not considered in this graph.

When reading Figure 5-5 one must keep in mind that the relative lifetime intensities do not represent vacancy concentrations because the trapping coefficients of the vacancy types are different as established above. What seems very intriguing about the positron lifetime intensities shown in Figure 5-5 are the abrupt changes in the gradient of $V_{Sr}''$ & $V_{Ti}''''$ for the films below 1.5J/cm².

The intensity of $V_{Ti}''''$ films should intuitively keep rising since the films become increasingly Sr-rich [1]. The equivalent should be true for $V_{Sr}''$ which should further decrease the more Sr is incorporated into the STO films. However, the contrary appears to be the case for Sr-rich STO films. The concentration of $V_{Sr}''$ actually increases with increasing Sr content in the STO film. This increase of $[V_{Sr}'']$ can actually be explained with the formation of an additional SrO plane according to the equation below [71] which takes place either on the surface or within the crystal.

Surface reaction
$$\frac{1}{2}O_2 + 2e' + Sr_{Sr}^x \leftrightarrow V_{Sr}'' + SrO_{2nd-phase} \qquad (5.2)$$

Bulk reaction
$$SrTiO_3 \leftrightarrow Ti_{Ti}^x + V_{Sr}'' + 2O_O^x + V_O^{\cdot\cdot} + SrO \qquad (5.3)$$

The formation of SrO can be understood as a Ruddlesden-Popper type defect. The required electrons for this reaction might originate from $V_{Ti}''''$ in the TiO-layer which is replaced by the formation of a SrO-layer creating a planar fault.

This also means that the formation of a SrO-layer is facilitated by the existence of $V_{Ti}''''$ and especially $V_{Ti}''''$-clusters. Such clusters actually are very likely to exist since the positron data with lifetime components of τ > 300ps not only for the film grown at 1.17J/cm² but also for the STO film grown at 1.3J/cm² the existence of vacancy-clusters comprising about 10 – 14 vacancies as shown above. The kind of vacancies that are enclosed in such a cluster cannot be distinguished.

It is assumed however, that the absolute majority must be $V_{Ti}''''$ since the growing STO film is fed by a Ti-deprived STO plume (as will be shown later). The surface reaction of equation (5.2) would explain the increase of $[V_{Sr}'']$ and the drop of $[V_{Ti}'''']$ in Figure 5-5. The same applies to the bulk reaction (5.3) which is consistent with the cation vacancy trend in Figure 5-5.

For a specific laser fluence $F_{LS}$ where $\Delta c = 0$ the PALS data reveal that $[V_{Sr}'']/[V_{Ti}''''] \sim 1$. At $\Delta c = 0$ the concentration of $V_{Ti}''''$ is at its maximum. For $F_L > F_{LS}$ the STO films become Ti-rich and the concentration of $[V_{Ti}'''']$ actually decreases. Therefore $[V_{Sr}'']/[V_{Ti}''''] > 1$ for excess Ti-films.
STO films exhibiting an excess of Sr show the same ratio where $[V_{Sr}'']/[V_{Ti}''''] > 1$ due to the formation of Ruddlesden-Popper phases, see equation (5.2). Consequently we can write the following equation which represents the c-axis expansion as a function of the cation vacancy ratio in STO.

$$\Delta c \sim 1 - \left( \frac{[V_{Sr}]}{[V_{Ti}]} \right) \quad \text{with} \quad [V_{Sr}] + [V_{Ti}] = 1 \tag{5.4}$$

These interpretations and measurements above however, can hardly be combined with the theoretical computations from [31] where both types of vacancy defects are supposed to expand the lattice due to Coulomb interactions that cause a strain effect. More important, according to these calculations the strain effect of $V_{Ti}''''$ on the STO lattice is supposed to be ~13 times larger than the strain effect of $V_{Sr}''$ and the lattice expansion should be a function of $V_{Ti}''''$. PALS data rather suggest that the lattice expansion scales with $[V_{Sr}'']$, see Figure 5-5.

#### *5.1.1.3 TEM analysis of STO thin films*

The PALS studies above revealed that STO films above $F_{LS}$ exhibit dominantly isolated cation vacancies with an increasing $[V_{Sr}'']/[V_{Ti}'''']$ ratio for non-stoichiometric films.
STO films grown below $F_{LS}$ showed strong indications of vacancy clustering with mean positron lifetimes > 300ps up to 430ps which indicated the formation of nano-voids or other extended defects which could be the result of the formation of Ruddlesden-Popper phases.
To proof and visualize the defects in the STO films, (scanning) transmission electron microscopy (STEM) was employed to image the crystal structure of the STO films. Changes in the crystal structure were observed using high-angle annular dark-field (HAADF) imaging technique based on STEM and high-resolution transmission electron microscopy (HRTEM) technique. Three STO films were investigate and are presented below (1.17, 1.5 and $2 J/cm^2$).

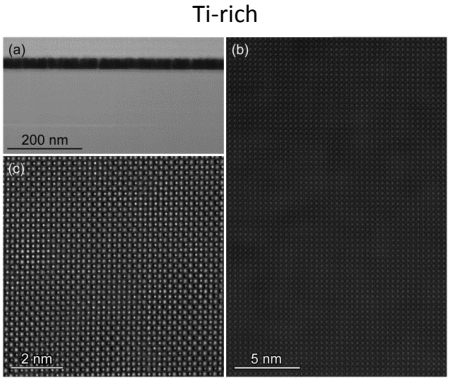


**Figure 5-6**: images of $SrTiO_3$ film grown at $F_L$: 2 J/cm², **(a)** Low magnification overview, **(b)** HAADF, and **(c)** HRTEM

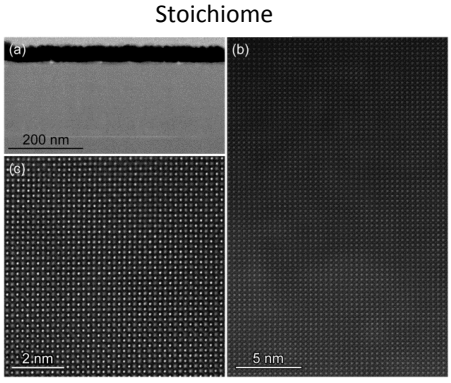


**Figure 5-7:** images of $SrTiO_3$ film grown at $F_L$: 1.5 J/cm², **(a)** low magnification overview, **(b)** HAADF, and **(c)** HRTEM

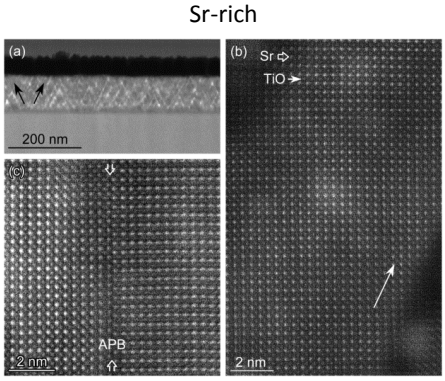


**Figure 5-8:** images of $SrTiO_3$ film grown at $F_L$: 1.17J/cm², **(a)** low magnification overview, arrows indicate the <112> direction **(b)** HAADF image of a STO grain with the arrow indicating the <112> direction. **(c)**HAADF image shows an anti-phase boundary (APB) due to the incorporation of an additional SrO plane into the STO.

*Measurement performed at the ERC by Jja & Du*

The films in Figure 5-6, Figure 5-7 and Figure 5-8 above, exhibit in the HRTEM pictures columns with a brighter contrast indicating SrO-columns and weaker ones indicating TiO-columns. The two STO films grown at $F_L$ = 1.5J/cm² and $F_L$ = 2J/cm² in Figure 5-6 & Figure 5-7 show basically no differences in the crystalline structure. This is consistent with the PALS observations where only lifetimes of single vacancies were detected. Such isolated defects are almost impossible to detect by TEM especially since the defect concentration is in the ppm range. Both films appear to have no perturbation or segregations in the lattice and therefore can be seen as a perfect addition to the single crystal STO substrate.

More interestingly is the crystalline morphology observed for the STO film grown at $F_L$=1.17J/cm² in the extremely Sr-rich region, see Figure 5-8. The positron data for this film indicated the existence of nano-voids. The intensity for $V_{Ti}''''$ was controversially lower than the intensity of $V_{Sr}''$ for this film. Already in the low magnification overview in Figure 5-8 (a) the formation of <001> textured STO grains can be observed. These grains show a distinct growth

orientation in the <112> direction, also see arrows Figure 5-8 (a) & (b) and overlap eventually forming grain boundaries (GB). Smaller miss-orientations lead to small angle boundaries between the grain formed by the insertion of half-planes. In Figure 5-9 (c) the insertion of such a plane can be observed in the form of a SrO-plane. A TiO-layer is missing and an anti-phase boundary is formed resulting in the formation of a double SrO layer and hence, the formation of a Ruddlesden-Popper (RP)-like phase.

When a TiO-layer vanishes the $V_{Ti}''''$ within such a layer vanish as well which would explain the sharp drop in the $V_{Ti}''''$ intensity shown in Figure 5-5. The formation of the SrO plane can cause the formation of $V_{Sr}''$ as depicted in equation (5.2) & (5.3).

### 5.1.2 Variation of the target – substrate distance

In order to investigate the origin of the two regions of non-stoichiometry with the distinct transition fluence ($F_{LS}$) observed in Figure 5-1 for 1.5J/cm$^2$, an attempt was taken to elucidate the cause of the difference by varying the target to substrate distance $D_{TS}$. The results of the XRD analysis are presented below.

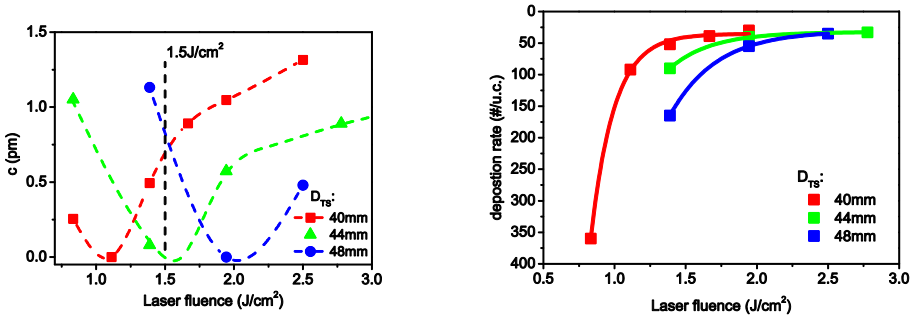


**Figure 5-9: a)** c-axis expansion of STO thin films $d_{STO}$~200 nm at different laser fluencies and various target to substrate distance $D_{TS}$ **b)** Growth rates of the STO films. All samples were grown on STO with TS: 800ºC, $p_{O2}$: 0.1mbar, $f_L$: 5Hz

Figure 5-9 (a) shows the c-axis expansion of STO films grown for different laser fluencies and substrate to target distances. The films in Figure 5-9 (a) show that $F_{LS}$ shifts systematically with $D_{TS}$. By applying the findings from PALS analysis from chapter 5.1.1 and [1] a STO thin film grown at 1.5J/cm$^2$ for example can be either Ti-rich ($D_{TS}$ = 40mm), stoichiometric ($D_{TS}$ = 44mm) or Sr-rich ($D_{TS}$ = 48mm) depending on the target to substrate distance. These findings would indicate a combination of two effects to be responsible for the stoichiometry shift; firstly a "time of flight" effect that comprises preferential scattering of a plume species [72] during the propagation of the plume from target to substrate and secondly, an incongruent ablation of the target that was observed by Dam et al. in [65] before.

It was reported that separation of species during the plume propagation [73, 74] occurs and it is suspected that such a separation is responsible for the observed shift in the STO lattice expansion and the shift of the film stoichiometry respectively.

### 5.1.3 $O_2$ background pressure variations

As described by [75] the background pressure has a profound effect on the PLD process. That is in part due to the braking and confinement of the plume and the scattering of plume species during their transport towards the substrate by gas molecules which is in turn a function of the background gas density. Shimoyama et al. reported in [76] that homoepitaxial STO films can be grown by supplying only metallic atoms i.e. Ti and Sr to the growing film. The necessary oxygen is being supplied by the substrate by so called automatic feeding for temperatures as low as 370°C. This basically allows for the deposition of $SrTiO_3$ even at extremely low $O_2$ partial pressure.

In this chapter the effect of the $O_2$ background pressure on the STO film stoichiometry with its defect accommodation is presented. The pressure in the vacuum chamber was changed by adjusting the flow by a needle valve or a mass-flow controller for $10^{-7}$mbar < $p_{O2}$ < $5{\cdot}10^{-3}$mbar and adjusting additionally a throttle valve for $5{\cdot}10^{-3}$mbar < $P_{O2}$ < 0.5mbar.

#### *5.1.3.1 XRD analysis*

For x-ray diffraction analysis 3 different sequences were analyzed. Each sequence was deposited at a different laser fluence ($F_L$: 1J/cm², 1.4J/cm², 2J/cm²).

The deposited STO films with $d_{STO}$ ~ 200nm were investigated by X-ray diffraction to determine the c-axis lattice parameter of the film. 2Θ – ω diffraction patterns were taken for the $SrTiO_3$ (002) diffraction peak.

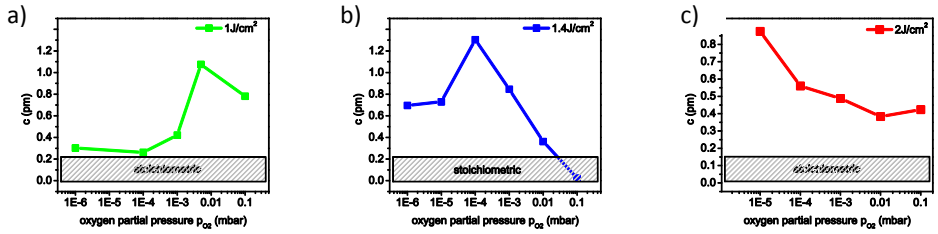


**Figure 5-10:** out-of-plane lattice expansion of STO thin films grown for different $O_2$ background pressures and laser fluencies. **a)** $f_L$: 1J/cm², **b)** $F_L$: 1.4J/cm², **c)** $F_L$: 2J/cm². The shaded area marks a stoichiometric STO film. With $T_S$: 800°C, $f_L$: 5Hz

The trend of the lattice expansions in Figure 5-10 for different laser fluencies visualize the variation of the Sr/Ti ratio of the STO film as function of pressure and laser fluence. The same trend for different laser fluencies and background pressures were observed by Liu et al. in [77] however with the conclusion that preferential sputtering is responsible for the change in thin film stoichiometry. Since the variation of the target to substrate distance in chapter 5.1.2 indicated preferential scattering as an origin of the stoichiometry variation of the STO thin film we suspect that the variation of the background pressure influences the scattering events and therefore the resulting STO film stoichiometry.

Moreover, the deposited STO films exhibited a gradual color change with decreasing pressure indicating a regular loss of oxygen with decreasing pressure. The color change indicates a reduction of the STO system with a removal of oxygen. This thermally activated process however should occur for very low oxygen partial pressures ($p_{O2} < 10^{-18}$mbar) and at temperatures T > 1000°C [17, 78].
The oxygen partial pressure in the vicinity of the specimen during growth must be for this reason much lower than the denominated pressure in the chamber. Also oxygen exchange kinetics and reactions on the STO surface can be enhanced by the impact of energetic plume particles [79]. Also if the uptake of oxygen from the ambient is too slow the growing STO film is readily reduced. For both cases an oxygen concentration gradient between the growing film and the substrate could lead consequentially to a diffusion of oxygen from the substrate towards the thin film. The transition when a growing homoepitaxial STO film is fed with oxygen by the STO substrate or by the ambient is mentioned in [80].

### *5.1.3.2 Positron annihilation by Doppler broadening analysis*

STO thin films deposited at $F_L = 1.4 J/cm^2$ with $d_{STO} \sim 200nm$ for different $O_2$ background pressures were studied by positron annihilation. The Doppler-broadening spectra were recorded for different implantation energies. Each spectrum contained ~ $10^6$ counts and was characterized by the S-parameter and plotted vs. positron energy. By reducing the background pressure autofeeding epitaxy as described in [76] needs to be considered with decreasing background pressure especially for films grown at $p_{O2}$ pressures < $10^{-6}$mbar.

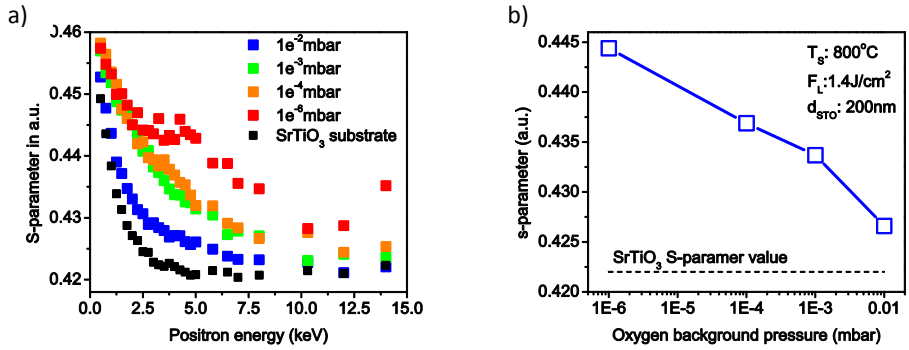


**Figure 5-11: a)** S-parameter as a function of positron energy for various STO thin films deposited at different $O_2$ partial pressures. **b)** S-parameter of STO films for 4keV positron energy vs. different $O_2$ partial pressure. With $F_L$: 1.4J/cm², $T_S$: 800°C, $D_{TS}$: 44mm, $f_L$: 5Hz

The S-parameters for different STO films grown at different $O_2$ background pressures are shown in the S - E plot in Figure 5-11 (a). The positrons trap into the 200nm thick STO film for positron energies between 2.5keV – 5.5keV. Beyond 5.5keV the implantation profile broadens and positrons largely trap into the STO substrate. The S-parameter values for the STO films at 4keV are plotted in Figure 5-11 (b) and demonstrate that the S-parameter value increases with decreasing pressure, $S \sim 1/p_{O2}$ which indicates that the average concentration of point defects in

the STO films increases for decreasing $O_2$ background pressure. The STO films grown at pressures $10^{-5}$mbar < $p_{O2}$ < $10^{-1}$mbar show no distinct plateau region for the S-parameter value in the STO film region (2.5keV – 5.5keV). Plateaus like in Figure 5-3 usually indicate a constant defect concentration.
The S-parameters in Figure 5-11 rather resemble a diffusion profile hinting towards a gradient of the point defects within the STO film. Only the film grown at $10^{-6}$ mbar shows a distinct plateau region and an onset of a plateau can be observed for the film grown at $10^{-4}$ mbar. The type of vacancies cannot be determined however by the Doppler-broadening spectra.
Unfortunately lifetime measurements weren't possible for the background pressure sequence. Therefore a survey of other the results of other researches should help to compare and conclude on the prevalent defect structure in the actual films shown above.

**S-parameter observations**

Helpful Doppler-broadening studies on STO films and crystals were presented in [4, 3, 60, 59]. S-parameter measurements by Uendo et al. [4] on homoepitaxial STO thin films grown under UHV conditions by co-evaporation of Sr and Ti with MBE exemplified the same S - E characteristics as can be seen in Figure 5-11.
It was concluded in [4] that the S-parameter is a measure for the oxygen vacancies in the STO film since the S-parameter value decreased by post annealing in oxygen at 200°C. Oxygen vacancies were found to stretch far into the STO substrate and can even reach the backside of the substrate. Oxygen multi-vacancies $V_{O\text{-}O}$ along with Sr-vacancies $V_{Sr}''$ were also observed in the STO-system and determined by VE-PALS.
The S - E plots from [4] show that the change of the S-parameter after post-annealing (at 200°C) is more pronounced within the bulk for positron energies > 6keV whereas the S-value remains almost unaffected for positron energies < 6keV. This could indicate that oxygen vacancies are more prevalent in the bulk whereas strontium vacancies are in the film and interface. ($V_{Sr}''$ cannot be removed by oxidation at 200°C).
The investigations of McGuire et al. [3] on ~300nm thick STO films deposited at 0.4mbar by PLD showed that the S-parameter value of the film is a result of trapping to Sr-vacancies $V_{Sr}''$ and $V_{Sr\text{-}O}$ di-vacancies. The films were confirmed by EDX to be Ti-rich i.e. Sr-deficient.
The investigations by Gentils at al. [60] also show S-parameter profiles that match the S-parameter profiles shown in Figure 5-11 (a).
In [60] co-doped (La, Sr)$TiO_3$ thin films deposited at $p_{O2}$ = $10^{-6}$mbar, $T_S$ = 750°C are investigated amongst others. The findings are analogous to the ones presented by [4, 3]. The S-parameter value increases and scales with increasing film thickness. A re-oxidized film exhibits a decrease of the S-value but with a much bigger difference for the bulk region for a positron energy ($E_p$) $E_p$ > 7keV than for the film $E_p$ < 7keV suggesting that there are more cation vacancies in the film and the concentration of anion vacancies i.e. oxygen vacancies is higher in the bulk.

The direct comparison of the mean positron lifetime $\tau_m$ (VE-PALS) with the S-parameter (Doppler broadening) for a STO film on STO is presented by Keeble at al. [59]. The S – E plot shows the same pattern as the S – E plots presented by [4] [3] [60] and in Figure 5-11.

**Space charge considerations**

The non-uniform shift of the S-value upon oxidation or post-annealing observed in the works of [4, 3, 60, 59] could lead to the assumption of a concentration gradient of defects within the STO interface. It was postulated in [81, 82] that the formation of defects at the surface is strongly influenced by the local space charge which could lead to the formation of defect concentration profiles also discussed by De Souza in [82] and Gunkel in [22] which are considered in the following.

When a high concentration of oxygen vacancies is formed at the surface (Surface core) a highly positive charge is created which creates a negatively charged space charge layer stretching from the surface into the bulk.

Figure 5-12 shows the schematic concentration profile for a STO system with a high $V_O^{\bullet\bullet}$ concentration in the surface region of the growing STO film.

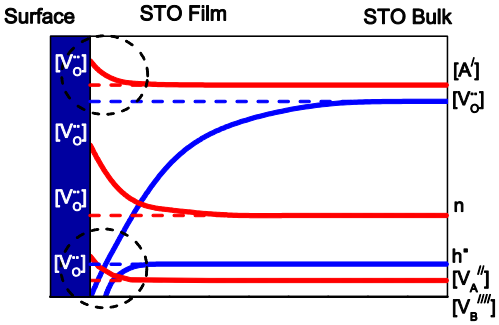


**Figure 5-12**: Schematic space charge profile for acceptor doped $SrTiO_3$ for a heavily reduced STO-film surface region.

For calculating the space charge profiles one can either utilized the Mott-Schottky model or the Gouy-Chapman model. The latter is applied when cations are considered as mobile. Since this is the case for a growing STO system the cations will contribute to the compensation mechanism and could align as depicted in Figure 5-12 (circle). This would result in an increase of the cation vacancies towards the surface. These concentration profiles can actually stretch up to 100 - 150nm into the bulk [82, 22]. Comparing this to the Makhovian implantation profiles, 100nm corresponds to a positron energy of ~6keV and 150nm to ~8keV.

The S – E plots in Figure 5-11 (a) show that the S-value varies/decreases with increasing positron energy and beyond 6 – 8keV the S-value stabilizes. That means in consequence that the S – E profiles fit very well the cation defect profiles depicted above and might resemble the distribution of the defects due to the formation of a space charge zone during growth.

For the film grown at $10^{-6}$mbar the incorporation of $V_O^{\bullet\bullet}$ is extremely high. If the diffusion of cation vacancies is too slow for the deposition process they cannot align properly and the oxygen (core) vacancies are compensated by electrons with $n = 2[V_O^{\bullet\bullet}]$ and the Schottky equilibrium becomes inactive which in consequence can result in a constant $V_{Sr}''$ concentration. This could

cause the S-value to stabilize over a defined region especially where the reduction is extremely high (intrinsic region in the Kröger-Vink diagram).
Combining the S-parameter observations with the consideration for space charge formation the observed S – E in Figure 5-11 (a) profile could be due to the concentration gradient of strontium vacancies as a result of the space charge zone during growth.

### 5.1.4 Influence of substrate temperature on the defect accommodation in STO

As presented earlier, even stoichiometric STO films deposited at $T_S$ = 850°C can enclose a "high" amount of vacancy type defects (> 100ppm) as demonstrated by the saturation trapping of the positrons by PALS.
The presence of defects in a thin film is in part the result of the stoichiometry (defect chemistry) of the thin film and in part a consequence of the growth kinetics. Due to defect chemical reactions defects can be created whereas during thin film growth defects can only be incorporated.
The growth of a film is the development of nuclei by the assimilation of ad-atoms. This process is strongly temperature dependent according to Walton [83]. The perfect growth of a thin film would be the consecutive formation of 2D-monolayers. If the diffusion of ad-atoms is insufficient to reach the edge of the nuclei (monolayer) in a given timeframe further nuclei will form on top of them and a 2nd monolayer evolves before the 1st is finished, see figure below . This marks the transition from a perfect 2D to a 3D thin film growth. This process is known to induce defects.

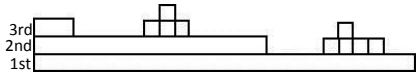


**Figure 5-13:** Formation of islands for the 1st and 2nd monolayer during layer-by-layer growth

By improving the diffusion kinetics of ad-atoms the 2D growth can be sustained. The surface diffusion of ad-atoms $D_S$ is a function of the activation energy $E_{SD}$ and the temperature $T$.

$$D_S = D_0 \exp\left(-\frac{E_{SD}}{kT}\right) \qquad (5.5)$$

By increasing the substrate temperature the surface diffusion increases and the ad-atoms mobility should be enhanced. This in return should facilitate the 2D growth and therefore suppress the incorporation of defects.
If diffusion kinetics are high, ad-atoms can diffuse towards the step edges on the substrate surface without the formation of nuclei which is termed as step-flow growth, see figure below. During step flow growth the step density on the surface doesn't change effectively. Therefore the RHEED signal shows no change in intensity.

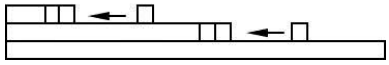

**Figure 5-14:** Step flow growth where ad-atoms diffuse towards the step edges of the vicinal substrate surface.

The homoepitaxial thin film growth of STO was investigate as a function of substrate temperature. The temperature was varied in the range of 650°C – 1150°C. For temperatures above 900°C a special high temperature holder was used, see chapter 3 for details.

### *5.1.4.1 XRD analysis*

For the temperature sequence 3 different laser fluencies were chosen. Therefore a Sr-rich, stoichiometric and Ti-rich films were deposited for different substrate temperatures. The background pressure was kept constant for all processes at $p_{O2}$ = 0.1mbar and the films had a thickness of $d_{STO}$ ~ 200nm. The XRD results are shown below.

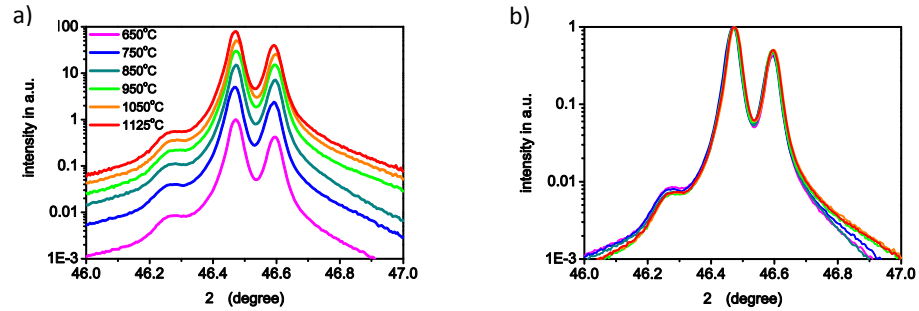


**Figure 5-15:** Stoichiometric STO film **a)** X-ray diffraction patterns for stoichiometric STO films grown at different temperatures. **b)** Juxtaposed XRD patterns from (a) demonstrate no sign of a lattice expansion.

The x-ray diffraction patterns in Figure 5-15 exemplify that the temperature has no profound impact on the cation vacancy ratio for a stoichiometric system. The concentration of defects however should decrease with temperature due to the improved growth kinetics which should result in the reduction in intensity of the x-ray diffraction peak with increasing temperature for an off-stoichiometric STO film.

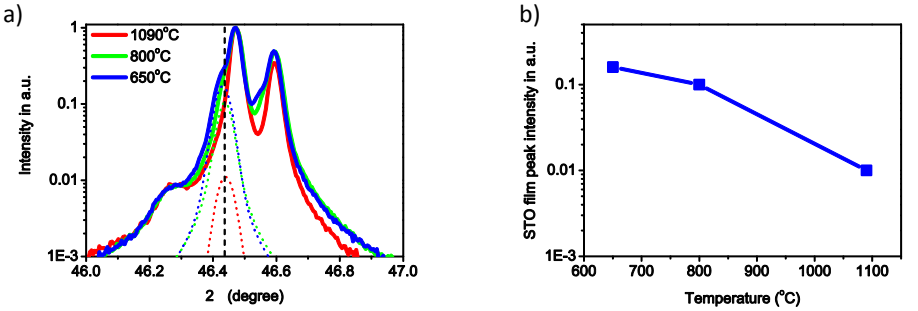


**Figure 5-16: a)** Ti-rich STO deposited for different substrate temperatures. $F_L$ = 1.8J/cm², $D_{TS}$: 40mm, $f_L$: 5Hz. Dotted lines depict the $K\alpha_1$ peaks for the STO films **b)** STO film peak intensity vs. $T_S$.

The XRD analysis for the Ti-rich STO films reveals that the lattice expansion doesn't change effectively with the substrate temperature. That is because the $K\alpha_1$ peaks of the STO thin films have the same 2Θ value. However, the intensity of the STO film peak decreases.

This observation supports the theory, that the lattice expansion of a non-stoichiometric STO film is a result of the cation vacancy ratio. When the defect concentration increases the intensity of the shifted film peak increases and the peak-shift is a result of the defect (cation vacancy) ratio.

## 5.2 Origin of non-stoichiometry in homoepitaxial $SrTiO_3$ thin films

The variation of the non-stoichiometry detected before by positron annihilation and XRD analysis is suspected to originate from the plume and ablation characteristics. Therefore, the plume characteristics were probed by fast optical imaging and the ablation spots on the target and the thin films were investigated by XPS.

### 5.2.1 Non-stoichiometry induced by laser fluence variations

So far there is no reported footage of in-situ PLD plume analysis for $SrTiO_3$ that can explain and connect the shift in thin film stoichiometry with the plume dynamics and the ablation characteristics.

Therefore, optical time resolved plume analysis and spectroscopy was employed for the investigation of the plume kinetics the chemical plume composition separately which was described in detail above in chapter 4.1.3. The propagating plume is imaged with a high speed ICCD camera for several delay times $\tau$ after the UV-laser pulse hits the target. By using a grating the visible emission spectra of the plume can be captured and emission lines can be assigned to different species and their oxidation state. This technique has already been used to investigate the plume dynamics of several complex oxides [47, 75, 84]. First the plume dynamics are investigated and subsequently the spectroscopic results are presented.

2D images of the STO plume are presented Figure 5-17 (a) for different laser fluencies and delay times $\tau$. Each image is normalized to its own maximum intensity. ***R*** denotes the propagation distance normal to the target surface whereas R = 0 represents the target surface. The lateral dimension of the plume is indicated by a value of ***x***.

#### *5.2.1.1 Plume dynamics*

To resolve the temporal evolution of the plume the fronts the methods described in chapter 4.1.3 were utilized. This procedure yields the plot in Figure 5-17 (b) and visualizes the expansion dynamics of the plume front. The plume front dynamics follow the plume propagation model described previously. The lines in figure (b) are the fits according to the propagation model with $\rho_g(T)$, which is described in detail in chapter **5.1.4**. By fitting the propagation the values for $M_p$ and $u_0$ are obtained and presented below.

| | **0.6J/cm²** | **1J/cm²** | **2J/cm²** |
|---|---|---|---|
| **$M_p$ [$10^{-10}$ kg]** | 3.5 | 5.8 | 8.5 |
| **$u_0$ [km/s]** | 9 | 11.8 | 14.2 |

**Table 5-2:** The initial mass $M_p$ and velocity $u_0$ both increase with increasing laser fluence. $p_{O2}$ = 0.1mbar, $T_S$ = 800°C

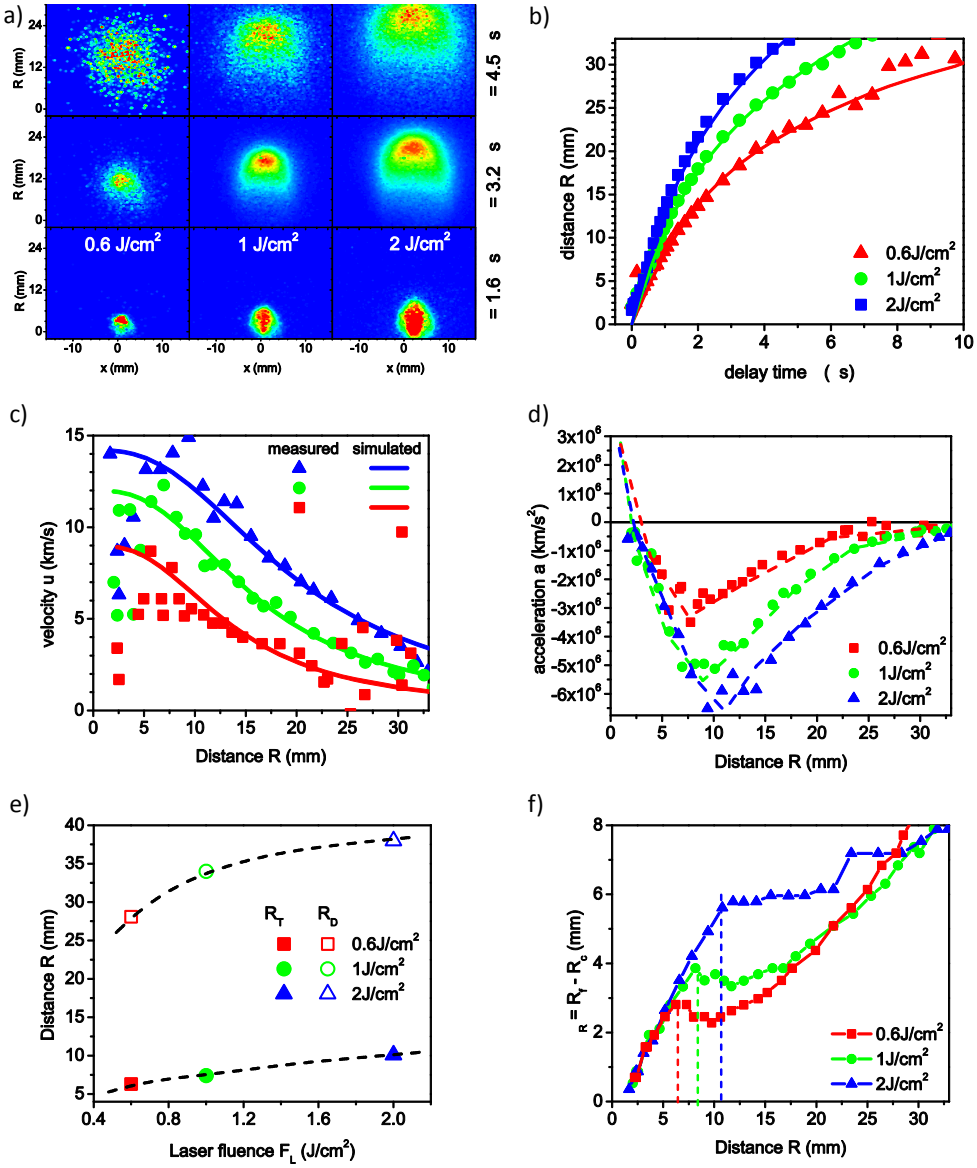


**Figure 5-17: a)** 2D images of the STO plume for different delay times τ and laser fluencies $F_L$. **b)** R-τ plots for the plume fronts at different laser fluencies **c)** Simulated plume front velocity $u_f$ **d)** Simulated plume front acceleration $a_f$ **e)** Transition points $R_T$ from free expansion to shock-wave like expansion, $R_D$ from shock-wave like to diffusion–like expansion **f)** Difference between plume front and plume center vs. travelled distance R. With $p_{O2}$: 0.1mbar, $T_S$: 800°C.

By increasing the laser fluence the plume momentum increases. The plume dynamics in Figure 5-17 (b) demonstrate that the plume is significantly braked by the background gas and eventually stops. Depending on the laser fluence the plume front can stop before it actually strikes the substrate, see $\boldsymbol{F_L}$ = 0.6J/cm$^2$. In this case the plume species only reach the substrate by diffusion. The velocity of the plume front $\boldsymbol{u_f}$ and the plume mass $M_p$ scale with the laser fluence as can also be seen in Figure 5-17 (c) which shows the simulated plume front velocity according to the R – τ data obtained. Figure (d) illustrates the simulated plume front acceleration. (The velocity signal is too noise to be properly illustrated).
The minimum of the $\boldsymbol{a - \tau}$ plot marks the end of the free expansion and the beginning of the shock-wave like expansion. When the acceleration $\boldsymbol{a}$ approaches zero the diffusion like flow sets in and marks the transition position $\boldsymbol{R_D}$. The transition positions from free to shock-wave-like $\boldsymbol{R_T}$ and diffusion-like expansion $\boldsymbol{R_D}$ are plotted in figure (e).

Once the plume starts to interact with the gas molecules the plume front forms a spherical shape and is braked down due to the accumulation of gas molecules and the buildup of a dense gas layer in front of the plume. The plume center however, retains its momentum. When the plume front is braked by the backround gas the plume center keeps its velocity and the distance between plume front and plume center decreases, see Figure 5-17 (f). During this process the plume species between front and center are compressed.
This compression of the plume can be observed by subtracting the plume center position from the plume front position, see Figure 5-17 (f) which yields $\boldsymbol{\Delta R}$. When $\boldsymbol{\Delta R}$ reaches its first maximum the free expansion ends and marks the beginning of a shock wave. This is exactly the same position where the acceleration of the plume exhibits its minimum, compare figure (d) and (f). The compression can cause among other effects a so called plume splitting effect which was observed before for other PLD plumes [53] (LSMO) or [74] (Si) and [73] (STO). The splitting causes a spatial separation of plume species and causes a shift in plume stoichiometry. Plume splitting can be made visible by plotting intensity profiles of the plume emission along the plume center in the direction of expansion, as shown below. When the plume splits it forms additional emission maxima. Non-continuous emission intensity can therefore be an indication of plume splitting. In Figure 5-18 the intensity profiles are plotted for the plumes shown above in Figure 5-17.

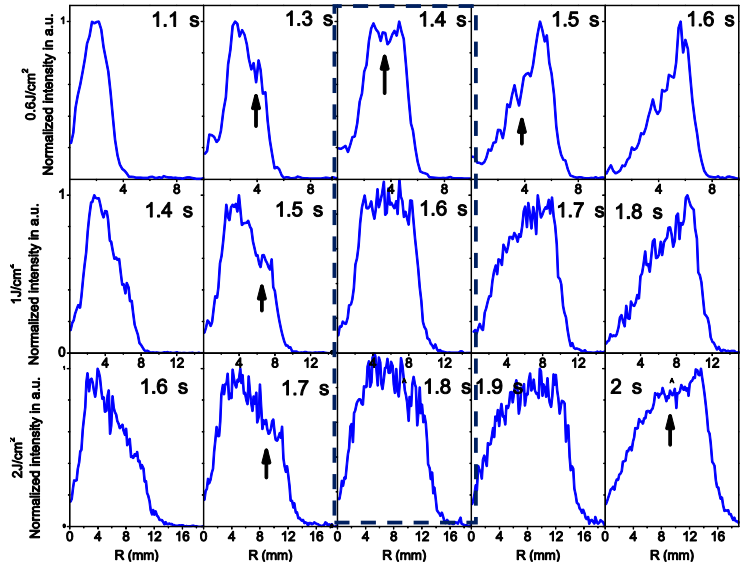


**Figure 5-18:** Normalized intensity profiles of the plume emission along the plume middle for different laser fluencies $F_L$ and delay times **τ**. The arrows mark weak indications of plume splitting. With $p_{O2}$: 0.1mbar, $T_S$: 800°C.

The arrows indicate weak signs of plume splitting, however, such minute variations can hardly be regarded as a separation of plume species or a plume splitting. Figure 5-18 helps to illustrate the expansion state of the plume. A phenomenological observation in Figure 5-18 can be made by comparing the intensity profiles of the 3 plumes at 1.4µs, 1.6µs and 1.8µs. All 3 profiles are almost symmetric which mark the delay times where the plume acceleration is zero, compare with Figure 5-17 (d). The acceleration or the deceleration of the plume are accompanied by a compression of the plume back or plume front respectively which is represented by a sharp decline in the emission intensity.

The compression of the plume front causes scattering of plume particles [55] due to the increased density of species in this region. In any scattering event, lighter particles are scattered to larger angles resulting in a proliferation of heavier particles in the scattering center. In the actual case of STO the atomic weight of a Sr-particle is almost twice the atomic weight of a Ti-particle and ~2.7 times heavier than an oxygen molecule. Therefore Sr-species should accumulate in the plume center during the shock-wave like expansion while lighter Ti-species are scattered and ousted of the plume leading to a continuous loss of Ti-species. The loss of Ti-species is more pronounced the longer the plume propagates and the stronger the plume is compressed i.e. the higher the background pressure is. Applying these considerations to the measured plume dynamics in Figure 5-17 (b) and to the PALS findings in Figure 5-3 and to the results of Ohnishi et al. [1] the trend of the increasing Sr content with decreasing laser fluence could be explained.

Ti species can be scattered and the plume becomes progressively Sr-rich. This effect would explain the results from Figure 5-9 where the amount of Sr in the plume increases with increasing substrate to target distance. In this case more Ti-species will get lost the longer it takes for the plume to reach the substrate. The loss of Ti species during plume propagation is a function of the initial plume mass $M_p$, the background gas density and the plume velocity.
However, the scattering of Ti-species cannot explain the excess of Ti for some of the STO films. Only an incongruent ablation process with a preferential ablation of Ti species with increasing laser fluence could explain the increasing amount of Ti in the STO film.

#### *5.2.1.2 XPS analysis and target ablation characteristics*

For the investigation of incongruent ablation, XPS spectra were taken for the ablation spots on the STO target respectively and compared to the resulting film stoichiometry as shown below.

| $F_L$ (J/cm$^2$) | Sr/Ti ratio | |
|---|---|---|
| | STO thin film | Target |
| **0.8** | 1.15 ± 0.05 | 1 ± 0.05 |
| **1.1** | 1 ± 0.05 | 1.05 ± 0.05 |
| **1.7** | 0.8 ± 0.05 | 1.13 ± 0.05 |

**Table 5-3:** XPS analysis of STO films and respective ablation spots on the STO target. With $p_{O2}$: 0.1mbar, $T_S$: 800°C $D_{TS}$: 40mm. *Measurements performed by A. Köhl*

The XPS results for the STO films exhibit the expected Sr/Ti ratios. The XPS results for the ablation spot show an increasing Sr/Ti ratio with increasing laser fluence. The same trend for the ablation spot stoichiometry was reported by [65]. This indicates an incongruent ablation where the STO surface becomes Ti-deficient with increasing laser energy.

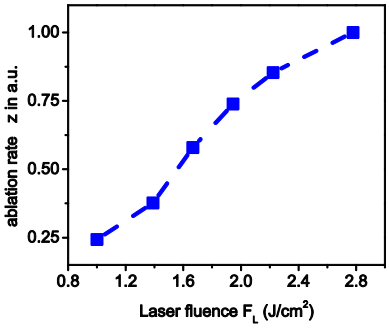


**Figure 5-19:** ablation rates $\Delta z_u$ of STO for different laser fluencies.

The ablation rate $\Delta z(F_L)$ shows a linear trend where an Arrhenius dependence for $F_L < 0.8 J/cm^2$ and a logarithmic dependence for $F_L > 3 J/cm^2$ can be assumed. The ablation of STO therefore indicates a thermal ablation characteristic.
The incongruent ablation detected by XPS cannot be explained by the measured ablation rate per se. The STO system is a peritectic system where the slightest deviation in stoichiometry will

result in an incongruent melting of the STO target. The phase diagram for STO exemplifies that a non-stoichiometry in either direction reduces the melting temperature $T_m$. When the STO stoichiometry on the ablation spot gradually changes in the surface region with laser energy, $T_m$ decreases and causes $\Delta z$ to increase. Therefore the incongruent ablation might be a self-sustaining process. The more material is being melted the more a non-stoichiometry change is facilitated.

### *5.2.1.3 Plume spectroscopy analysis*

To assess the chemical composition of the plume for different laser fluencies, optical emission spectroscopy was carried out as described before in chapter 4.1.3. The spectra were taken in the early stage of the plume propagation at $\tau$ = 1.6µs.

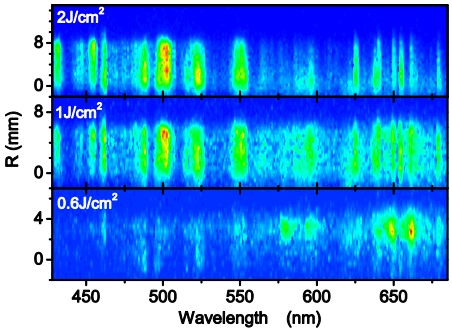


**Figure 5-20:** optical emission spectra of plumes created at different laser fluencies $F_L$ (0.6, 1 and 2J/cm²) at $\tau$ = 1.6µs. With $p_{O2}$: 0.1mbar, $T_S$: 800°C.

Each optical emission spectrum above is normalized to its own intensity maximum. Qualitatively the spectra in Figure 5-20 reveal that the emission of Ti increases with laser energy. Considering the XPS results for the STO ablation spot, the plume emission spectra support the theory of a Ti-rich ablation with increasing laser fluence leaving behind a Sr-rich ablation spot.

### *5.2.1.4 Scattering of plume species*

To complete the plume analysis the scattering process of plume species was resolved. By monitoring the relative intensities of the emission lines for different delay times $\tau$ the temporal variation of the species concentration can be qualitatively detected. Therefore, timely resolved optical emission spectra of a STO plume in an inert background gas was measured. By choosing an inert gas like Ar, falsification of the optical signal due to chemical reactions of plume species with oxygen can be excluded and the gas primarily affects the kinetics and scattering effects of species. The plume was measured for a laser fluence of $F_L$ = 1.5J/cm² and an Argon background pressure of $p_{Ar}$ = 0.2mbar. The relative Sr/Ti emission signal versus the propagation distance $R$ is plotted in Figure 5-21.

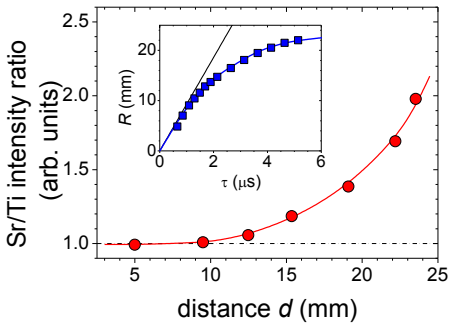


**Figure 5-21:** Sr/Ti emission intensity ratio as a function of the distance d from the STO target surface in Argon background gas. The inset shows an R-τ of the STO plume front. With $D_{TS}$: ∞, $T_S$: 25°C, $p_{Ar}$: 0.2mbar, $F_L$: 1.5J/cm²

The plot in Figure 5-21 implies that when the STO plume is braked down by the background gas and transforms from a free expansion into the shock-wave expansions at R ~ 10mm the Sr/Ti intensity ratio increases indicating a loss of Ti-species. These findings strongly support the theory devised before that Sr-species proliferate in the plume center due to preferential scattering of Ti species to larger angles. In Figure 5-22 the loss of Ti species can be observed by the decline of the emission intensity for 375nm < λ < 500nm where the radiation originates predominantly from T-species.

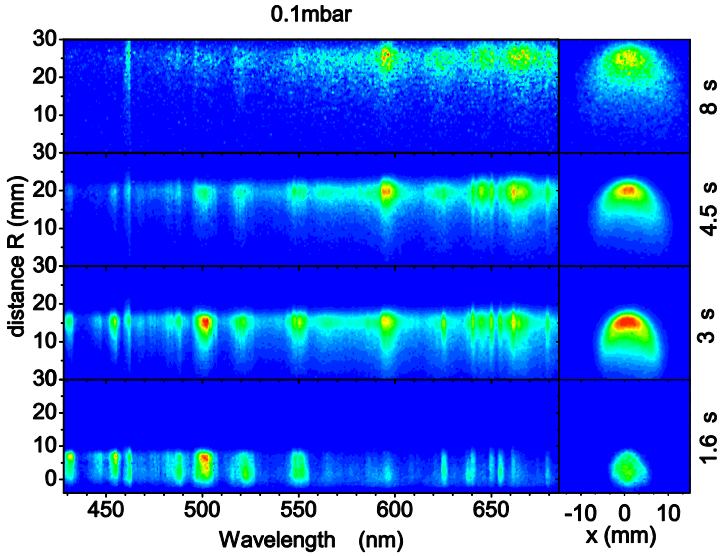


**Figure 5-22:** Optical spectroscopy images of a propagating STO plume with $p_{O2}$ = 0.1mbar for different delay times τ

As can be seen above, the intensity of the Ti species (420nm – 460nm) drops during the plume propagation and indicates the loss of Ti-species due to scattering events. The confirmation of the augmented scattering of Ti-species from the plume in combination with the verification of the preferential ablation of Ti-species with increasing laser energy completes the general model of

the origin of the stoichiometric variation of STO thin films with laser fluence and their incorporation of cation vacancies at $p_{O2}$ ~ 0.1mbar, $T_S$ ~ 800ºC and $D_{TS}$ 35 – 55mm.

### 5.2.1.5 Oxidation state of plume species

The spectroscopic analysis of the propagating plume as shown in Figure 5-22 also depict an enlargement of the emission lines which eventually merge into so-called emission bands. These bands are the result of the oxidation the plume species during their propagation to the substrate. The oxidation state of the arriving species on the substrate is in the following investigated as a function of the laser fluence in oxidizing atmosphere with $p_{O2}$ = 0.1mbar. The results are shown below.

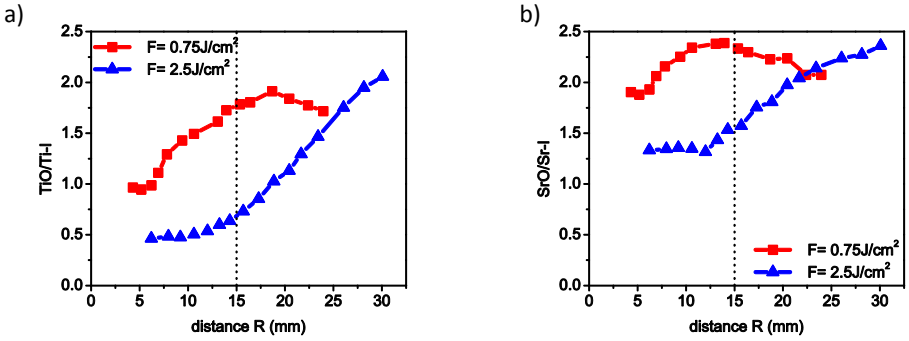


**Figure 5-23: a)** Variation of the intensity ratio of TiO/Ti-I species versus travel distance R and different laser fluencies, **b)** Variation of the intensity ratio of SrO/Sr-I species versus travel distance R and different laser fluencies.

The plots in Figure 5-23 show the intensity ratio of SrO- and TiO-species and Sr-I and Ti-I species respectively. The ratios increase with distance $\boldsymbol{R}$ traveled, which demonstrate that the species oxidize during the time of flight. The decrease of the intensity for the plume species ablated with $F_L$ = 0.75J/cm$^2$ is due to decrease of the optical intensity of the emission. The plots illustrate that the species are initially already more oxidized for a low laser fluence which indicates that the initial oxidation state of emerging species decreases with increasing laser fluence.

The plots also demonstrate nicely that the oxidation of the plume species start at $\boldsymbol{R_T}$ when the plume converts from the free expansion to the shock-wave like expansion where the plume starts to interact with the background gas, compare with Figure 5-17 (c), which is ~7.5mm for the plume ablated with 0.75J/cm$^2$ and ~12.5mm the plume with 2.5J/cm$^2$. Also, the plume species oxidize more rapidly for a low laser fluence, which can be observed by the steeper slope of the TiO/Ti-I and SrO/Sr-I ratio after the onset of the oxidation. This indicates that the oxidation state of the plume species is a function of the laser fluence. Therefore, the SrO/Sr-I and TiO/Ti-I ratio is studied for various laser fluencies at R = 15mm.

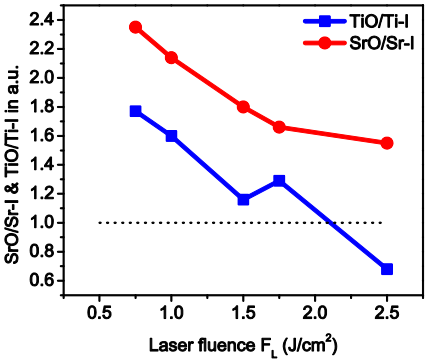


**Figure 5-24:** Oxidation ratio of SrO/Sr-I and TiO/Ti-I as a function of the laser fluence at a distance R = 15mm from the target.

The oxidation ratio of the plume species, plotted in Figure 5-24, decreases systematically with increasing laser fluence. For laser fluencies $F_L > 2J/cm^2$ the TiO/Ti-I ratio is < 1 which could lead to the deposition of more metallic Ti-species than TiO species. This could result in the deposition of Ti rich films with a high amount of oxygen vacancies.

### 5.2.2 $O_2$ background pressure variations

The XRD patterns from Figure 5-10 are shown again below. With the findings from the laser fluence variation above the nascent plume stoichiometry can be assigned to the laser fluence, see Table 5-3.

Nascent plume: Sr/Ti ~ 1 | Nascent plume: Sr/Ti < 1 | Nascent plume: Sr/Ti << 1

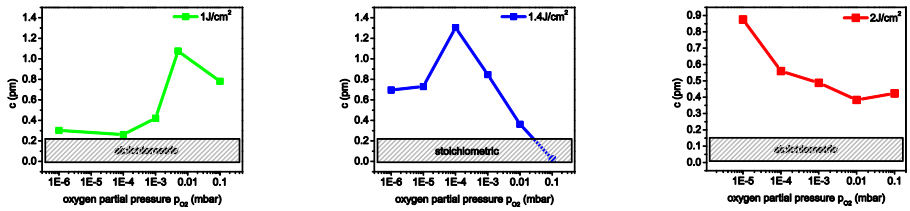


**Figure 5-25:** out-of-plane lattice expansion of STO thin films grown for different $O_2$ background pressures and laser fluencies. **(a)** $F_L$: 1J/cm² **(b)** $F_L$: 1.4J/cm² **(c)** $F_L$: 2J/cm². With $T_S$: 800°C, $f_L$: 5Hz

In Figure 5-25 (a) the nascent plume is stoichiometric with a Sr/Ti ~ 1. Due to preferential scattering of Ti-species as discussed above in chapter 5.2.1 the STO film for $p_{O2}$ = 0.1mbar is Sr-rich with a Sr/Ti ratio > 1 and hence, shows an expanded c-axis lattice parameter. By reducing the background pressure the scattering effects of Ti gradually decrease and the STO film grows to be stoichiometric which materializes in a very small or no c-axis lattice expansion.

When STO films are deposited for $F_L$ = 1.4J/cm$^2$ the emerging plume is Ti-rich i.e. Sr/Ti < 1. At elevated background pressure, the scattering effects of Ti-species can render a stoichiometric STO film. Therefore, by reducing the pressure less Ti-species are scattered yield an increasing Ti-rich film with an expanded out-of-plane lattice parameter.
The obvious drop of Δc for STO films grown at $10^{-5}$ and $10^{-6}$mbar could be explained by a defect chemistry approach. Due to the reducing conditions and the obvious dark coloring of the specimen after growth the system obviously contains a relatively high amount of oxygen vacancies $V_O^{\bullet\bullet}$. The Schottky equilibrium described in chapter 2.2 dictates that due to an artificial increase of $[V_O^{\bullet\bullet}]$ the total amount of $[V_{Sr}^{''}]$ in the system has to be reduced by an equal measure according to the corresponding law of mass action given below.

$$K_S^O \exp\left(-\frac{\Delta H^S}{k_B T}\right) = \left[V_{Sr}^{''}\right]\cdot\left[V_O^{\bullet\bullet}\right] = K_S^*(T) \qquad \textbf{(5.6)}$$

Since the term on the left in the equation above essentially is a constant it becomes apparent that with an increasing concentration of $V_O^{\bullet\bullet}$. The incorporation of strontium vacancies $V_{Sr}^{''}$ is suppressed and the $V_{Sr}^{''}$ / $V_{Ti}^{''''}$ ratio decreases which reduces the lattice expansion.
Moreover, Freedman [31] argues that by the incorporation of oxygen vacancies the Coulomb interaction of cation vacancies are shielded and the lattice expansion therefore decreases.

When the laser fluence is even further increased to $F_L$ = 2J/cm$^2$ the nascent plume becomes even richer in Ti with Sr/Ti << 1. Although Ti-species are lost during the plume propagation in a background pressure there are still enough Ti-species to render a Ti-rich film for $p_{O2}$ = 0.1mbar. By reducing the pressure further, this trend perpetuates and STO films become increasingly Ti-rich.

The qualitative Sr/Ti ratio of the STO film versus background pressure is given in the following graph for different laser energies.

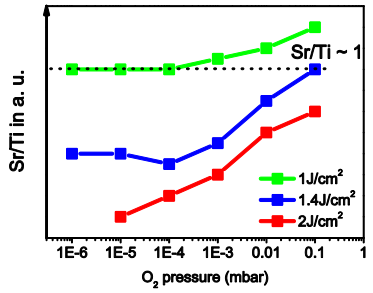


**Figure 5-26:** Qualitative representation of the Sr/Ti ratio of the STO films for different background pressures and laser fluencies. With $T_S$: 800°C, $f_L$: 5Hz

The qualitative Sr/Ti ratios for different laser fluencies and background pressures imply that the stoichiometry of the STO can be adjusted by tuning $\boldsymbol{D_{TS}}$, $\boldsymbol{F_L}$ and $\boldsymbol{p_{O2}}$.

The x-ray diffraction results in Figure 5-25 indicated that with decreasing pressure the nascent plume stoichiometry seems to prevail and the scattering events during the plume propagation towards the substrate decline. As demonstrated in chapter 5.2.1 the scattering events take place during the shock-wave like expansion and the diffusion like flow.

#### *5.2.2.1 Plume dynamics*

To probe for the plume front kinetics and the evolution of the shock-wave expansion the STO plume dynamics were investigated by optical plume analysis for different pressure conditions. Optical spectroscopy analysis will provide an insight into the plume stoichiometry for different pressure and propagation states.

Figure 5-27 (a) displays the 2D plume images of the propagating STO plume for different $O_2$ background pressures at different delay times. The interaction of the plume front with the background gas can be observed by the formation of a spherical shape of the plume front. When the plume propagates through the ambient gas it accumulates gas molecules which compress and decelerate the plume [84]. The plume with an ambient pressure of $10^{-3}$ mbar shows no distinct sign of such an accumulation or deceleration. The plume rather continuous to expand freely and keeps its characteristic shape.

The expansion dynamics and the plume front position vs. delay time are plotted in Figure 5-27 (b). The simulation of the expansion dynamics reveal that the initial velocity $\boldsymbol{u_0}$ and the plume mass $\boldsymbol{M_p}$ remain constant and were determined to be $u_0$ = 13.5km/s and $M_p = 8.2 \cdot 10^{-10}$ kg. The laser fluence $F_L$ = 1.5 J/cm$^2$ was kept constant and the substrate temperature $\boldsymbol{T_S}$ was 800ºC. The ambient pressure only affects how much the plume is compressed due to the buildup of a gas layer and the accumulation of gas molecules which decelerates the plume. The result of the deceleration can be observed in figure (c) where the plume front velocity $\boldsymbol{u_F}$ is plotted vs. the plume front position $\boldsymbol{R_F}$. The solid lines in the plot represent the simulated velocities for the parameters given above. The kinetic energy of the arriving species increases with decreasing pressure. The plume species for $p_{O2}$ = 0.85mbar only reach the substrate via diffusion. Kinetic energies of species at R = 33mm ($\boldsymbol{D_{TS}}$) are given in the following.

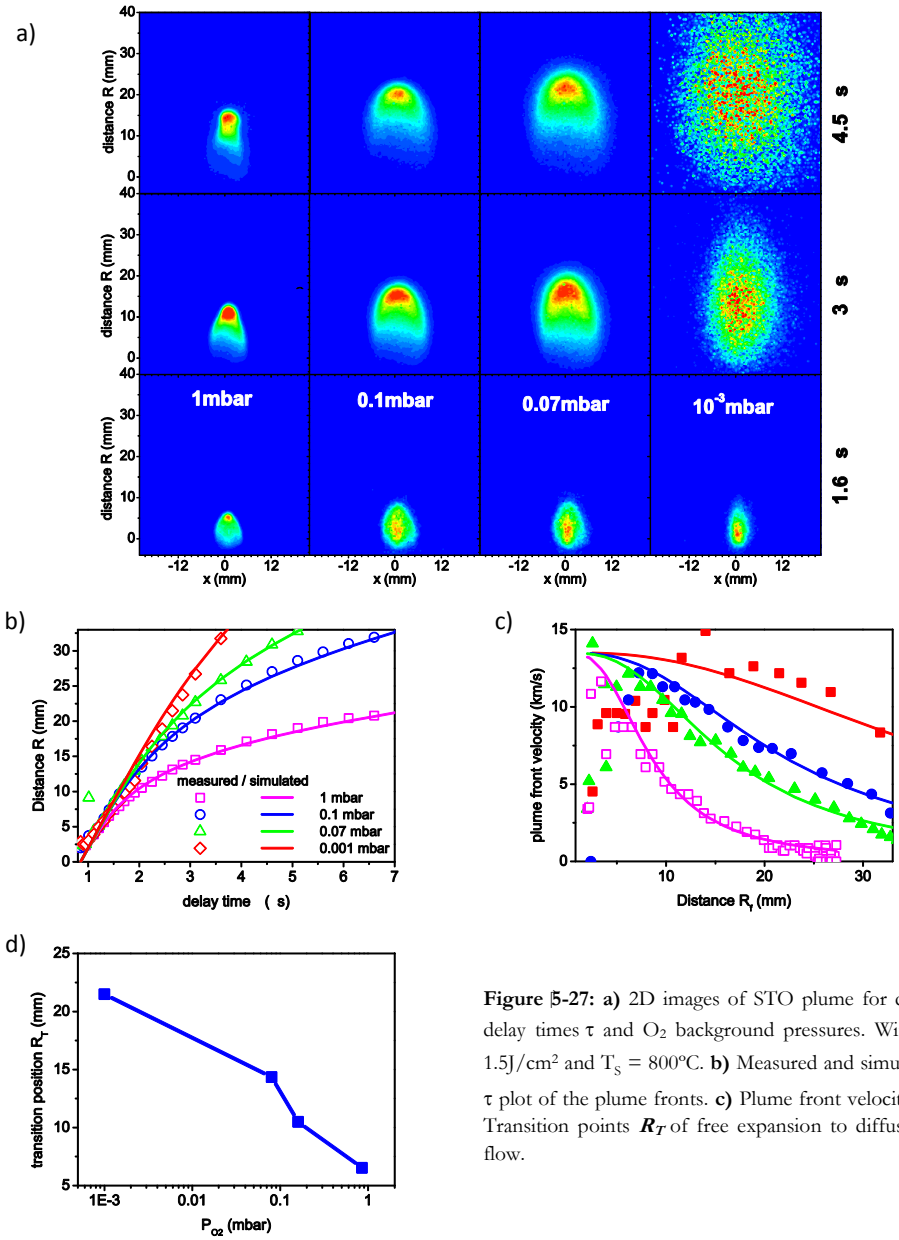


**Figure 5-27: a)** 2D images of STO plume for different delay times τ and $O_2$ background pressures. With $F_L$ = 1.5J/cm² and $T_S$ = 800°C. **b)** Measured and simulated R-τ plot of the plume fronts. **c)** Plume front velocity $u_F$ **d)** Transition points $R_T$ of free expansion to diffusion-like flow.

The transition positions $\boldsymbol{R_T}$ are shown in figure (d) and shift to higher distances with decreasing pressure. With the shift of $\boldsymbol{R_T}$ the onset of scattering events is delayed. Additionally, the probability Π of scattering events is decreased for lower pressures because the scattering scales with pressure. Both effects combined yield the full aspect of the scattering of plume species.
If $\boldsymbol{R_T} > \boldsymbol{D_{TS}}$ the plume transfer occurs without any change of its nascent stoichiometry. Within this narrative the shift of the c-axis as function of the background pressure can be explained by the plume dynamics. For $p_{O2}$ pressures < $10^{-5}$mbar exhibit an increased incorporation of oxygen vacancies which influence the formation of cation vacancies and the lattice expansion due to Coloumb interactions. Therefore plume kinetics cannot be applied within this regime to explain any changes in the cation sublattice of the growing thin film.

| | $E_{kin}$ [eV] | | | | |
|---|---|---|---|---|---|
| | **Sr** | **SrO** | **Ti** | **$TiO_2$** | **Average** |
| **1mbar** | 0.22 | 0.26 | 0.12 | 0.21 | 0.2 |
| **0.1mbar** | 2.2 | 2.6 | 1.2 | 2 | 2 |
| **0.07mbar** | 6.56 | 7.75 | 3.58 | 5.98 | 6 |
| **0.001mbar** | 32.8 | 38.8 | 17.9 | 29.9 | 30 |

**Table 5-4:** Kinetic energies of different plume species at R = 33mm.

#### *5.2.2.2 Plume spectroscopy*

It was established before in chapter 5.2.1 that Ti species are lost during the plume propagation due to scattering events. The emission of different plumes is now plotted at τ = 4.5µs in Figure 5-28 to compare the qualitative intensities of the Ti emission lines. The Ti content of the plume should increase with lower background pressures since less Ti-species will be scattered.

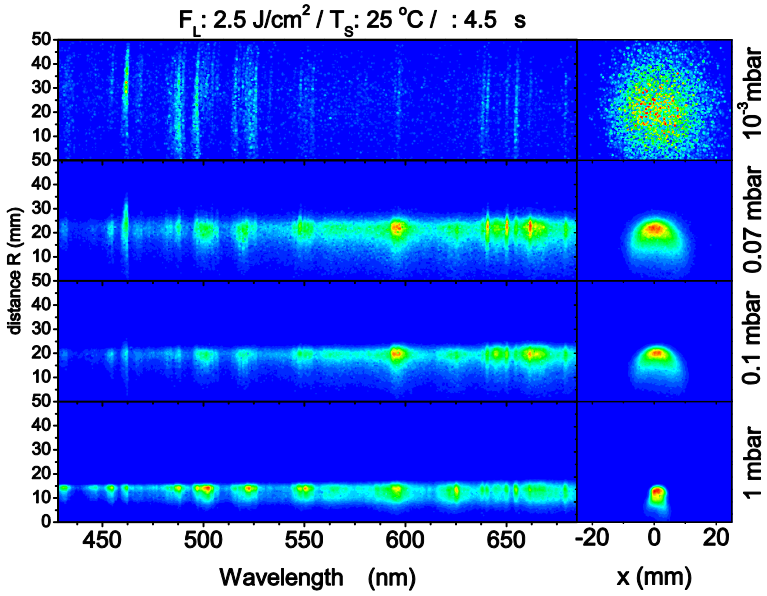


**Figure 5-28:** Optical spectroscopy images of STO plumes in different background pressures.

The images indeed reveal that the emission intensity of Ti-species within the range of 420nm – 460nm increases with decreasing background pressure. The reaction of plume species with oxygen decreases as well which can be seen by the conservation of the emission lines rather than the formation of emission bands due to the oxidation of species. This observation clearly demonstrates that the species have to oxidized after they arrive on the substrate surface. The necessary oxygen is then provided by the substrate which effectively reduces the bulk.

### 5.2.3 Effect of substrate temperature on the stoichiometry of STO thin films

It was shown by Sambri et al. [54] that the substrate temperature has an influence on the plume expansion kinetics which could cause a shift of the plume stoichiometry. The characteristics of the plume kinetics are presented in the following for various substrate temperatures.

The effect of the substrate temperature on the plume dynamics becomes visible in Figure 5-29. The plume front velocity $u_F$ for a plume with elevated $T_S$ is faster than for low $T_S$. Also, the transition from free to shock-wave like expansion takes place at earlier delay times for a low substrate temperature.

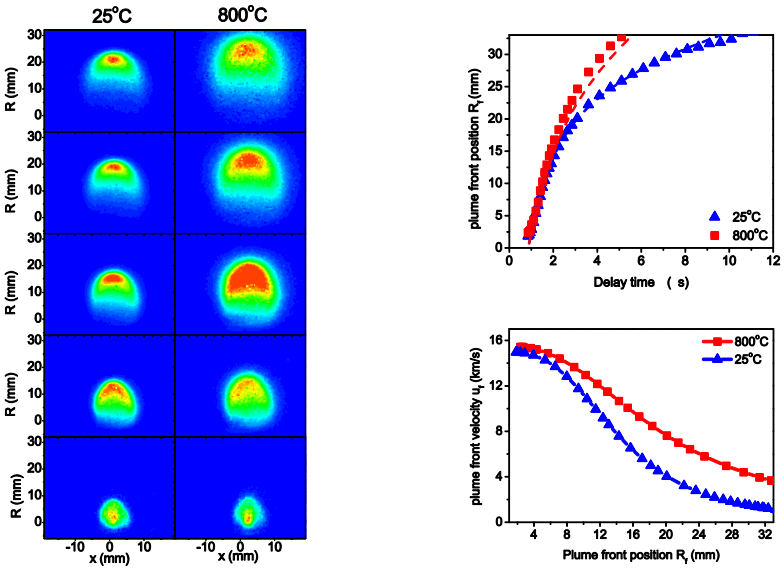


**Figure 5-29: a)** 2D plume images for different substrate temperatures. **b)** Plume front positions $z_f$ for different substrate temperatures. **c)** Plume front velocity. $F_L$: 2.5J/cm², $p_{O2}$: 0.1mbar.

The expanding plume seems less confined for a high substrate temperature and the braking effect by the background gas is obviously more effective for a low substrate temperature. These observations can be explained by the modification of the gas density due to the substrate temperature which was explored and elucidated by Sambri et al. [54].

The density of a gas is inversely proportional to its temperature. The density of the gas $\rho_g$ as a function of the temperature $T$ can be estimated by the ideal gas law as shown below. Where $p$ is the background gas pressure and $R_g$ is the specific gas constant, 260J/kg·K for oxygen.

$$\rho_g(R_f) = \frac{p}{R_g T(R_f)} \quad \text{with} \quad T(R_f) = T_T + \frac{T_S - T_T}{D_{TS}} \cdot R_f \tag{5.7}$$

The substrate temperature loses temperature to the gas by conduction and thereby heats up the background gas. The temperature gradient from the substrate $T_S$ to the target is supposed to be linear where the target ideally remains at room temperature $T_T$. The gradient depends on the target substrate distance $D_{TS}$. It is important to note that no convection of the gas is considered due to the low pressures during the PLD processes.

By substituting $\rho_g(z)$ for $\rho_g$ in equation (4.10) the velocity and the R – τ characteristic for the plume with $T_S$ = 800°C can be fitted correctly (dashed curve in Figure 5-29) to the actual measured values.

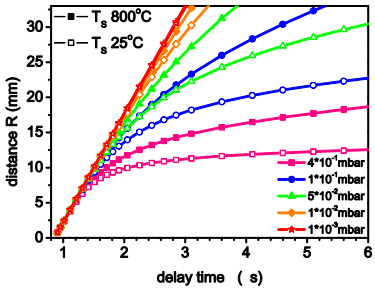


**Figure 5-30:** Simulated R – τ plots for PLD plume with $M_p$ = 8*10$^{-10}$kg & $u_0$ = 15km/s for different background pressures $p_{O2}$ and Substrate temperatures $T_S$.

The influence of the substrate temperature on the plume dynamics is effective for background pressures down to $p_{O2} > 10^{-3}$mbar as shown in Figure 5-30.

### 5.2.3.1 *Plume dynamics:*

Taking into account the dependence of $\rho_g$ on the substrate temperature $T_S$ the plume dynamics for the plumes and conditions in Figure 5-15 can be simulated. A plume with $M_p$ = 8·10$^{-10}$ kg and $u_0$ = 13.5 km/s was considered. The R – τ plots in Figure 5-31 (a) show that the plume dynamics are only slightly influenced by the variation of the temperature $T_S$ from 650°C – 1125 °C. Also the scattering probability $\Pi_S$ only changes slightly. Therefore the plume stoichiometry varies only slightly by varying $T_S$ from 650 – 1125 °C at 0.1 mbar. The influence of the substrate temperature would be more effective for higher background pressures where the gas density shows a larger deviation.

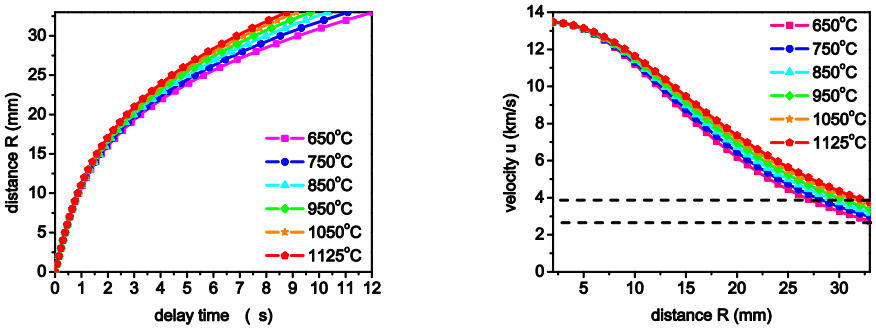


**Figure 5-31: a)** Simulated R – τ plot for plumes for different plume substrate temperatures $T_S$. **b)** Simulated R – u plot for different $T_S$. With $M_p$ = 8·10$^{-10}$mbar, $u_0$ = 13.5km/s, $p_{O2}$ = 0.1mbar, $F_L$ = 1.3J/cm$^2$, $D_{TS}$ = 40mm.

## 5.3 Discussion and Conclusions

It was shown that by varying the PLD processes parameters $F_L$, $p_{O2}$, $T_S$ and the target to substrate distance $D_{TS}$ the stoichiometry and defect accommodation of the STO thin film can be varied. The nascent plume stoichiometry depends on the laser fluence $\boldsymbol{F_L}$. For low laser fluencies a stoichiometric plume with Sr/Ti ~ 1 is created. With increasing fluence the plume stoichiometry becomes Ti-rich due to an incongruent laser ablation for increasing laser fluence as shown in Table 5-1. After the ablation process is finished and the plume is released into the background gas, and the plume kinetics and the plume stoichiometry is influenced by the background gas with $\boldsymbol{p_{O2}}$. The interaction of the plume species with the gas molecules leads to the scattering of lighter Ti-species whereas Ti-species are scattered to bigger angles and the plume core becomes increasingly Sr-rich. This can yield a Sr-rich STO film. By increasing the laser fluence the loss of Ti-species can be compensated due to the preferential ablation of Ti and a stoichiometric film can be generated. When the laser energy is increased even further the plume becomes over compensated with Ti-species and renders a Ti-rich STO film.

A non-stoichiometric STO films shows a characteristic expansion of the out-of-plane lattice parameter and seems to be a function of the $V_{Sr}''/ V_{Ti}''''$ ratio in the STO film. For a stoichiometric STO film the $V_{Sr}''/ V_{Ti}''''$ ratio ~ 1. PALS analysis confirms the existence of both cation vacany types $V_{Sr}''$ and $V_{Ti}''''$ in the STO film, proving that the formation of $V_{Ti}''''$ in the STO film is energetically feasible. The ratio of $V_{Sr}''/ V_{Ti}''''$ depends on the prevalent non-stoichiometry in the STO film. A Ti-rich STO film shows an increasing $V_{Sr}''/ V_{Ti}''''$ ratio with an increasing Ti-content. For a Sr-rich STO film the $V_{Sr}''/ V_{Ti}''''$ ratio increases again. This can be attributed to the formation of Ruddlesden-Popper phases that cause the formation of $V_{Sr}''$ and the elimination of $V_{Ti}''''$. Because planar faults introduce grain boundaries and anti-phase boundaries the formation of nano-voids with up to 14 vacancies can be observed.

The reason for the reduction of the lattice expansion for an equal cation vacancy ratio might have mechanical and electro static reasons. The lattice expands due to the formation of cation vacancies mainly because of their Coloumb interaction. An additional cation vacancy on a different lattice site might counteract this interaction.

When the background pressure $\boldsymbol{p_{O2}}$ is decreased the scattering events are delayed and are also less pronounced. The plume velocity increases with decreasing pressure.

With the decrease of the scattering events the plume progressively maintains its nascent plume stoichiometry and the STO film resembles this stoichiometry. For $p_{O2} \leq 10^{-4}$mbar the incorporation of oxygen vacancies into the thin film increases intensely with $[V_O^{\bullet\bullet}] >> [A']$ which resembles the intrinsic n-type region, as shown in Figure 2-2 in chapter 2.2.2. With an activated Schottky equilibrium this could result in the suppression of cation vacancies (predominantly $V_{Sr}''$).

Below $10^{-4}$mbar the particles keep their initial velocity from the ablation and the kinetic energy of species near the substrate surface can reach up to 35eV. This energy is sufficient to break up many-fold bonds on the surface of the growing film which results in the destruction of small

growth islands and the smoothening of the surface by the suppression of 3D clusters. Sputtering of the surface per se is not likely within this energy regime.
With decreasing pressure the oxidation of the arriving species is less pronounced and the species therefore use oxygen from the substrate to form an oxide phase. The supply of oxygen by the substrate works for temperatures as low as 370ºC. Because of the thermal activation and the kinetic energy of the arriving cations, oxygen ions are easily ejected from the surface. Due to this lack of oxygen in the surface region of the growing film exhibits a concentration gradient of oxygen and develops a space charge layer. Within this space charge layer the cation vacancies realign and also exhibit a concentration profile.

The substrate temperature $\boldsymbol{T_S}$ affects the defect accommodation by influencing the growth kinetics but has basically no effect on the stoichiometry of the STO thin film. If a non-stoichiometric plume reaches the substrate surface the cation (vacancy) ratio cannot be changed by the substrate temperature. Only the overall concentration of the defects can be reduced by enhancing the diffusion kinetics with increasing $\boldsymbol{T_S}$. The intensity of the XRD-film peak is a measure of the defect concentration in the system and drops for elevated substrate temperatures. Moreover, the substrate temperature influences the gas density and thereby impacts the plume dynamics. However, for common PLD process pressures $p_{O2} \leq 0.2$mbar the influence on the dynamics and the scattering of species is negligible.

# 6 Defect formation & accommodation in Fe doped $SrTiO_3$ thin films

Doping $SrTiO_3$ with Fe (Fe:STO) serves many purposes. Particularly with regard to resistive switching, Fe:STO with low Fe concentrations 0.5% ≤ Fe ≤ 2% is a preferred system as it is reported to facilitate and stabilize the resistive switching effect [85] and can also be used as a tracer for subsequent X-ray spectroscopy techniques [86]. By determining the valence state of iron one can conclude on the abundance of oxygen vacancies [$V_O^{\cdot\cdot}$] in the system. As described above, the movement of oxygen vacancies is essential for the resistive switching effect.
Also, a STO thin film can contain "natural" impurities such as Ca, K or Cu for example which introduce an acceptor-type doping. Since even minute concentrations of impurities can influence the physical properties of the STO thin film and can vary statistically it is only straight forward to dope the STO system deliberately with an acceptor that would overshadow the effect of the impurities.
When Fe is incorporated into the STO system it substitutes the Ti host atom. Iron when oxidized is predominantly found to be in a redox state of $Fe^{3+}$ or $Fe^{2+}$. Since the Ti host atom is in a $Ti^{4+}$ redox state the $Fe^{3+/4+}$ transition might introduce additional defect chemical reactions within the Fe doped STO system.

## 6.1 XRD and PLD process analysis

Fe doped STO films were deposited via PLD for several Fe doping concentrations and different laser fluencies. The detailed PLD process settings are given in detail with the figures below. The X-ray diffraction was performed the same way as already discussed previously.
The deposition rate was measured via RHEED where the number of pulses [#] per unit cell was determined. The ablation rate was gauged via profilometry. First, 100 UV-laser pulses were directed onto a single spot on the target creating a square crater structure. By utilizing a DEKTAK profiler the average depth of the crater was determined which was used as measure of the ablation rate. This was done for several STO targets with different Fe doping concentrations.

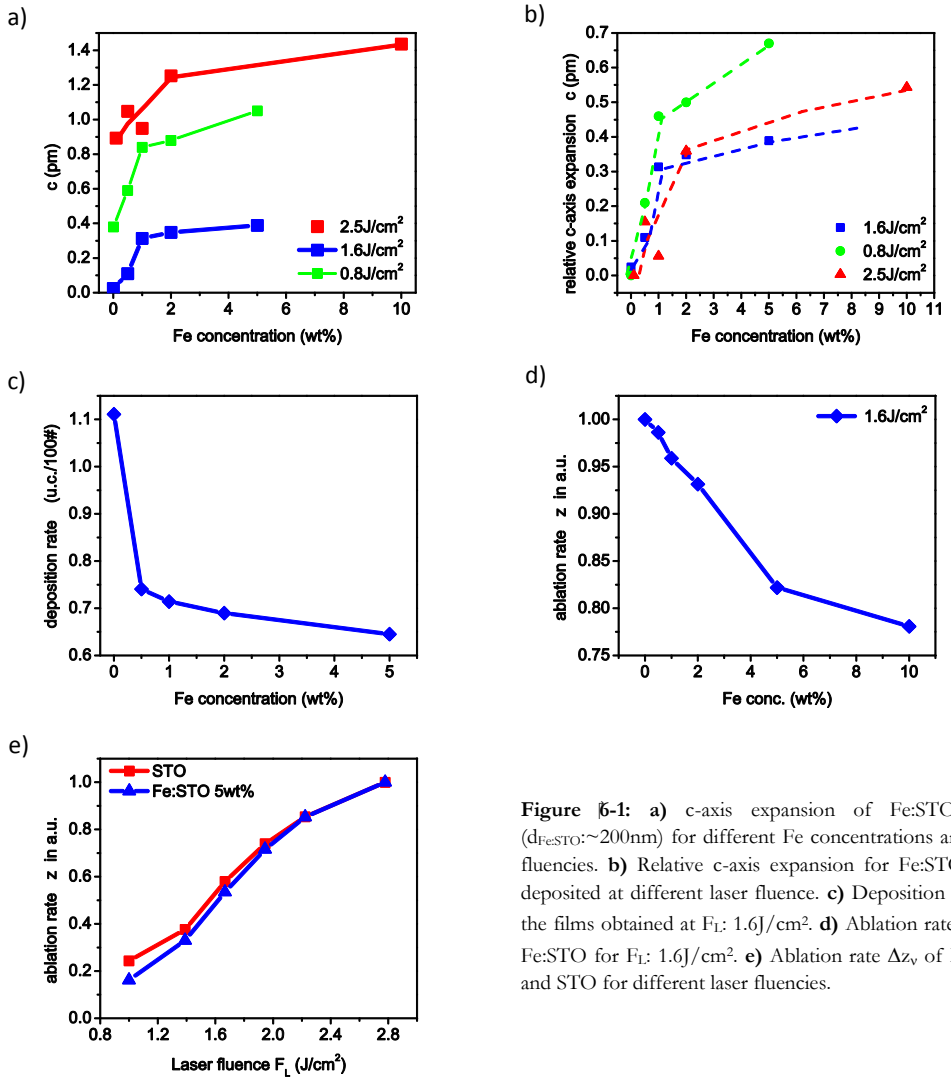


**Figure 6-1: a)** c-axis expansion of Fe:STO films ($d_{Fe:STO}$:~200nm) for different Fe concentrations and laser fluencies. **b)** Relative c-axis expansion for Fe:STO films deposited at different laser fluence. **c)** Deposition rate for the films obtained at $F_L$: 1.6J/cm². **d)** Ablation rate $\Delta z_v$ of Fe:STO for $F_L$: 1.6J/cm². **e)** Ablation rate $\Delta z_v$ of Fe:STO and STO for different laser fluencies.

The c-axis expansion of the Fe doped STO films shown in Figure 6-1 (a) systematically increases with the Fe content. First the lattice expands steeply with the Fe content and beyond 2wt% Fe the c-axis expansion levels off and eventually saturates. This behavior seems to be independent of the laser fluence since the sequence at 2.5J/cm² shows the same trend as the sequence for 1.6J/cm² and 0.8J/cm², see Figure 6-1 (b).

It was established before, that the expansion of the c-axis for a STO thin film system with 0wt% Fe is due to the ratio of the cation vacancies. By doping an existent system with Fe the c-axis expands further, as can be seen by figure a & b. The proportion of this c-axis expansion due to

Fe seems to be independent of a preexisting lattice expansion (due to cation defects in the STO film) as can be seen by Figure 6-1 (b). Therefore, the lattice expansion due to Fe incorporation could be treated independently of preexisting defect conditions.
By monitoring the deposition process e.g. via RHEED the effect of Fe on the deposition rate $\kappa$ can be noticed and is shown in Figure 6-1 (c). The deposition rate decreases with the iron content (in the target) systematically and saturates for higher Fe concentrations > 10% eventually. The reason for this decrease of $\kappa$ can be found by determining the ablation rate $\Delta z_v$ which is shown in Figure 6-1 (d). Obviously the ablation rate decreases with the Fe content in the target. By comparing the decrease of $\Delta z_v$ due to the Fe content with the decrease of $\Delta z_v$ due to laser fluence varation the effect of the laser fluence outweighs the doping effect by Fe.

Nevertheless, the systematic shift of the deposition and ablation rate with the Fe concentration both hint towards a modification of the laser ablation characteristics by Fe doping. As described above in equation (4.1) the ablation rate $\Delta z_v$ is a function of the threshold fluence $F_{th}$. Combining both expressions yields the equation below.

$$\Delta z_v \approx \frac{AF_L - \rho c T_m L_{th}}{\rho L_v} \quad \text{with} \quad L_{th} \sim (2D\tau_P)^{1/2} \quad \text{and} \quad D = k/\rho c \qquad (6.1)$$

For the Fe sequence the parameters in equation (6.1) are almost all subject to change with Fe doping. It is assumed that the thermal properties of the STO target change the most with Fe doping concentration. It could well be that the thermal conductance $k$ increases with the Fe concentration. When $k$ increases the thermal diffusion coefficient $D$ increases as well and with it the heat penetration depth $L_{th}$. When the heat penetration depth is increased the applied laser energy by $A \cdot F_L$ is dissipated. Hence, less material is ablated.
Although the absorbance $A$ of Fe doped STO increases in the visible region (darkening of STO with Fe doping) the absorbance in the UV region probably decreases according to observations of Zhou et al. [87]. The density $\rho$ of STO only changes minutely due to the Fe doping. The latent heat per unit mass $L_v$ might also be just minutely affected by the Fe doping.
As it is shown below in chapter 6.1.1, a metallic Fe-phase forms upon laser irradiation in the ablation spot. However, the shift of the c-axis lattice expansion with Fe concentration is very big compared to the changes in deposition and ablation rate.

### 6.1.1 XPS analysis of the films and the ablation spots on the target

By XPS analysis the chemical composition on the surface can be determined. For the analysis of the ablation spots Fe:STO targets with different Fe-concentrations were ablated with a fluence of ~1.4J/cm$^2$ and 500 laser pulses. The ablation spot was 0.018cm$^2$.

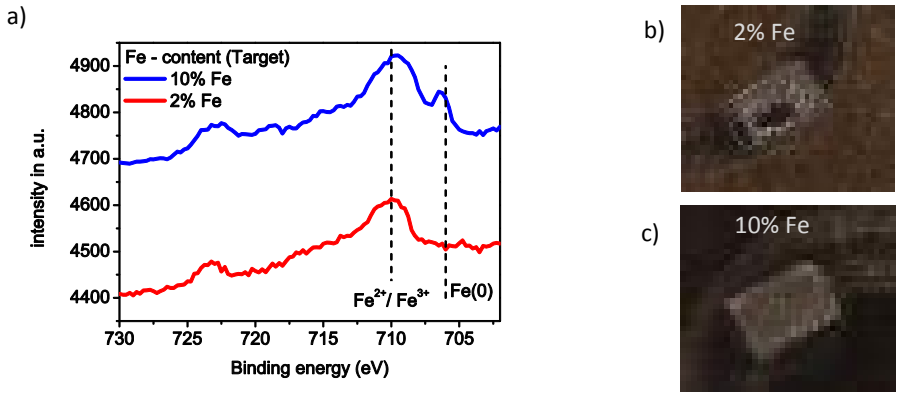


**Figure 6-2: a)** XPS signals within the ablation spot of a 2% and a 10% Fe doped STO target. $F_L$ = 1.4J/cm², #500, $F_L$ = 5Hz. **b) & c)** Photographs of the ablation spots on the Fe:STO target after laser irradiation.

The XPS analysis in the ablation spot of the Fe:STO targets reveal a metallic Fe(0) peak (~706eV) that increases with the Fe content in the target, shown here for the 2% and 10% target in Figure 6-2. The largest contribution stems from $Fe^{2+}$ (FeO) in the ablation spot (~710eV). The formation of a metallic Fe phase can occur during the ablation process where the Fe:STO melts before it is transferred to the gas & plasma phase. A separation of the Fe from the STO is likely since the solubility of Fe in STO is known to be very limited. The ablation process of metallic Fe exhibits different characteristics than Fe:STO and therefore influences the overall ablation characteristics of Fe:STO as presented above in chapter 6.1.

The Sr/Ti ratio in the ablation spot after 500 pulses and 1.4J/cm² were measured for different Fe doping concentrations and are presented in the table below.

| Fe:STO | 0% Fe | 0.5% Fe | 2% Fe | 10% Fe |
|---|---|---|---|---|
| Sr/Ti ratio | 1.16 | 1.2 | 1.13 | 1.2 |

**Table 6-1:** Sr/Ti ratio within the ablation spot of Fe:STO targets and different Fe-concentrations after 500 pulses with $F_L$ = 1.4J/cm².

The Sr/Ti ratio doesn't change or show a clear trend with Fe content as it was observed for example in the case of the laser fluence variation in chapter 5.1.1. Therefore one can relegate the effect of Fe doping to affect the plume stoichiometry.
However, the Sr/Ti ratio resembles the ratio of a Ti-rich ablation, see chapter 5.1.1. Therefore a Ti-rich ablation is assumed which yields strontium vacancies in the STO system.

### 6.1.2 Positron Analysis

As described previously the lattice expansion of a STO thin film can be correlated with defects/vacancies in film. To determine what kind of defects are present in the films they were investigated by PALS and positron Doppler-broadening. PALS results for a Fe-sequence deposited at 1.6J/cm² are presented. Doppler-broadening spectra were recorded using a $^{22}Na$

source. Two sequences were prepared for the Doppler-broadening analysis with the same PLD process settings.

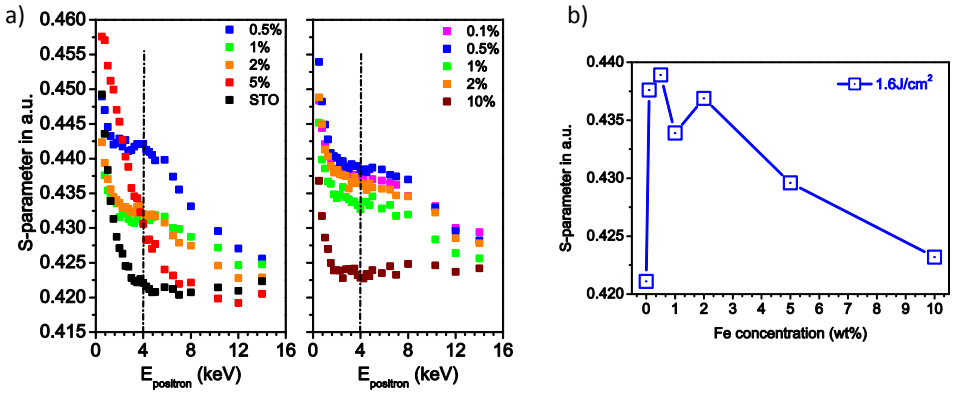


**Figure 6-3: (a)** S-paramter for 2 different sequences of Fe doped STO. **(b)** Average S-Value for different concentration of Fe in STO system

The S-parameter values from the Doppler-broadening of the positron annihilation for the Fe sequence are shown in Figure 6-3 (a) and exhibit a characteristic implantation profile (plateau) describing a fairly uniform point defect distribution within the thin film. The positrons trap into the film for a typical kinetic energy ranging from 2.5keV to 5.5keV.

The average S-parameter value determined at a kinetic energy of 4keV is plotted in Figure 6-3 (b) for different Fe concentrations. Initially the S-parameter value increases sharply for Fe concentrations < 2%. Then the S-parameter value slowly decreases with increasing doping concentrations > 2%.

Since the S-parameter value scales with the defect concentration or the trapping rate in a system this behavior could either imply that the overall defect concentration in the film decreases with Fe doping or that the electronic structure/electron momentum of the valence electrons changes with Fe concentration. The S-value doesn't reveal however, if the concentration of one type of defect is changing or if the defect type is changing. In Table 4-1 the lifetimes of different types of vacancies are listed.

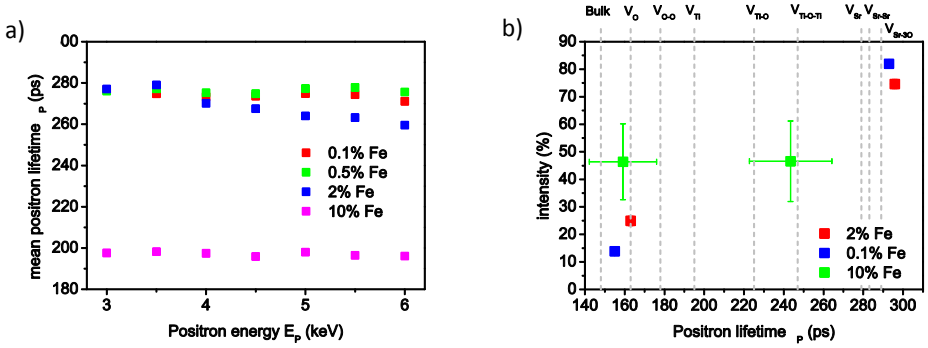


**Figure 6-4: a)** Mean positron lifetimes for different Fe concentrations in the STO thin film at positron energies 2.5keV – 6keV. **b)** Deconvolved mean positron lifetimes for the data shown in (a). The statics reveal that different vacancy types are in the thin film with different intensities/concentrations. For Fe:STO films with 10% Fe the type of vacancy changes as well as the relative concentration of the vacancies.

In order to further elucidate the defect composition in the Fe:STO films for different Fe concentrations the obtained PALS data were deconvolved to retrieve the intensity of the detected lifetime components in the films.

The mean positron lifetimes are plotted in Figure 6-4 (a). All films with a Fe concentration < 2% Fe show roughly the same mean positron lifetime (~277ps) which approximately resembles the typical lifetime for a strontium vacancy $V_{Sr}''$.

To retrieve the lifetime components from the mean positron lifetimes the data set is deconvoluted assuming two different lifetime components and presented in Figure 6-4 (b). The statistics show that more than 75% of the lifetime signal can be attributed to a lifetime component with ~290ps meaning that the film contains strontium vacancies $V_{Sr}''$ coupled to other strontium vacancies or oxygen vacancies forming more complex vacancies. Additionally the film also shows characteristic lifetimes of isolated vacancies at ~160ps which is ~5-10ps longer than for bulk positron lifetime for $SrTiO_3$ and is consistent with the value calculated by DFT for the oxygen mono-vacancy. This suggests either that a proportion of oxygen vacancies have a local charge less than $2^+$, or that there is an unidentified defect with an effective open volume size comparable to an oxygen vacancy; maybe associated with boundaries or extended defects.

With the quadruple strontium vacancies where $V_{Sr}''$ is combined with 3 $V_O^{\bullet\bullet}$ the Fe doped STO films for Fe < 2% seem to be in a reduced state and Ti-rich. Titanium vacancies seem not to be within the film for Fe concentrations ≤ 2%.

The results for the 10% Fe doped STO film are noticeable different; the mean lifetime is significantly smaller. The two lifetime deconvolution gives two components with comparable intensities, the shortest again at ~160ps and a longer lifetime component at ~250ps. The latter is less than the $V_{Sr}''$-lifetime value and may result from trapping at $V_{Ti}''''$-n$V_O^{\bullet\bullet}$ defects, or may result from the weighted average of two unresolved lifetime components. The technique is limited in its ability to deconvolve two closely separated components. There is certainly a suppression in trapping to $V_{Sr}''$ related defects, either due to a reduction in concentration, or due to an increase

in the concentration of vacancy defects with lifetime values less than 290ps ($V_{Sr}''$), or a combination of both.

The origin of the apparent concentration increase of the oxygen vacancies with increasing Fe concentration can be explained by the ablation of metallic Fe from the target. As it was observed before for the pressure sequence, metallic components can use the substrate a source for oxygen. This would result in the formation of oxygen vacancies in the system.

By applying the Schottky equilibrium where the concentration of strontium vacancies must decrease when the concentration of oxygen vacancies increases, the decline of [$V_{Sr}''$] can be explained by the incorporation of oxygen vacancies.

The intensification of $V_{Ti}''''$ with Fe concentration might be a consequence of the formation of a second phase. Since the solubility of Fe in STO is limited the creation of a second Fe-rich phase is plausible. Just like in the case of a Ruddlesden-Popper like phase where a Sr-rich phase is created and $V_{Sr}''$ are formed in this process, the same could happen when a Fe-rich phase is formed. Since Fe occupies Ti-sites the formation of a Fe-rich phase could yield $V_{Ti}''''$.

Since it was argued above that the defects due to Fe incorporation is simply added to the defect structure in the film a fluence sequence was performed for a 2% Fe doped system and investigated by PALS. The fluencies chosen were 1.3J/cm$^2$ (Sr-rich) , 1.6J/cm$^2$ (~stoichiometric) and 2J/cm$^2$ (Ti-rich).

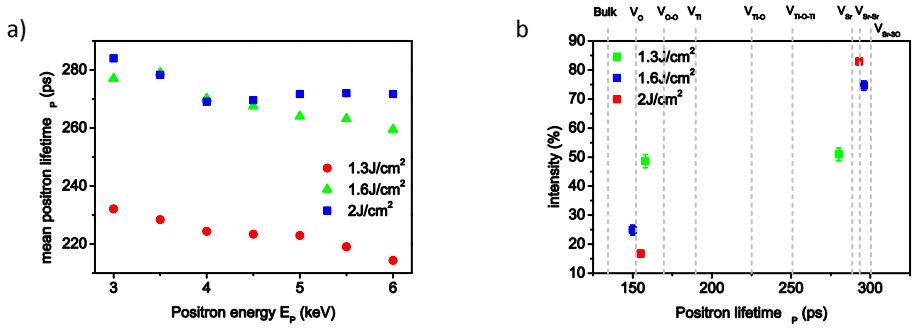


**Figure 6-5:** a) Mean positron lifetimes of the Fe:STO films deposited at different laser fluencies. b) Intensities and characteristic lifetimes for the different Fe:STO films.

Figure 6-5 (a) depicts the mean positron lifetimes of the fluence sequence for the Fe:STO films (2wt%) for typical implantation energies 3keV – 6keV. Figure 6-5 (b) shows the deconvolved lifetimes of figure (a) respectively. All Fe:STO films show strontium vacancies and oxygen vacancies in the film. The laser fluence only seems to vary their ratio.

The intensity of $V_{Sr}''$ decreases with laser fluence. This trend could be explained by the defect incorporation due to the fluence variation, see chapter 5.1.1 where [$V_{Sr}''$] increases with laser fluence. The incorporation of oxygen vacancies for low laser fluence can be interpreted with the ablation characteristics presented in Figure 6-1 (f) where it could be observed that the ablation

characteristic varies more significantly for lower fluencies where the formation of metallic iron seems to be increased in the ablation spot. Therefore, the ablation and deposition of a metallic Fe component could yield an increased amount of oxygen vacancies. This increase in [$V_O^{\bullet\bullet}$] reduces [$V_{Sr}''$] due to the Schottky equlilibrium.
The mean positron lifetimes for the Fe-sequence and the laser fluence sequence is presented below. The decrease of the mean lifetime is a consequence of the formation of oxygen vacancies with higher Fe concentrations or lower laser fluencies.

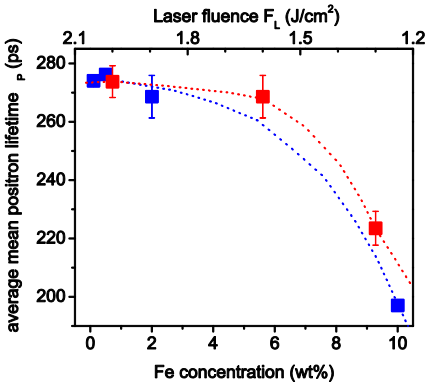


**Figure 6-6:** Average mean positron lifetimes of the Fe concentration sequence with $F_L$: 1.6J/cm² and the fluence sequence for Fe2%. For both sequences; $T_S$: 800°C, $p_{O2}$: 0.1mbar.

With Figure 6-6 it becomes clear, that an increase of the Fe content (in the target) has the same effect as a reduction of the laser fluence on the mean positron lifetime for the Fe:STO films. So far the influence of the plume dynamics on the defect accommodation in Fe:STO films was neglected. Because of the XRD results and ablation characteristics shown above, where the lattice expansion seems to be independent of the actual laser fluence and the ablation changes only slightly with laser fluence the influence of plume kinetics was so far not considered to affect the defect formation in the Fe:STO film.

Nevertheless the plume dynamics and spectroscopy are presented in the following.

## 6.2 PLD Plume Analysis for Fe doped STO

By performing an optical plume analysis the consequences of the reduced ablation rate on the plume kinetics can be observed. The plume spectroscopy of a Fe:STO plume is also shown.

### 6.2.1 Plume kinetics

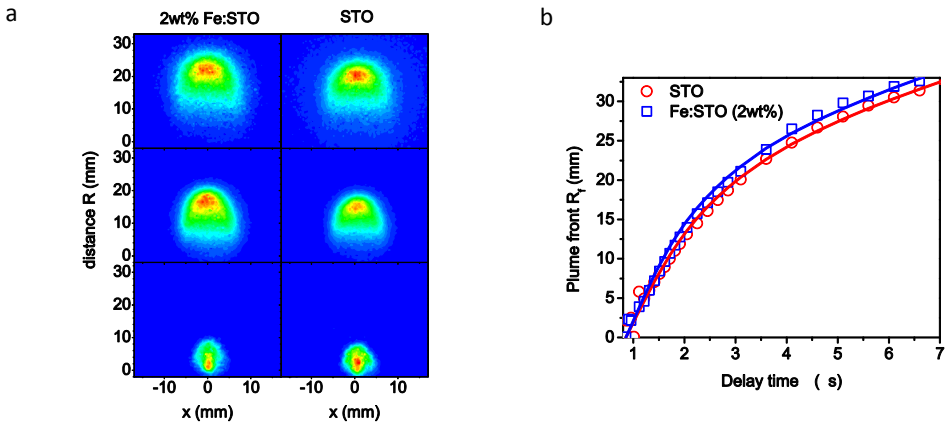


Figure 6-7: **a)** 2D images of the plume front for a 2% Fe:STO and a STO plume at different delay times τ in oxygen ambient with $p_{O2}$: 0.1mbar and $F_L$: 1.5J/cm². **b)** Plume front dynamics of the STO and the Fe:STO plume.

The plume images in Figure 6-7 (a) illustrate a slight difference in the plume shape for the plumes. The Fe:STO plume seems to be more stretched and narrower compared to the STO plume which might be a result of the ablation characteristics of Fe:STO.

The plume front dynamics shown in Figure 6-7 (b) demonstrate that the Fe doped STO plume front does not differ from the STO plume front considerably and a difference is difficult to determine. The STO plume was fitted by adjusting $\boldsymbol{M_p}$ and $\boldsymbol{u_0}$ for $F_L$ = 1.5J/cm² and $p_{O2}$ = 0.1mbar with $T_S$ = 800°C. Based on the fitting for the STO plume the Fe:STO plume was trimmed by bearing in mind a lower ablation rate. The results are listed below.

| | $M_p$ [$10^{-10}$ kg] | $u_0$ [km/s] |
|---|---|---|
| **STO – plume** | 5.2 | 13.3 |
| **(2wt %) Fe:STO - plume** | 5 | 14.8 |

**Table 6-2:** Initial plume mass $M_p$ and initial plume velocity $u_0$ for a STO and a 2wt% Fe:STO plume at $F_L$ = 1.5J/cm²

For Fe:STO the initial plume mass should be slightly lower compared to STO for the same laser energy, see Figure 6-1 (c & d). The initial velocity of the Fe:STO plume is increased whereas the percentage change of the velocity is higher than the mass change.

Because the ablation rate decreases a little further for Fe-concentrations ≥ 2% Fe the mass of the confined plume should decreases as well. Therefore the initial velocity of the Fe:STO plume should increase with Fe doping. This however, can hardly be simulated here.

In any event the change of the kinetic energy and the plume dynamics respectively due to the Fe-doping of the STO target is minute and basically negligible.

### 6.2.2 Plume spectroscopy

In Figure 6-8 the emission lines from a STO and a 2wt% Fe:STO plume are plotted for $\tau$ = 1.6µs. The Fe:STO plume shows the same spectra as the STO plume and no additional characteristic emission lines from iron can be observed in the Fe:STO spectrum.

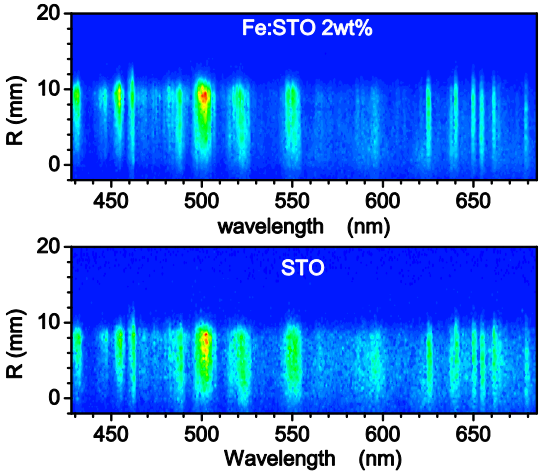


**Figure 6-8**: 2D emission spectra of a Fe:STO and a STO plume for $\tau$ = 1.6µs. The spectrum was taken with $F_L$: 1.6J/cm², $T_S$: 800°C, $p_{O2}$: 0.1mbar.

Comparing in Figure 6-8 the emission lines it seems that the emission lines for the STO plume show more oxidized features than the Fe:STO plume. The emission lines for the STO plume are a little more frizzy and fringy whereas the emission lines of the Fe:STO plume are more defined. This difference would support the theory of the less oxidized species in the Fe:STO plume.

### 6.2.3 TEM investigations of Fe:STO films

Because Fe doped STO depicts a large lattice expansion with a series of vacancy complexes the thin films were investigated by TEM.

Figure 6-9 (a) shows a TEM image for a 10wt% doped Fe:STO film ($d_{Fe:STO}$ ~ 200nm). The investigations by TEM reveal the formation of domains (yellow) within the Fe:STO film which cause an enormous mechanical strain in the film. Along the interfaces between the nano "domain" and its surroundings antiphase boundaries (APB) form. The lattices at the antiphase boundary is strained as depicted in figure (b). Along these APB's a displacement of ~1/2 unit cell is observed in [101] direction. At these boundaries Ti-O octahedra are tilted and along the boundaries oxygen isn't incorporated.

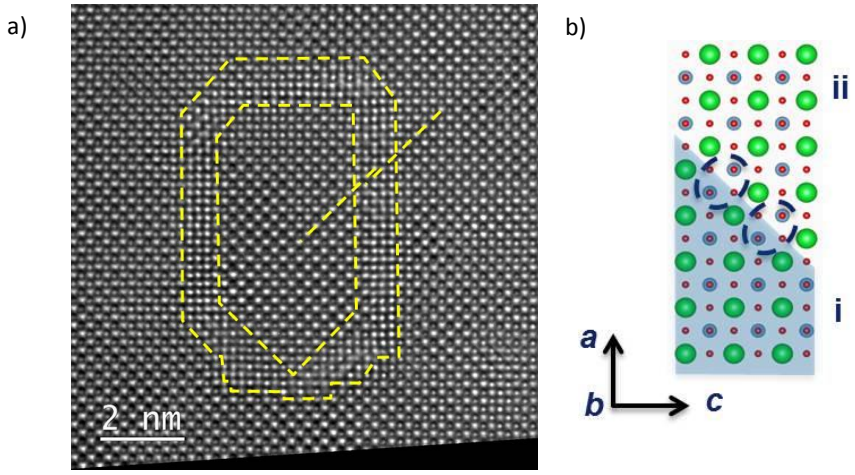


**Figure 6-9: a)** TEM picture of a Fe:STO film with 10wt% Fe. Antiphase boundaries form and induce stress into the lattice. **b)** Schematic illustration of the anitphase boundary with aTi-O shear edge. *Images and Illustration by Hongchu Du, ER-C.*

The formation of such APB's and the deformation of the unit cell would explain the high amount of oxygen vacancies, detected by PALS and the formation of vacancy complexes as well as the large lattice expansion.

## 6.3 Discussion and Conclusions

The XRD analysis of Fe doped STO for different laser fluencies at $p_{O2}$ = 0.1mbar indicates that the lattice expansion due to Fe is independent of preexisting STO stoichiometry.

Fe:STO films with Fe-concentrations < 5% can be regarded as Ti-rich independent of laser fluence and exhibit $V_{Sr}''$ and $V_O^{\bullet\bullet}$ in the thin film. The incorporation of oxygen vacancies is a result of the deposition of metallic Fe-species due to the prospered formation of metallic iron on the target with decreasing laser fluence. The formation of strontium vacancies is regulated by the Schottky equilibrium and decreases with the formation of $V_O^{\bullet\bullet}$.

The XPS results of the ablation spot indicate a Ti-rich ablation which helps to create $V_{Sr}''$ in the Fe:STO system. The intensity of the $V_{Sr}''$-lifetime signal increases with laser fluence and fits well to the fluence characteristics for STO, see chapter 5.1.1 where $[V_{Sr}'']$ increases with laser energy above $f_{LS}$. The suppression of $V_{Ti}''$ could be a result of the Fe doping of the STO system. Because the Fe-concentration is very low the arriving plume species form predominantly a STO film. The added Fe will accommodate unoccupied lattice sites – most likely titanium vacancies.

In chapter 5.1.1 it was shown that the lattice expansion of STO is a function of the $V_{Sr}/V_{Ti}$ ratio. With the incorporation of Fe the concentration of $V_{Ti}$ is reduced and therefore the lattice expansion further increased with $\Delta c \sim V_{Sr}/V_{Ti}$ and $\Delta c \sim 0$ for $V_{Sr}/V_{Ti} \sim 1$.

| | Sr-rich | Stoichiometric | Ti-rich |
|---|---|---|---|
| $V_{Sr}/V_{Ti}$ | > 1 | ~ 1 | > 1 |
| $V_{Sr}/V_{Ti}$ with Fe doping | >> 1 | > 1 | >> 1 |

**Table 6-3:** The Fe-species occupy $V_{Ti}^{''''}$-sites and reduce $[V_{Ti}]$ increasing the $V_{Sr}/V_{Ti}$ ratio and thereby the lattice distortion.

Because Fe-species occupies the $V_{Ti}^{''''}$-sites that are most active for trapping electrons, the Fe:STO films should become more conductive with Fe doping. However, Fe-species on Ti-site transform from $Fe^{4+}$ to $Fe^{3+}$ and thereby trap charge carriers and virtually increase the acceptor concentration $[A_{Ti}']$ in the Fe:STO system which reduces its conductivity.

For Fe:STO films with Fe-concentrations > 5% the amount of Fe-species in the STO species exceeds the solubility limit and a secondary Fe-rich phase forms which creates $V_{Ti}^{''''}$. (Compare the creation of $V_{Sr}^{''}$ for the RP-phase formation).

# 7 Influence of defects on the growth mode of $SrTiO_3$ thin films

The impact of the (non-) stoichiometry of plume and STO films as well as the plume kinetics on the film growth characteristics are described in the following. By RHEED the ad-atom arrangement can be observed in-situ. The film morphology was investigated ex-situ after the deposition process.

## 7.1 Laser fluence variations

It is phenomenological observed via RHEED that non-stoichiometric deposition impacts the growth of a STO thin film. The growth of homoepitaxial STO thin films is observed via RHEED for different laser fluencies (0.95J/cm$^2$ – 2.5J/cm$^2$) with $p_{O2}$ = 0.1mbar, $D_{TS}$ = 44mm and $T_S$ = 800°C. For these settings the laser fluence for a stoichiometric film is $F_{LS}$ = 1.6J/cm$^2$. Figure 7-1 (a) exhibits the RHEED oscillations of the specular spot intensity for STO films grown at various laser fluencies. The increase of the deposition rate with increasing laser fluence can be clearly observed by the width of a single oscillation and is shown in figure (b). It can be seen that the excess of Sr in the STO film ($F_L$ < 1.6J/cm$^2$) can lead to an accelerated formation of 3D nuclei and therefore the abrupt end of a layer-by-layer growth which results in the decrease of the total number of RHEED oscillations, see Figure 7-1 (b). The growth mode is an intricate interplay of diffusion kinetics of ad-atoms and the terrace step length of the vicinal STO crystal surface as well as the deposition rate.

The intensity oscillations for the STO films in Figure 7-1 clearly indicate layer-by-layer growth mode for all systems and the layer-by-layer growth seems to become more stable for higher laser fluencies. With increasing laser fluence the amount of impinging species and hence the deposition rate increases. As shown previously the kinetic energy of arriving species doesn't vary considerably and therefore shouldn't impact the growth mechanism.

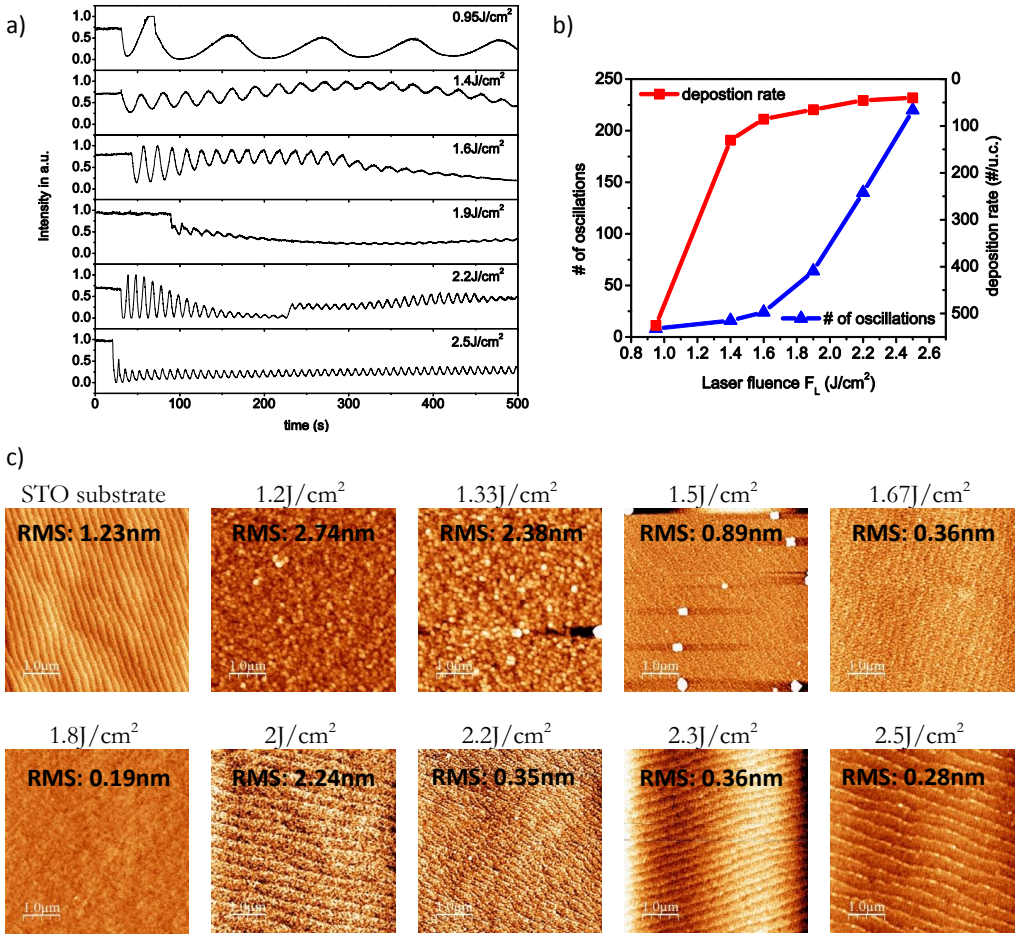


**Figure 7-1: a)** RHEED specular spot intensity oscillations for the growth of homoepitaxial STO films at different laser fluencies $F_L$. **b)** Deposition rate and total number # of RHEED oscillations. **c)** Surface morphology of STO films determined by NC-AFM scans (5 x 5µm). The RMS-value depicts the surface roughness of the films in [nm]. With $d_{STO}$ ~ 200nm $P_{O2}$: 0.1 mbar, $T_S$: 800 °C, $D_{TS}$: 44 mm, $f_L$: 5Hz.

The questions remains however, why the systems grown at high laser fluencies (Ti-rich & less oxidized) exhibit a more stable layer-by-layer growth although the STO film is just as non-stoichiometric as for low laser fluencies. Therefore the kinetic energies and the diffusion kinetics of the ad-atom species are resolved.

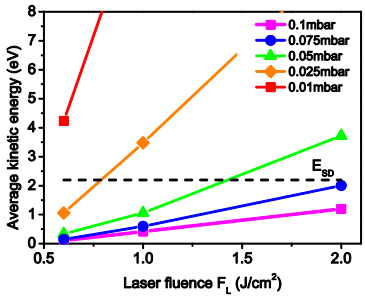


**Figure 7-2:** Calculated kinetic energies of STO plume species for various laser fluencies $F_L$ and background pressures $p_{O2}$ at $D_{TS}$ = 44mm. The activation energy of surface diffusion $E_{SD}$ for STO is ~2.2eV. With

| | 0.6J/cm² | 1J/cm² | 2J/cm² |
|---|---|---|---|
| $M_p$ [$10^{-10}$ kg] | 3.5 | 5.8 | 8.5 |
| $u_0$ [km/s] | 9 | 11.8 | 14.2 |

The kinetic energy of the plume species increases with laser energy and decreasing pressure. As mentioned in the previous chapter, the breakup of bonds is possible for $E_{kin}$ > 30eV. The kinetic energy of the plume species for the films shown above in Figure 7-1 doesn't exceed the activation energy of surface diffusion. This means that the diffusion is still temperatures dependent and not accelerated by the kinetic energy of the plume species.

To investigate the diffusion kinetics of the ad-atoms more closely the relaxation time $\tau$ of the diffusing species was gauged via RHEED and presented below.

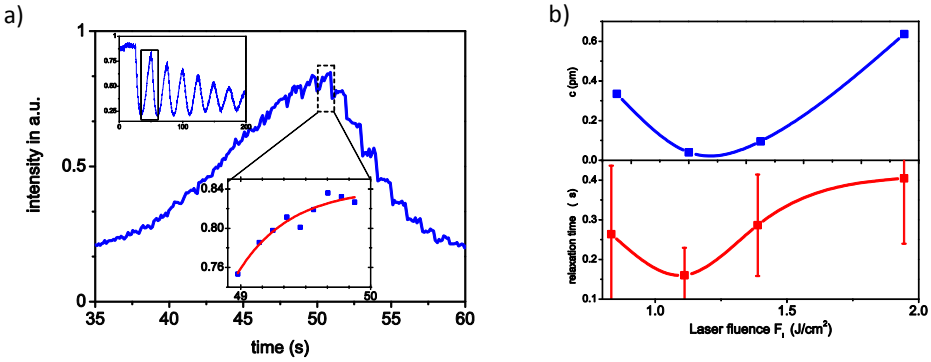


**Figure 7-3: a)** Close-up view of an intensity oscillation of STO grown on STO at $f_L$: 1 Hz with the superimposed intensity modulations. The inset in the top left corner shows the characteristic RHEED intensity oscillations for the deposition. The inset in the middle below depicts the fit (red) to the relaxation time τ of the ad-atoms in between the laser pulses. **b)** Upper (blue) curve describes the c-axis lattice expansion vs. laser fluence. The lower curve (red) shows the relaxation times τ for the STO films. Films were grown at $f_L$: 1Hz, $T_S$: 800°C, $p_{O2}$: 0.1mbar, $D_{TS}$: 40mm.

Figure 7-3 (a) shows a characteristic intensity oscillation captured by RHEED for a deposition of STO on STO. Superimposed are intensity modulations due to the change of the surface coverage after the laser pulses, also see inset top right in Figure 7-3 (a). The intensity drops abruptly after each pulse because of the increased step density as a result of the dispersed ad-atoms on the surface. When these ad-atoms start to diffuse the step density decays and the RHEED intensity

recovers as the ad-atoms move either to the step edges, form nuclei or diffuse to already existing nuclei. The time constant of this recovery is the relaxation time τ.

In Figure 7-3(b) the time constants τ of the recovery processes are plotted for different laser fluencies along with the respective c-axis lattice expansions. The determination of τ for all measurements was the 1st RHEED oscillation maximum as depicted in (a) where the step density is the lowest. Therefore the island density $N_S$ can be considered as constant for all measurements and the surface coverage is almost zero, $\Theta \sim 0$, when the RHEED intensity is at its maximum; hence one can write for the RHEED intensity recovery in this case,

$$I = I_0\left(1 - \exp\left(-\frac{t}{\tau}\right)\right) \tag{7.1}$$

The values of the relaxation times τ and the parameters of the c-axis lattice expansions $\Delta c$ in Figure 7-3 (b) intriguingly follow the same trend. This behavior can be expressed with the equation below.

$$\tau\big|_{\Theta\approx 0} \sim \Delta c \tag{7.2}$$

Merged with equation (4.6) it yields the following expression;

$$\tau\big|_{\Theta\approx 0} \sim \Delta c \sim \frac{1}{D_S N_S} \tag{7.3}$$

As described above, $N_S$ can be considered as constant since all relaxation times τ are determined at the same RHEED position where the RHEED intensity is at its maximum where surface coverage Θ is in principle the same for all systems and equals ~0 and we can write

$$D_S \sim 1/\Delta c \quad \text{with} \quad \Delta c \sim 1 - \left(\frac{V_{Sr}}{V_{Ti}}\right)$$

therefore, (7.4)

$$D_S \sim \left(1 - \left(\frac{V_{Sr}}{V_{Ti}}\right)\right)^{-1}$$

This expression states that the surface diffusion coefficient $D_S$ of ad-atoms appears to be inversely proportional to the lattice expansion $\Delta c$ and the vacancy defect ratio in the STO thin film.

This does **not** mean that the lattice expansion neither the vacancies are a direct result of the surface diffusion kinetics of the ad-atoms. It rather states that the surface diffusion kinetics is influenced by the lattice expansion and the cation vacancies respectively and are therefore a measure of the non-stoichiometry of a growing STO thin film.
The origin of this dependence could be found in the strain of a non-stoichiometric STO thin film. As [31] and others already stated, the incorporation of cation vacancies cause compressive strain effects through Coulomb interactions in an oxide lattice. Therefore the observed changes of the relaxation time might be a direct result of the strained film surface that scales with the non-stoichiometry in the system.
It is known for other systems that surface diffusion kinetics can vary because of the shift in the activation barrier $E_{SD}$ due to a strained surface and these strain-effects can be very material specific [88]. For example compressive strain on the one hand can enhance surface diffusion for metal systems [89], whereas for semiconductors the surface diffusion is impaired [90, 91]. Because the actual STO thin films exhibit a lattice expansion in c-axis that scales with the non-stoichiometry we expect a strained surface and can assess the biaxial stress on the growing surface by [32].

$$\sigma_x = \frac{E}{1-\nu}\frac{a_s - a_0}{a_0} \tag{7.5}$$

with

$$a_0 = \frac{(1-\nu)a_z + 2\nu a_s}{1+\nu} \tag{7.6}$$

Where E is the Young's modulus of STO (189.7GPa), ν the Poisson's ratio (0.232) and $a_z$ the measured out of plane lattice parameter of the film, $a_s$ is the bulk lattice parameter of STO. $a_0$ is the intrinsic stress-free lattice parameter. For the actual case where $a_z > a_s$ equation (2.25) yields a negative stress value and the film is therefore under compressive strain and scales linearly with the lattice expansion which is caused by the cation vacancies.
The development of mechanical stress in the growing STO films doesn't conclusively explain why Ti-rich films with $V_{Sr}''$ show a superior layer-by-layer growth over Sr-rich or even over stoichiometric growth systems.
Sr-rich systems however are known to form Ruddlesden-Popper (RP) phases where an additional SrO plane is incorporated into the STO unit cell. The formation of a SrO layer, can be seen as the incorporation of planar faults which can cause the formation of dislocations that can cause the formation of 3D nuclei.
The increase of the relaxation time τ could be a consequence of the interaction of cation vacancies and diffusion cations on the surface where negatively charged cation vacancies influence the positively charged cations. Therefore the diffusion of cations on the STO surface should be enhanced by the incorporation of oxygen vacancies that shield the electrostatic interaction of cation vacancies and cations.

Furthermore it was phenomenological observed that the minimum of the RHEED intensity oscillations shift systematically with the laser fluence as presented in Figure 7-4.

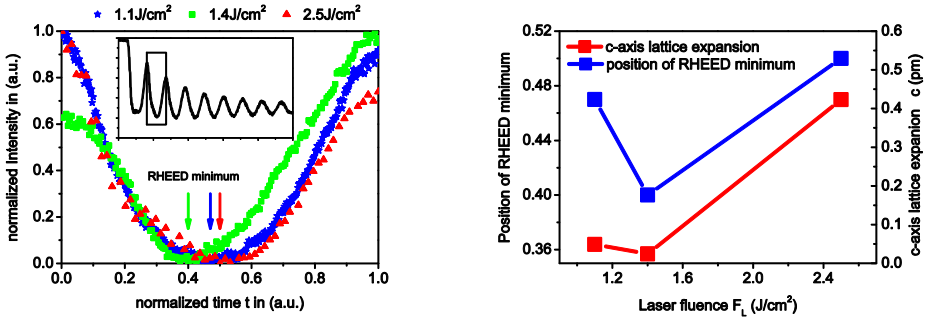


**Figure 7-4: a)** Normalized RHEED oscillations with a normalized time scale of STO films deposited at different laser fluencies. **b)** RHEED minimum position η vs. lattice expansion Δc. With $p_{O2}$: 0.1mbar, $D_{TS}$: 44mm, $T_S$: 800°C, $f_L$: 5Hz.

Figure 7-4 (a) shows the normalized RHEED intensity oscillations for STO films deposited at various laser fluencies. The intensity minimum $\boldsymbol{\eta}$ and can be described by equation (7.7), where $\boldsymbol{t_{min}}$ is the time when the RHEED intensity minimum occurs, $\boldsymbol{t_s}$ is the time for the start of one oscillation (0) and $\boldsymbol{t_e}$ the end of the same oscillation (1). The oscillations starts in the intensity maximum.

$$\eta = \frac{t_{\min - t_s}}{t_e - t_s} \tag{7.7}$$

The intensity minimum occurs at the position where the step density **S** of the growing film is maximal which we can expressed with the following equation

$$\frac{\partial S(t)}{\partial t} = 0 \tag{7.8}$$

which yields the expression

$$\eta \cong \frac{\sqrt{N_S}}{D_S} \tag{7.9}$$

In Figure 7-4 (b) the position of the RHEED minimum is plotted versus laser fluence with the corresponding lattice expansion of the film. The data demonstrates that the shift of the RHEED intensity minimum follows the trend of the corresponding c-axis elongation of the STO thin film. This behavior yields the expression,

$$\Delta c \sim \eta \tag{7.10}$$

and with equation (7.10) we can write

$$\Delta c \sim \frac{\sqrt{N_S}}{D_S} \sim \eta \tag{7.11}$$

$N_S$ is considered as constant since all systems basically depict the same coverage in the RHEED intensity minimum. This yields the following expression which is the same as in equation (7.4).

$$D_S \sim 1/\Delta c \tag{7.12}$$

As explained above the diffusion of species could be affected by the defect incorporation due to stress and strain because of the incorporation of charged cation vacancies. These effects can be observed by effects that strongly depend on diffusion processes.

## 7.2 Background pressure variations

The growth mode of the STO films for different background pressures was characterized by RHEED and is shown below. The RHEED signals shown above demonstrate layer-by-layer growth of the STO film. The films grown at $10^{-3}$mbar $\leq p_{O2} \leq 10^{-6}$mbar were deposited initially at $f_L$ = 1Hz and after 10u.c. at 5Hz. The relaxation of the RHEED intensity after the completion of a STO monolayer (1u.c.) increases gradually with decreasing pressure. Additionally, the number of oscillations rises as well for lower background pressures. Both observations portray an improved surface quality of the growing film for lower pressures which could be a direct result of the increased kinetic energy of the arriving species.

As described by Willmott et al. in [92] the flux of high energetic species can break up small islands (no sputtering) and thereby inhibit a proliferation of large-diameter 2D island and the creation of 3D seeds. The bond strength of SrO is 430 kJ/mol which is about 5 eV. TiO has a bond strength of 670 kJ/mol which resembles ~7 eV. With an average maximum kinetic energy of 30 eV (see Table 5-4 & Figure 7-2) and an average bond strength of 6 eV only 5-fold bonds can be cracked at max by the arriving species at low pressures. The bonds of cations on the STO surface are 5-fold in the case of Ti and 4-fold in the case of Sr. The surface morphology of the films is shown in Figure 7-4 (b). The surface roughness decreases with decreasing pressure confirming the suppression of bigger islands due to the fragmentation of nuclei on the surface.

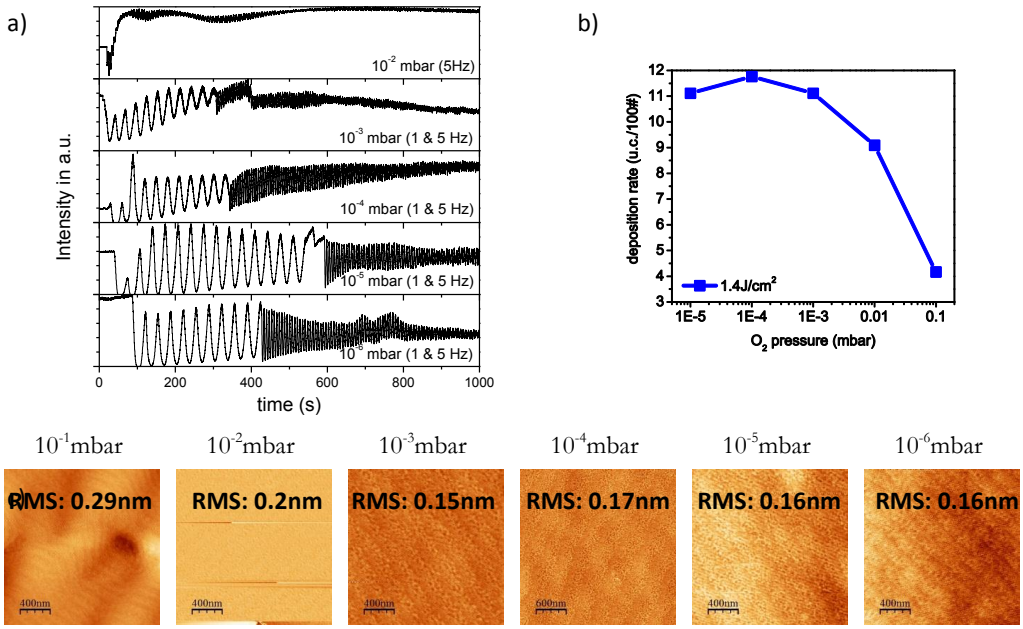


**Figure 7-5: a)** RHEED oscillation for STO films grown on STO for different $O_2$ background pressures. **b)** deposition rate vs. $O_2$ background pressure. c) Surface morphology of STO films determined by NC-AFM scans (2 x 2µm). With $T_S$ = 800°C, $D_{TS}$ = 44mm, $f_L$ = 1.6J/cm², $f_L$ = 5Hz.

The relaxation time $\tau$ as well as the shift of the relative RHEED minimum $\eta$ that were measured for different background pressures follow the same trend of the lattice expansion Δc. This was already observed in the case of the laser fluency sequence, see chapter 5.1.1. It was concluded that $\Delta c \sim V_{Sr}''/V_{Ti}''''$. The same conclusion can be applied here.

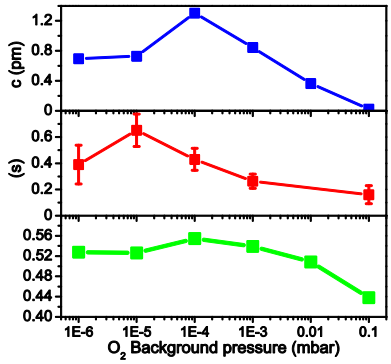


**Figure 7-6**: Relaxation time τ and RHEED minimum η vs. background pressure compared with the lattice corresponding lattice expansion. $D_{TS}$: 40mm, $T_S$: 800°C, $F_L$: 1.4J/cm², $f_L$: 1Hz

Since the nascent plume in Figure 5-10 is Ti-rich the $V_{Sr}''/V_{Ti}''''$ ratio in the STO thin film increases with decreasing pressure since less Ti species are scattered during the ToF and the film becomes increasingly Ti-rich which yields the incorporation of $V_{Sr}''$ and the reduction of $V_{Ti}''''$.
Beyond $10^{-4}$ mbar the increased incorporation of $V_O^{\bullet\bullet}$ inhibits the creation of $V_{Sr}''$ (Schottky equilibrium) and the cation vacancy ratio drops. Therefore the relaxation time decreases accordingly.
Because the average kinetic energy of the species exceeds 2.2eV for $p_{O2} < 0.02$mbar at R = 33mm the arriving species should enhance the surface diffusion and the relaxation time should therefore decrease. However, the measured relaxation times give no direct hint towards a facilitated surface diffusion.
It was concluded before that a non-stoichiometric STO surface slows the diffusion which could overshadow the effect of a facilitated surface diffusion due to the increased kinetic energy of the arriving species with decreasing pressure. Especially when a decrease in Pressure facilitates a non-stoichiometric plume, see Figure 5-26.

## 7.3 Effect of substrate temperature

As mentioned before, the growth kinetics are temperature dependent. Therefore the change of the growth mode of a film due to temperature can be gauged by RHEED. The characteristic RHEED intensity oscillations indicate a 2D layer-by layer growth where nuclei are formed, grow bigger, coalesce and eventually form a new monolayer. If diffusion kinetics are high, ad-atoms can diffuse towards the step edges on the substrate surface without the formation of nuclei which is termed as step-flow growth. During this process the step density on the surface doesn't change effectively. Therefore the RHEED signal shows no change in intensity. Samples grown at 650ºC – 950ºC were grown at the beginning with $f_L$ = 1Hz and then after 3 – 4u.c. with 5Hz.

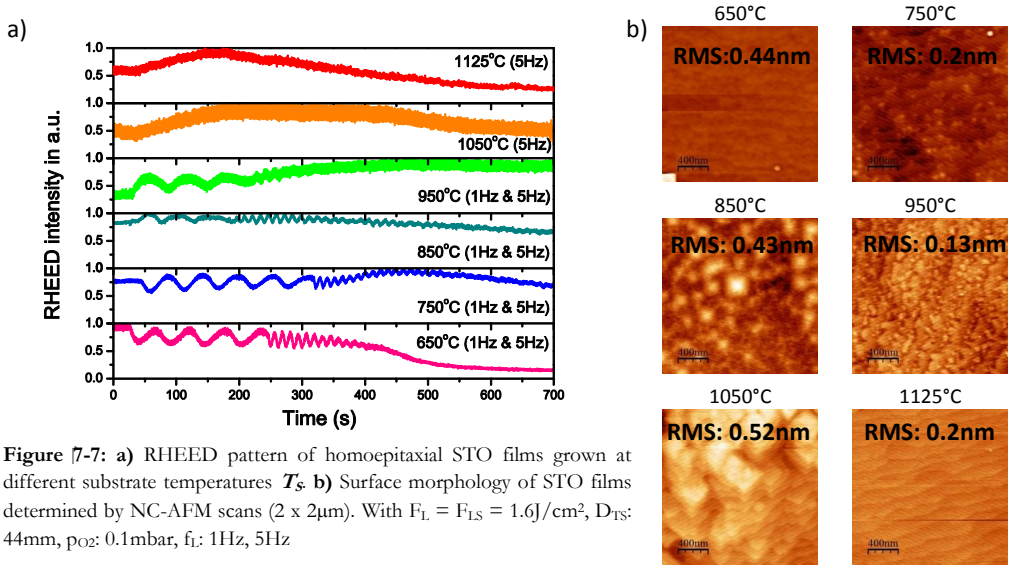


**Figure 7-7: a)** RHEED pattern of homoepitaxial STO films grown at different substrate temperatures $T_S$. **b)** Surface morphology of STO films determined by NC-AFM scans (2 x 2µm). With $F_L = F_{LS} = 1.6J/cm^2$, $D_{TS}$: 44mm, $p_{O2}$: 0.1mbar, $f_L$: 1Hz, 5Hz

The RHEED patterns in Figure 7-7 depict a layer-by-layer growth for films grown at $T_S < 950°C$ and step flow growth for $T_S > 950°C$. The transition from layer-by-layer growth to a step-flow growth occurs at ~950°C. The transition point is very difficult to pin point in general since it depends for example on the step terrace length $l_{st}$ and the thermal activation of the diffusing species.

## 7.4 Influence of Fe doping on the STO film growth

It was shown in chapter 6.1 before that doping STO with Fe results in a distortion of the thin film that is much bigger than by the usual deviations from non-stoichiometry. For that reason the film growth characteristics of Fe:STO are investigated to find out if the Fe-doping has a substantial effect on the growth process.

In-situ RHEED patterns are presented in Figure 7-8 (a) for Fe-doped STO films grown on STO substrates. The resulting surface morphologies of the Fe:STO film ($d_{Fe:STO}$ ~ 200nm) are depicted in figure (b). The RHEED patterns reveal a common layer-by-layer growth mechanism which eventually ends due to 3D nucleation formation. In principle the RHEED patterns are the same independent of the doping concentration with a maximum number of oscillations of 13 - 20# which is not different from the undoped STO system deposited at the same laser fluence ($F_L = 1.6J/cm^2$).

The same is true for the film topography. Although the c-axis depicts enormous deviations compared to undoped STO systems, the surface morphology is in principle the same.

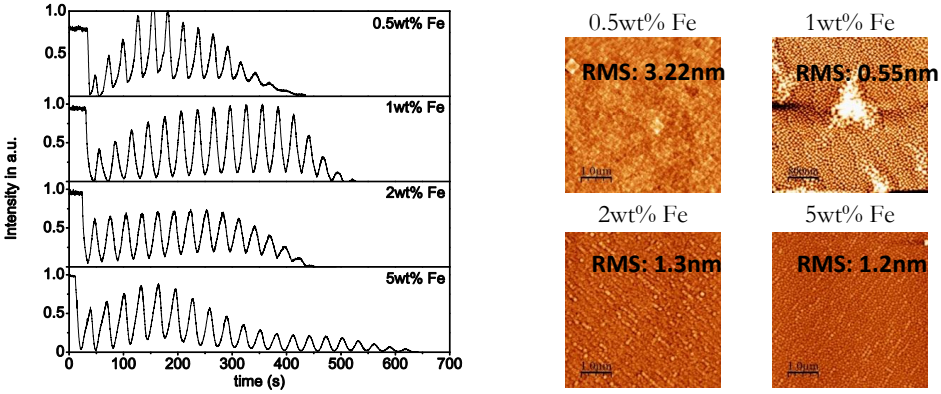


**Figure 7-8: a)** RHEED oscillation for Fe doped STO films grown on STO with different Fe-concentrations. **b)** NC-AFM scans of Fe:STO films. With $T_S$ = 800°C, $D_{TS}$ = 44mm, $F_L$ = 1.6J/cm², $f_L$ = 5Hz

The resulting film topographies in Figure 7-8 are not any different from the undoped STO films presented before. Further analysis of the RHEED pattern revealed a systematical shift of the relative RHEED minimum $\eta$ with the Fe-concentration that follows the trend of the lattice expansion.

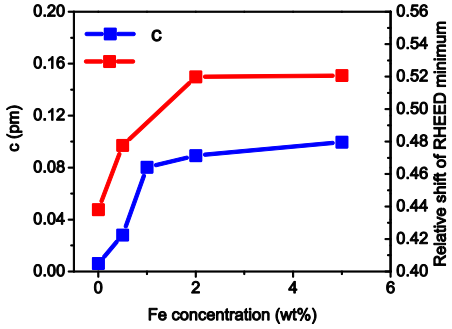


**Figure 7-9:** Shift of the relative RHEED minimum η versus Fe doping concentration in STO compared with the corresponding lattice expansion.

## 7.5 Discussion and Conclusions

In general it can be concluded that aiding the thin film growth process by increasing the surface temperature or facilitating the kinetic energy of the arriving species improves the growth process which can be observed by an increased number of RHEED oscillations for layer-by-layer growth or the transition to step-flow growth.

However, the majority of cation defects depend on the stoichiometry of the PLD plume. A non-stoichiometric PLD plume introduces a specific ratio of cations and cation defects respectively. This cation vacancy ratio seems be responsible for the observed lattice expansion.Increasing the kinetic energy of plume species by reducing the background pressure results in an improved layer-by-layer growth due to the fragmentation of nuclei on the film surface. Such an improved layer-by-layer growth does not result in a lower defect incorporation though.By increasing the

surface temperature the non-stoichiometry remains for films deposited at background pressures below 0.1mbar. The overall concentration of defects can be reduced in this manner but the lattice expansion remains.

In general no correlation between surface topography and defect concentration and non-stoichiomtry respectively could be found.
Defect incorporation and non-stoichiometry strongly depends on the ablation and plume transport process. It can also be concluded that surface diffusion is strongly influenced by the stoichiometry of the growing STO thin film.

# 8 Investigations of the resistive switching properties of STO thin films

The fundamentals of the resistive switching (RS) phenomenon were described earlier in chapter 2. There, it was also shown that several RS mechanisms have been categorized so far. The so called VCM mechanism of $SrTiO_3$ will be investigated in the following. The origin of the resistance change and the processes within the oxide are still in dispute and under scrutiny. The common denominator responsible for the VCM mechanism is the mobility and movement of oxygen vacancies although not all resulting resistance states and electrical properties can be explained by the re-arrangement of the oxygen vacancies.

Because both, mobility of ions and charge carriers are created upon the formation of defects in the oxide they play the key role in the RS mechanism [9, 10]. Based on the defect engineered STO thin films the RS properties of the films are characterized in the following and the role of specific defects for the RS mechanism elucidated.

The $SrTiO_3$ thin films for characterization of their RS properties are deposited on 0.5wt% Nb doped $SrTiO_3$ (Nb:STO) single crystals. Nb:STO serves as the bottom electrode since Nb:STO exhibits an almost metallic conductivity where $Ti^{4+}$ ions are replaced by $Nb^{5+}$ ions. The additional electron of the Nb-ion (0.5wt%) generates a nominal doping level of $N_D \sim 10^{16} cm^{-3}$ and therefore turns the STO crystal into a n-type material. The band structure of Nb:STO is shown below.

The STO thin film thickness ranges from 0.8 – 6.4nm for LC-AFM studies, and 20nm for ex-situ investigations with MIM structures.

## 8.1 LC-AFM investigations of the RS properties of STO thin films

Many attempts are being made to probe the RS properties by so called MIM structures where the active oxide is sandwiched in between two micro or nano-structured metal electrodes. With this technique the RS properties of the oxide can be tested. However, subsequent analysis of the oxide in between the metal contacts is extremely tricky and the origin of the RS mechanism difficult to decipher.

Therefore a new approach was devised to investigate the origin of the RS mechanism by utilizing an AFM probe as one of the electrodes. The attractiveness of this technique is the prospect of examining the oxide on the nano-scale.

Probing the electrical properties of an oxide by local conductivity AFM (LC-AFM) was so far done by several researchers [93, 40]

In the actual case however, $SrTiO_3$ thin films are investigated quasi in-situ after the deposition process where the specimen is transferred from the deposition tool (PLD) to the SPM tool under UHV conditions. Hereby, re-oxidation of the film is prevented and artificially designed thin film properties, such as low oxygen contents, non-thermodynamic states created by annealing and quenching can be preserved and their influence on the RS properties investigated.

For LC-AFM investigations, either a Pt/Ir coated Si tip was utilized or a heavily boron doped diamond (BDD) tip. The work function $\phi_m$ of both materials are similar (Pt: 5.12 – 5.93eV, BDD: 5.2eV) and chemically inert. The advantage of the BDD tip is its structural stability at high currents when the resulting temperature load would cause a damage of the Pt/Ir coating. Additionally, the abrasive degeneration of the BDD tip is basically zero whereas the Pt/Ir coating wears off with time when the tip is scanned over the STO-surface.

The electron affinity of $SrTiO_3$ is $X_{STO}$ = 3.9eV according to [94]. Depending on the Fermi level EF the work function $\phi_{STO}$ can vary between 7.1 – 3.9eV, given the band gap of $SrTiO_3$ is $E_{g/STO}$ = 3.2eV.

**Experimental**

For the investigations of the resistive switching properties of the STO thin films with LC-AFM a voltage is applied to the AFM-tip with respect to the bottom electrode which is grounded, see Figure 8-1. STO thin films with different stoichiometry are investigated and listed in Table 8-1.

| STO film | $p_{O2}$ [mbar] | $F_L$ [J/cm$^2$] | $T_S$ [°C] | $f_L$ [Hz] | $d_{STO}$ [nm] |
|---|---|---|---|---|---|
| **Stoichiometric** | 0.1 | 1.4 | 800 | 1 | 6.4 ~ 16 u.c. |
| **Ti-rich** | 0.1 | 2 | 800 | 1 | 6.4 ~ 16 u.c. |
| **Sr-rich** | 0.1 | 0.9 | 800 | 5 | 6.4 ~ 16 u.c. |

**Table 8-1:** PLD process parameters for the deposition of STO thin films for resistive switching investigations

It is important to note, that all specimen were annealed, prior to the LC-AFM investigations, in oxidizing conditions at $p_{O2}$ = 0.1mbar and $T_S$ = 800°C for about 10min and quenched to room temperature. Such annealing conditions result in a p-type conductivity for STO (equilibrium condition). This condition can be captured by quenching.

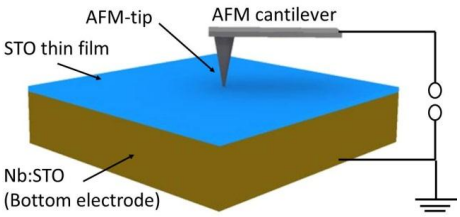


**Figure 8-1:** Schematics for resistive switching of STO films on Nb:STO by LC-AFM. The AFM-tip constitutes the top electrode whereas the Nb:STO describes the bottom elecrtrode.

### 8.1.1 Pristine I(V) characteristics of STO thin films

After deposition, the films were cooled down to room temperature at 0.1 mbar oxygen ambient. Subsequently the specimens were transferred under UHV condition to the SPM module and probed by LC-AFM for their electrical characteristics. The pristine characteristics are shown in Figure 8-2.

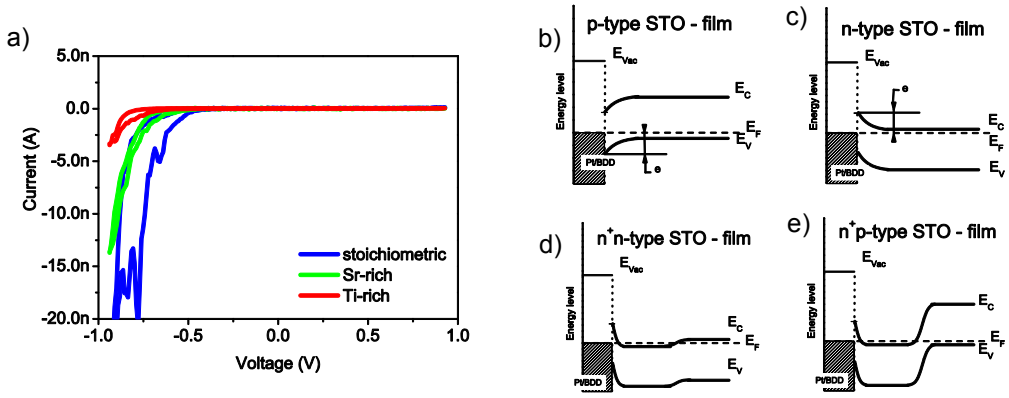


**Figure 8-2: a)** I(V) curves for pristine STO films with different stoichiometry and $d_{STO}$ = 16u.c. Energy band diagrams for **b)** p-type STO in contact with Pt or BDD in equilibrium forming a Schottky contact ($\phi_m < \phi_{STO}$), **c)** n-type STO in contact with Pt or BDD in equilibrium forming a Schottky contact ($\phi_m > \phi_{STO}$), **d,e)** Ohmic contact between $n^+$-type STO and Pt with a n-type or p-type STO below the $n^+$-type STO.

The I(V) curves of all 3 films with different stoichiometries exhibit similar rectifying behavior and resemble the characteristic of a Schottky diode-like junction [95, 96]. The forward direction occurs for a negative bias at the AFM tip which indicates a p-type behavior of the STO film, see Figure 8-2 (b). Also, the currents in forward direction vary with the stoichiometry of the STO film, see dashed line in Figure 8-2 (a).

A Schottky contact between the metal (AFM-tip) and a semiconductor (STO) can form in general if the p-type semiconductor shows a work function bigger than the metal work function, $\phi_m < \phi_{STO}$ or if the n-type semiconductor shows a smaller work function than the metal work function, $\phi_m > \phi_{STO}$.
The electron affinity of STO is according to [94] 3.9eV. If we assume an average Fermi level at $E_F \approx 0.48$eV above the valence band due to the acceptors ($V_{Sr}''$ & $V_{Ti}''''$ or $Fe'''$) in the STO film which act as acceptors according to [16] the work function $\phi_{STO}$ of the STO film therefore yields a value of 6.62eV which constitutes a bigger work function compared with the work function of the platinum or boron doped diamond and consequently a Schottky contact between the AFM-tip and the p-type (acceptor doped STO) thin film is formed.

For high donor doping of the oxide by e.g. oxygen vacancies ($V_O^{\bullet\bullet}$), the oxide would be essentially an n-type semiconductor with a Fermi level at ≈0.21eV according to [16] below the conduction band. This would yield a STO work function of $\phi_{STO} \approx 4.11$eV. Since in this n-type case the work function of the metal contact (AFM-tip) is bigger than the work function of the oxide a Schottky contact is formed as well. Therefore, for all doping scenarios in STO (acceptor doped, donor doped) a Schottky like contact will be formed between the AFM-tip (Pt, BDD) and the STO film.

The observation presented above however, is controversial with respect to a p-type behavior of the $SrTiO_3$ films which so far couldn't be confirmed experimentally at room temperature. Doping STO extrinsically with Sc- or In- atoms will result in a p-type behavior and has been so far experimentally investigated by [97-98, 25].
Gunkel has shown in [22] for LAO/STO heterostructures (2DEG) that the mobility of charge carriers $\mu_n$ decreases with the non-stoichiometry of the STO film at 300K which was attributed to the scattering of charge carriers by acceptor like cation vacancies. LAO/STO systems quenched after annealing at 1050K in reducing environment ($10^{-23}$mbar $O_2$) yielded an electron mobility $\mu_n$ independent of the STO stoichiometry which was attributed to the healing of cation vacancies and showed that the concentration of cation vacancies in the STO film is <1at%.
This however, could also be a result of an over-compensation of cation vacancies by oxygen vacancies yielding an intrinsic n-type behavior.

The actually observed p-type behavior, described above, could therefore be explained by the post-annealing and quenching of the specimen in the oxidizing PLD-process environment ($10^{-1}$mbar $O_2$) at 1050K. This (oxidation-) process reduces the concentration of $V_O^{\bullet\bullet}$ according to equation (8.1 as already shown in chapter 2.

$$\frac{1}{2}O_2 + V_O^{\bullet\bullet} \leftrightarrow O_O^x + 2h^{\bullet} \qquad \textbf{(8.1)}$$

In this case the cation vacancies are then compensated by holes $h^{\bullet}$ which in turn could result in a latent (extrinsic) p-type conduction mechanism which is the consequence of a non-equilibrium state of the STO film due to the quenching in an oxidizing environment. By quenching, the p-type conductivity could be captured and preserved to room temperature.

### 8.1.2 1D resistive switching characteristics of STO films

The general I(V) characteristics of a resistive switching device for memristive devices were depicted in chapter 2. It was shown that a system can exhibit either a so called **8**-wise or a counter-**8**-wise I(V) hysteresis loop.
The STO films with 3 different stoichiometries and $d_{STO}$ = 6.4nm were therefore probed for their I(V) hysteresis loop characteristics and are depicted below. The I(V) sweeps were performed without a forming step and swept from: 0 → +3.8V, +3.8V → -3.8V, -3.8V → 0V with 0.25Hz and a compliance current $I_{CC} = \pm 25\mu A$.

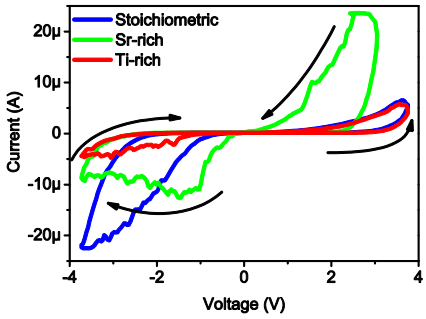


**Figure 8-3:** RS-I(V) characteristics of STO films with $d_{STO}$ = 6.4nm and different stoichiometry. All films show an **8**-wise hysteresis loop.

All films exhibit an **8**-wise hysteresis where the loops show diverse characteristics though that might be a direct result of their inner defect constellation and stoichiometry. The Sr-rich film shows a strongly defined switching where the passage through the origin depicts the steepest I(V) curve indicating a high resistance ratio between the high resistance state (HRS) and the low resistance state (LRS).

All system switch into the LRS after a specific positive threshold voltage for a positive voltage where the current increases suddenly. By applying a negative bias the effect can be reversed and the system switches into the HRS. The Sr-rich films exhibit hereby a so called negative differential resistance (NDR) where the voltage is further increased and the current decreases exemplifying the increase of the resistance of the system.

To verify that a change of resistance is responsible for the hysteresis in Figure 8-3 and not a parasitic capacitance, the I(V) curve of the Sr-rich film was probed by different voltage amplitudes and frequencies. A consequential property of a so called "memristive" system is the so called pinched hysteresis loop where the current response to a sinusoidal voltage signal is pinched at the origin [99]. Also, with increasing frequency of U(t) the I(V) hysteresis loop should decrease in its amplitude. A capacitive system would exhibit an increase of the I(V) hysteresis loop with increasing frequency.

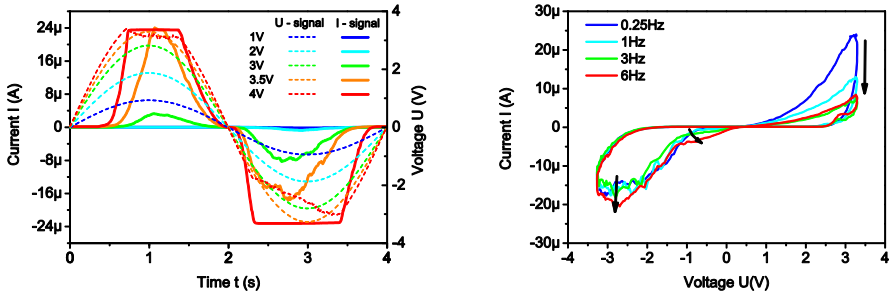


**Figure 8-4: a)** pinched hysteresis loop by amplitude variation of the sinusoidal voltage signal. **b)** Response of hysteresis loop to different frequencies of the sinusoidal signal U(t) indicates a memristive behavior and no capacitive.

The response of the system to different voltage amplitudes is shown in Figure 8-4 (a) and the reaction to a change in sweep-frequency is depicted in figure (b). The "pinching" of the hysteresis loop can be clearly observed for U = 3.5V. When the scanning frequency is increased the set-amplitude decreases whereas the reset amplitude doesn't change.
In essence, the pinched hysteresis loops in figure (a) and the decrease of the amplitude with frequency in figure (b) describe the resistive switching properties of the STO thin films and demonstrate that capacitive effect are not the reason for the observed hysteresis loops.

**Spatial dimensions of the switching phenomenon**

When the I(V) sweeps shown above are executed via the AFM tip the material changes its resistance state upon this stimulus. The spatial dimensions of this phenomenon can be observed by scanning the AFM tip over the treated area with an applied read-out voltage of +0.5V. The topography and the conductivity are recorded simultaneously. For the set-process the AFM-tip was swept from 0V → +4V with 0.25Hz. Then the surface (200 x 200nm) was scanned with a biased AFM-tip (+0.5V). For the reset-procedure the AFM-tip was placed at the same spot as for the set-process and treated with a voltage sweep of 0V → -4V with 0.25Hz. The surface was scanned again with a +0.5V biased AFM-tip over an area with 200 x 200nm. The results are depicted below.

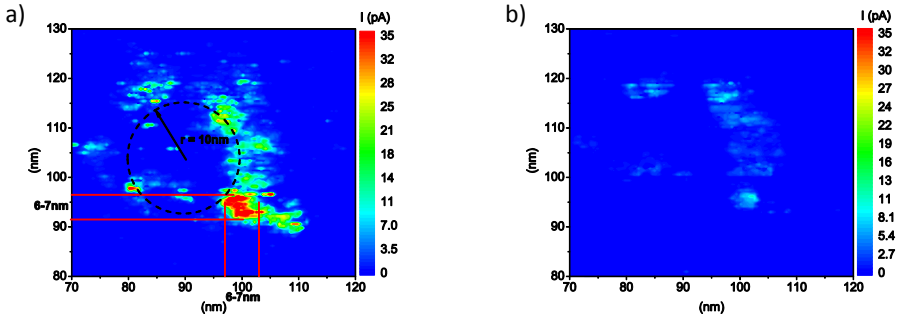


**Figure 8-5: a)** 2D scan with $U_{tip/read}$ = +0.5 V of the LRS after positive voltage sweep 0V → +4V **b)** 2D scan with $U_{tip/read}$ = +0.5V after negative voltage sweep 0V → -4V

Figure 8-5 (a) & (c) presents the conductivity and the topography of the STO film surface after the SET-sweep (0 – 4V) to transform the system into the low-resistance-state (LRS). The thin film surface shows no signs of a change in topography after the SET process. The gauged current however, exhibits spots of high conductivity. These conductive zones seem to be in the circumference of the AFM-tip which is known to have a radius of ~10 nm. The conductive zones have an average dimension of 6 - 7nm.
With a reset-sweep (0 – -4 V) the system was reset into the high-resistance-state (HRS). The mapped conductivity in figure (b) shows that the conductive zones from the LRS exhibit now a much lower conductivity. Their spatial arrangement hasn't changed which demonstrates that the

switching process is a local phenomenon. Also, the topography was not affected by the RESET-process.

### 8.1.3 LC-AFM characteristics of $SrTiO_{3-x}$

To probe the behavior and for the electrical properties of STO upon the rearrangement of oxygen vacancies in the system a STO single crystal was investigated by LC-AFM for different oxidation states. Therefore a STO single crystal was "doped" with oxygen vacancies ($SrTiO_{3-x}$) by annealing at high temperatures in vacuum and then quenched to room temperature. With a biased AFM-tip the positively charged oxygen vacancies can be moved. The measurement setup is shown below.

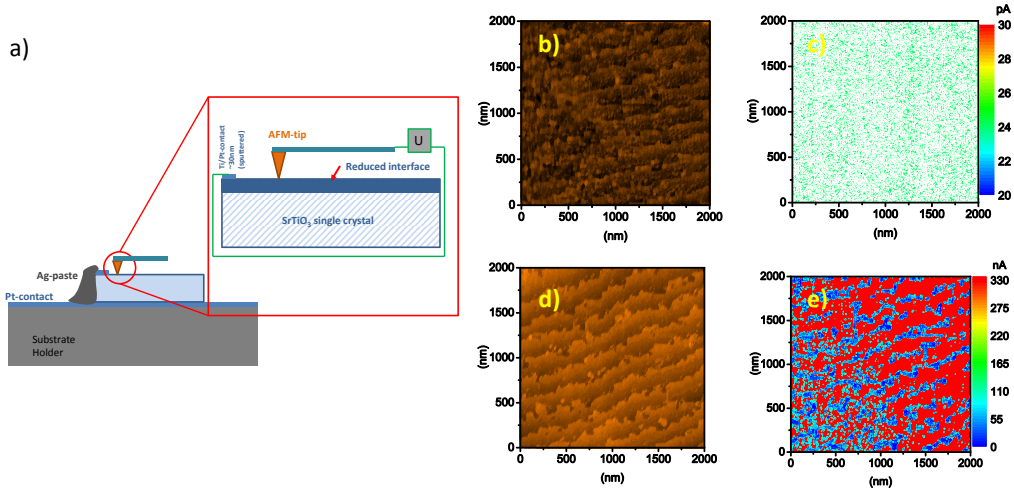


**Figure 8-6: a)** LC-AFM measurement setup to probe the effect of oxygen vacancies on the conductivity of a STO single crystal. Topography **(b)** and conductivity **(c)** of the STO single crystal annealed at $T_S$ = 950°C in atmosphere for t = 4 hrs with $U_{tip/read}$ = +0.1V. Topography **(d)** and conductivity **(e)** of the STO single crystal annealed at $T_S$ = 700°C with $P_{ambient} = 4 \cdot 10^{-8}$mbar for t = 45min with $U_{tip/read}$ = +0.3V.

The pristine STO crystal was probed by LC-AFM after annealing at 950°C for 4 hours in atmosphere as depicted in Figure 8-6 (a). The applied read-out voltage of $U_{tip/read}$ = +0.1V at the AFM tip detected essentially no conductivity of the STO surface, see figure (c). The STO crystal was then moved into a UHV annealing chamber and treated at $p = 4 \cdot 10^{-8}$ mbar and $T_S$ = 700 °C for 45 minutes. After cooling down to room temperature the crystal was moved back in-situ in a UHV ambient with $p = 10^{-9}$ mbar to the LC-AFM system and probed with a voltage of +0.1V again. This time the STO surface clearly exhibits conductivity as shown in figure (e). The conductivity map also reveals the vicinal surface of the STO crystal with low conductivity spots along the step edges. The vicinal surface of the STO crystal surface in figure (b) & (c) exhibit an improvement of the surface quality due to annealing in vacuum. Major variations of the surface cannot be observed though. The reduced condition can be reversed into the oxidized high

resistance condition (not shown here) by oxidation at $p_{O2}$ = 0.1mbar with $T_S$ = 700ºC for 45min and exhibits the same conductivity as depicted in figure (c). This process reveals that the STO system owes its conductivity to the oxygen vacancies $V_O^{\cdot\cdot}$ and the condition can be reversed via oxidation.

The low resistance state can also be reversed into the HRS by changing the polarity of the applied voltage as can be seen by the I(V) sweeps in Figure 8-3. To determine if the STO crystal doped with oxygen vacancies exhibits the same properties, the AFM tip was scanned first with a positive voltage of +0.75V over the reduced surface to mimic a transfer into the LRS and then the tip was scanned with -0.75V over a smaller area to transfer the system into the HRS. Subsequently the AFM tip was scanned over both areas with a read-out voltage of +0.1V. The conductivity map of the read-out is shown below.

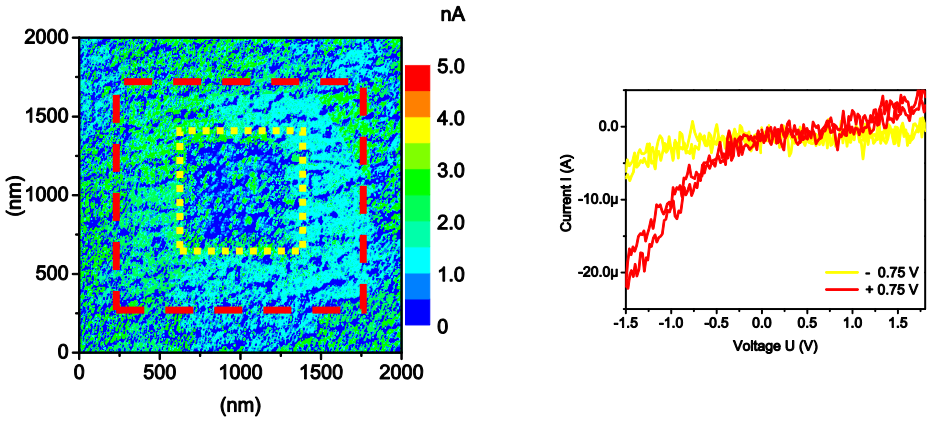


**Figure 8-7: a)** Conductivity map on a reduced STO single crystal acquired by LC-AFM with $V_{tip/read}$ = +0.1V. The red area depicts where the STO surface was treated with $V_{tip}$ = +0.75V and the yellow area depicts where the STO was treated with $V_{tip}$ = -0.75V. **b)** 1D voltage sweep for both areas shows the result of the treatment on the I(U) characteristics.

The conductivity map in Figure 8-7 reveals that the STO system doped with oxygen vacancies doesn't further increase its conductivity by a positive applied bias to the AFM tip (red-dashed square) but that the system can be reversed into the HRS by applying a negative bias to AFM tip (yellow-dotted square). Surprisingly the area that was treated with a negative AFM-tip, which should cause oxygen vacancies (positive charge) to accumulate near the surface, shows a higher resistance than the area treated with a positive bias which should repel oxygen vacancies.

This map also clearly demonstrates that the switching effect occurs at the AFM tip (Schottky contact) and not at the counter electrode (Ohmic contact) because only where the negative biased AFM-tip was scanned over the $SrTiO_{3-x}$ surface does a change in conductivity occur. However, not all spots within the HRS areas show a change of the resistance state.

The LRS and HRS areas were also probed for their I(V) characteristics shown in Figure 8-7(b). The HRS area reveals a similar rectifying characteristic as the as-deposited STO thin films in Figure 8-2 where the system is in forward direction for a negative polarization in reverse for the

positive polarization which indicates a p-type behavior of the system despite the oxygen vacancy doping which introduces electrons as charge carriers which should introduce a n-type character. The LRS area exhibits conductivity for both polarities however with a lower conductivity for a positive polarization. The Schottky barrier in $\phi_{SBH}$ positive direction seems therefore to be reduced by the high concentration of oxygen vacancies.

### 8.1.4 Resistive switching mapping (2D) of STO thin films

As demonstrated before in Figure 8-6 the resistance states can be mapped by scanning a biased AFM-tip over the oxide surface. With the same principle resistance states can be inscribed into the oxide by scanning the AFM-tip over an area with a characteristic SET or RESET voltage.
It is important to consider here that the contact of the tip and the surface can be disturbed by the lateral scanning movement and the constant adjustment of the normal force due to the constant force control mode. This could influence the SET, RESET and READ processes and the detected values of current cannot be taken as "real". Also the contact area is therefore difficult to determine. Therefore, it would be misleading to make any quantitative conclusions based on the measurements like the determination of the Schottky barrier height, or band gap etc.

Now the SET, RESET and READ characteristics of STO thin films (16u.c.) on a Nb:STO bottom electrode are investigated. First, the the SET-process for different stoichiometric STO films is investigated and presented below. Therefore the AFM-tip is scanned over an area of 800 x 800nm with a tip bias of +1.3V.

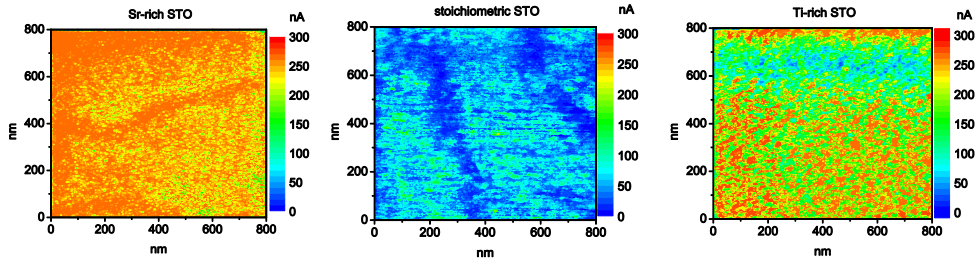


**Figure 8-8:** SET-process characteristics of STO films with different stoichiometries with a set-voltage of $V_{SET}$ = +1.3V.

In Figure 8-8 the currents during set-processes for STO films with different stoichiometries are shown. The maps reveal that the SET-current is influenced by the stoichiometry of the STO film and that non-stoichiometric STO film exhibit a larger MIEC than the stoichiometric STO film. The Sr-rich STO film shows the biggest mean current of ~260nA followed by the Ti-rich film with ~210nA. The smallest current is detected for the stoichiometric STO film with ~50nA.

To detect a change in resistance due to this stimulus the AFM-tip is scanned over same area with a scan width of 1400 x 1400nm and a READ-out voltage $U_{read}$ of +0.2V. The detected currents are presented below.

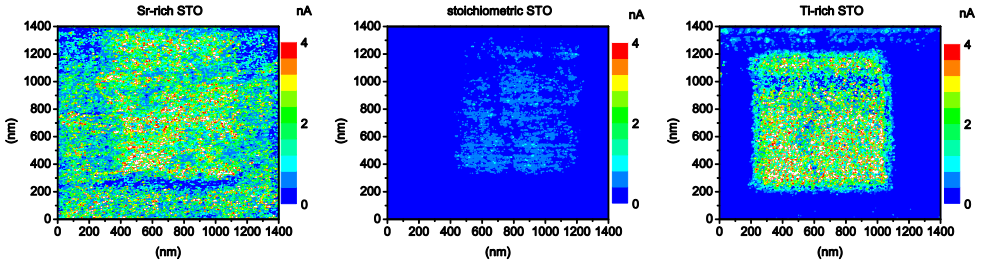


**Figure 8-9:** Read-out maps of the SET-state for STO films with different stoichiometries with $V_{read}$ = +0.2V.

The conductivity maps in Figure 8-9 depict the resistance change that occurs after the set-scan as well as the pristine conductivity of the STO thin films.
The maps reveal that the Sr-rich STO film shows the highest pristine conductivity whereas the Ti-rich STO films exhibits the highest current in the set-area. The resistance ratios between the pristine area and the SET-area are listed below.

| | Sr-rich | Stoichiometric | Ti-rich |
|---|---|---|---|
| $R_{pristine}/R_{LRS}$ | ~2.5 | ~25 | ~300 |

**Table 8-2:** Resistance ratios between the pristine and the set-state for STO films with different stoichiometries.

The conductivity detected at a voltage of $V_{read}$ = +0.2V is predominantly electronic due to a very low ionic contribution since the electric field is too low to effectively move ions at +0.2V. The electronic conductivity is a result of the concentration of charge carriers and their mobility.
By applying a negative voltage to the AFM-tip the LRS can be set back into a high resistance state as shown below. Therefore, an area of 300 x 300nm within in the LRS-area was treated with $V_{reset}$ = -1.3V.

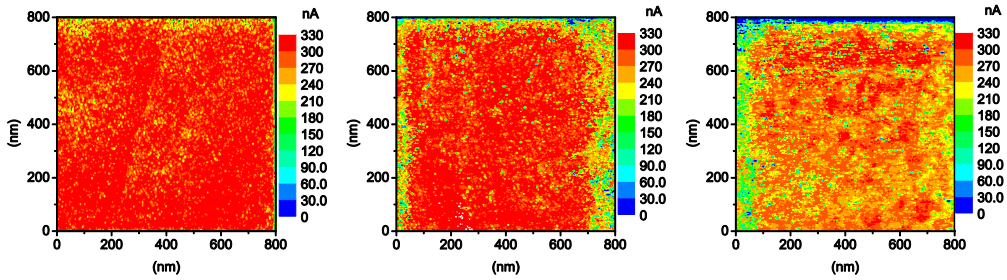


**Figure 8-10:** Reset conductivity map for STO films with different stoichiometry. **a)** Sr-rich STO, **b)** stoichiometric STO, **c)** Ti-rich STO.

The conductivity maps in Figure 8-10 show for all STO films a relatively high reset current. A dependence on the stoichiometry isn't observable. Subsequently the STO surface was scanned with $V_{read}$ = +0.2V with 1400 x 1400nm to determine the change of the resistance state.

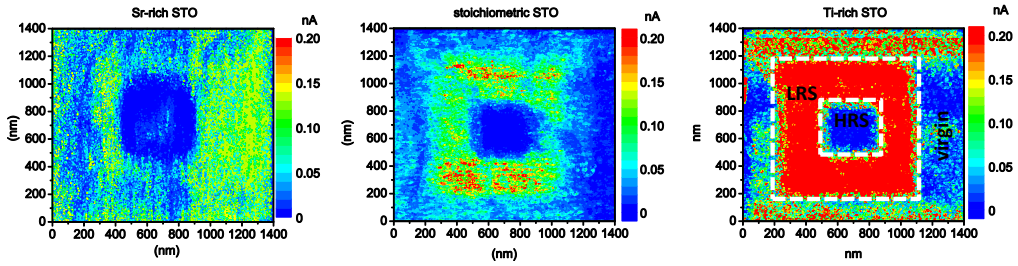


**Figure 8-11:** Conductivity maps for STO films with different stoichiometries with LRS, HRS and pristine area. The LRS area was inscribed with $V_{set}$ = +1.3V, the HRS area was inscribed into the LRS area with $V_{reset}$ = -1.3V. The read-out voltage $V_{read}$ is +0.2V. With $d_{STO}$ = 16u.c.

The conductivity maps in Figure 8-11 demonstrate that the LRS can be reversed into a HRS by applying a negative bias to the AFM-tip. The conductivity of the HRS is the same or lower than the pristine conductivity.

This graphic representation of the resistance states further demonstrate the RS-properties of the STO and demonstrate that the resistance change is a change of the material properties and not only a change of the contact characteristics since the LRS and HRS can be laterally confined. Moreover, the conductivity maps in Figure 8-11 demonstrate the dependence of the RS characteristics on stoichiometry. In general, as shown in Figure 2-3, the electronic contribution dominates. If the electronic current increases the mobility of oxygen vacancies can increase due to joule heating.

The STO films with non-stoichiometry exhibit a higher conductivity than the stoichiometric films. The conductivity is a function of charge carrier concentration and mobility it is difficult to decipher which contribution determines the increased conductivity for non-stoichiometric STO films. For low voltages the electronic conductivity dominates over the ionic for two reasons, first, the electric field can be not sufficient to move $V_O^{\bullet\bullet}$, second, if the electronic current is low there is no joule heating effect which facilitates an ionic ($V_O^{\bullet\bullet}$) mobility. Comparing the Ti-rich and stoichiometric STO film, the electronic conductivity at low voltages are similar. For higher voltages (SET) the detected current is higher for the Ti-rich STO as well as for the Sr-rich film.

As mentioned in the beginning of this chapter, the STO films were quenched in oxidizing conditions where acceptors (A', i.e. $V_{Sr}''$ & $V_{Ti}''''$) are compensated by oxygen vacancies ($V_O^{\bullet\bullet}$), as shown in chapter 2.2. In chapter 5 it was demonstrated by PALS that non-stoichiometric films depict a higher concentration of cation vacancies. This would argue for an increased $V_O^{\bullet\bullet}$ concentration in non-stoichiometric films as well. This could lead in consequence to an increased MIEC for the Ti-rich and Sr-rich systems.

However, the concentration of these compensating oxygen vacancies is constant and independent of the oxygen partial pressure in oxidizing and moderately reducing conditions see Figure 2-2 in chapter 2. The number of charge carriers ($h^{\bullet}$ & $e'$) however, have a dependence on the acceptor concentration with $n \sim (1/[A'])^{1/2}$ and $p \sim [A']^{1/2}$ according the mass action where the concentration of holes increases with $[A']$. Such holes could also contribute to the detected increased conductivity for non-stoichiometric STO films. The high pristine conductivity of the Sr-rich film could therefore be explained by a high concentration of holes $h^{\bullet}$ however wasn't investigated any further.

It is important to mention here, if electrons contribute considerably to the conduction, then, joule heating which scales with the electronic current could facilitate the mobility and drift velocity of $V_O^{\bullet\bullet}$ which eventually leads to a non-linear ionic drift behavior also described in [100]. Due to the AFM-tip polarity during the SET-process (+), oxygen vacancies are effectively repelled from the STO surface and oxygen ions ($O^{2-}$) are attracted to the surface. This process could lead to removal of oxygen vacancies by so called anodic oxidation where oxygen molecules (gas) are formed and oxygen vacancies created which is further discussed in chapter 8.1.7. This process could transform the system from extrinsic p-type to an intrinsic system with $n \sim [V_O^{\bullet\bullet}]$. The lowest SET-current and pristine conductivity in total is detected for a stoichiometric STO film. The incorporation and movement of oxygen vacancies is probably less pronounced due to the inherent low defect concentration in a stoichiometric STO film.

The current during the RESET-process shows the same characteristics for all three systems. This would indicate that all three systems are in the same state regardless of their acceptor concentration. This would indicate that the system is indeed in the intrinsic regime after SET where the conductivity depends on the oxygen vacancy concentration and electrons dominate the conductivity.

### 8.1.5 I(V) characteristics of the pristine, LRS and HRS area

After inscribing the resistance states LRS and HRS into the STO thin films they are analyzed for their I(V) characteristics. Therefore the AFM-tip was set on an arbitrary spot within the specific region and swept from -1V to +1V. The results are presented below.

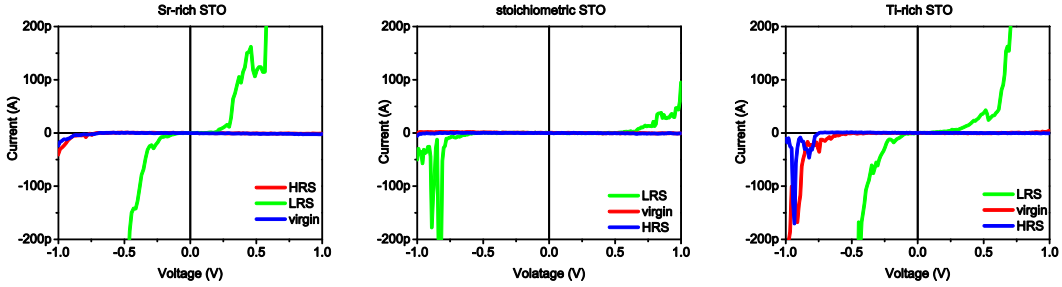


**Figure 8-12:** I(V) characteristics of inscribed HRS, LRS and pristine areas of STO films with different stoichiometries.

The measurements presented in Figure 8-12 depict the I(V) characteristics of inscribed LRS and HRS areas as shown in Figure 8-11 for STO films with different stoichiometry. All films exhibit for the pristine state a rectifying behavior as already presented in Figure 8-2. The I(V) characteristics of the HR-state resembles the pristine state for all STO films which demonstrates that the LRS is a reset into the initial conditions.
Because the resistance of the system depends on the concentration of oxygen vacancies the resistance should be scalable by systematically varying the oxygen vacancy concentration. This is demonstrated in the following where an area (200 x 200nm) is scanned with the AFM-tip with either a positive or a negative bias with 1V. After each scan the I(V) response of the same spot is determined and presented below.

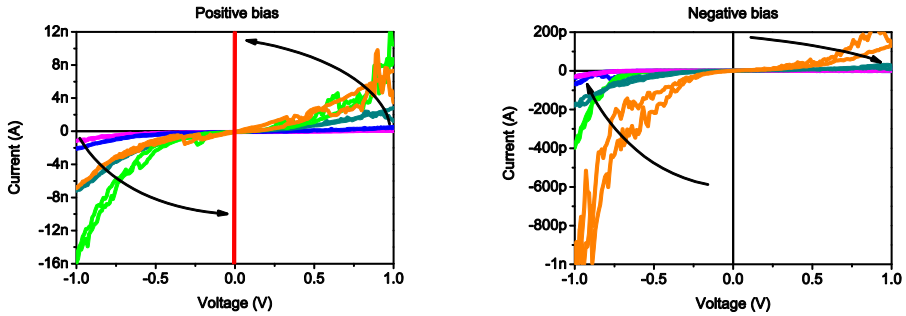


**Figure 8-13: a)** I(V) characteristics for a LRS area. Repeatedly rotating an I(V) sweep (-1V - +1V) and an AFM 2D-scan with +1V. **b)** I(V) characteristics (-1V - +1V) of a HRS area after repeated AFM 2D scanning (-1V).

The measurements in Figure 8-13 depict the I(V) response of the scanned area after each scan. After each scan with +1V the current increases and eventually results in a breakdown of the oxide, figure (a). In the same manner the current decreases after each scan with a negative voltage of -1V, see figure (b). The increase and decrease of the current value seems not to follow a linear trend. For a better understanding the current values of the I(V) response at ±0.75V are presented below for the positive and the negative bias scans.

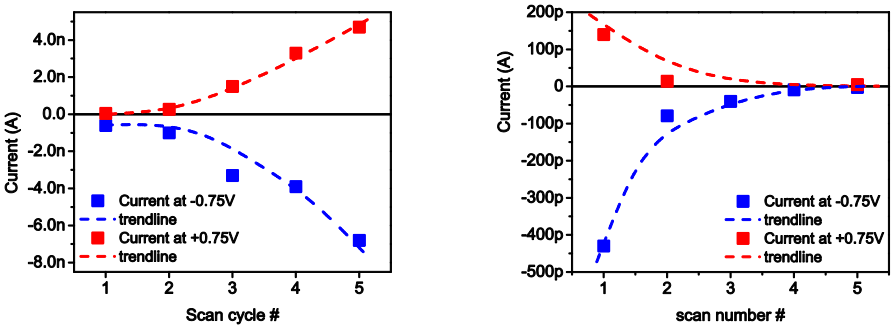


**Figure 8-14:** Current values after each scan in forward (FF) and reverse (REV) direction at ±0.75V with **a)** positive bias (+1V), and **b)** negative bias (-1V).

The current response in forward and reverse direction after the SET-scan with +1V and the RESET-scan with -1V in Figure 8-14 demonstrate that the current increases or decreases non-linearly with each scan although the scan settings remain the same. The SET and RESET process seem therefore to be a self-supporting process.
As the inscribed areas in Figure 8-11 demonstrate, the LRS can be reset into the HRS by applying a negative bias to the AFM-tip. Therefore, the reset characteristics are investigated by applying voltage sweeps on arbitrary spots in the LRS and the HRS region.

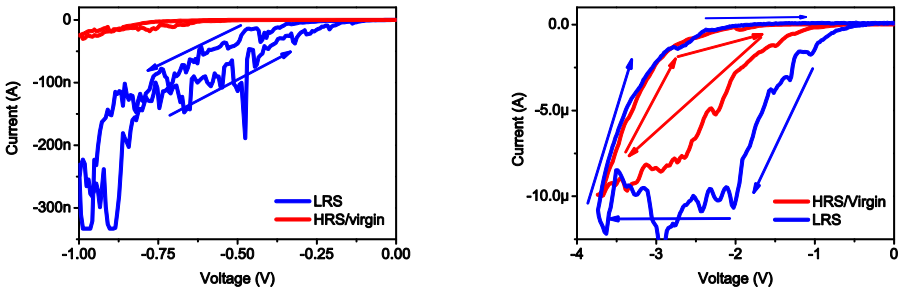


**Figure 8-15:** I(V) characteristics of the reset process for a LRS and HRS area. **a)** Low voltage characteristics of LRS and HRS. **b)** Higher voltage characteristics of the LRS and HRS area. The LRS exhibits eventually a NDR and resets into the HRS.

The curves in Figure 8-15 (a) show the current response to a small negative voltage bias and a relatively large negative voltage bias in figure (b). Figure 8-15 (a) reveals that for a small negative bias the resistance state of the LRS-spot doesn't change.
When a larger bias is applied the system switches into a HRS as can be seen by the I(V) sweep in Figure 8-15 (b). The I(V) characteristic reveal a so called negative differential resistance (NDR) below -2V where the current decreases or remains almost constant although the voltage is further increased in value. If the voltage sweep is executed in the HRS area the I(V) curve shows below -2.5V also a decrease in the current response which has NDR characteristic.
When the voltage bias is decreased again (-4V → 0V) the current response for a specific voltage is much lower indicating an increase in resistance. During the NDR a process must have occurred that resets the LRS into the HRS. The interesting aspect of the two I(V) curves in figure (b) is that the LRS as well as the HRS both show NDR characteristics and the resistance of the HRS can even be further increased.

The I(V) characteristics shown in Figure 8-12 (a) & (c) for the LR-state present an electric current in both directions, positive- and negative-bias without a rectifying characteristic anymore. The current in positive bias demonstrates that the LRS area has no blocking character anymore as it is for the pristine or HRS area due to the Schottky contact. The direct onset of the current for a negative bias hints either to a reduction or a removal of the Schottky barrier.
The I(V) characteristics of the LRS-area for the stoichiometric STO film, in Figure 8-12 (b), resembles a pn-junction with a tunneling breakdown [95] (page 98). This observation in

conjunction with the theory of an incorporation of oxygen vacancies near the surface during the SET-process could lead to the following theory.
The p-type STO film is gradually n-type doped by incorporation of $V_O^{\bullet\bullet}$ starting from the surface and eventually becomes highly conducting as demonstrated in Figure 8-13.
This process can be observed by the non-linear trend of the conductivity shown in Figure 8-14 where the STO film becomes more conducting after each scan (with a positive bias to the AFM-tip) which is illustrated in Figure 8-16.

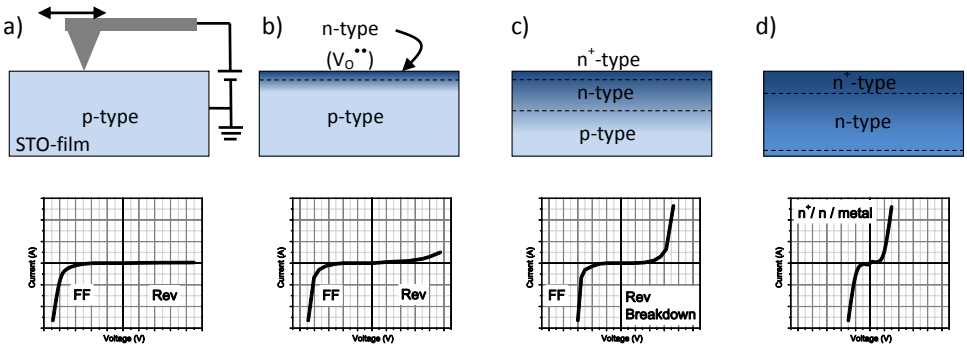


**Figure 8-16:** Doping schematics during the SET-process (scanning) of the STO film with oxygen vacancies and the resulting I(V) characteristics. **a)** Pristine I(V) characteristics, **b)** 1st scan with low positive voltage, **c)** 2nd scan with low positive voltage, **d)** 3rd scan with a low positive voltage or after a 1st scan with a high positive voltage. FF – Forward direction, Rev – Reverse direction.

When oxygen vacancies are incorporated during the SET-process a pn-junction forms which is biased in forward direction (FF) for a negative AFM-tip bias and biased in reverse for a positive bias, figure (b). At the same time a Schottky contact is formed between the n-type STO and the AFM-tip which is in forward direction for a positive bias.
With each scan, more oxygen vacancies are incorporated into the STO film which in turn increases the electronic current. With increasing electronic current the effect of joule heating increases as well which facilitates the mobility of oxygen vacancies and so on, see also [100].

The NDR characteristics observed in Figure 8-15 show an almost constant current during the I(V) sweep with negative bias which is indicative of the formation of a process that counteracts the flow of current through the system systematically and seems to be therefore current controlled. Such NDR characteristics were described before by Alexandrov et al. [101] for $TiO_x$ systems where it was concluded that the system regulates itself due to joule heating which curbs the current.
Such current controlled negative resistances are also common for tunnel devices and were observed also for MIS-diodes or pn-tunnel diodes [95] (page 549 & 518). During the RESET-process positive oxygen vacancies are attracted towards the STO surface and a $p^+n^+$-diode could form again as already depicted in Figure 8-16 (c & b). When a forward bias is applied to the

junction (negative bias at the n-type region), electrons tunnel from the $n^+$-type side to the $p^+$-type side, as shown in Figure 8-17 (b) & (c). When the voltage is further increased the band alignment allows for fewer electrons to tunnel and the current decreases and eventually ceases, see also Figure 8-17 (d) & (e). Therefore, both effects, the drift of $V_O^{\cdot\cdot}$ to the surface and the formation of a $p^+n^+$-tunnel diode could lead to the observed NDR (less current with increasing voltage) when a negative bias is applied to the AFM-tip.

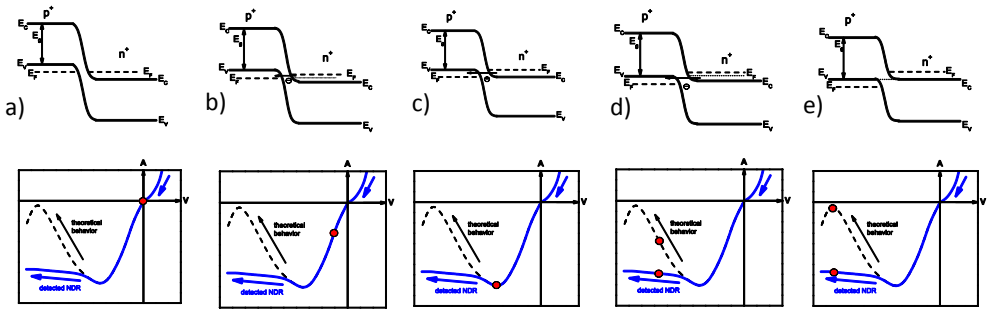


**Figure 8-17:** Schematic energy band diagrams and I(V) curves for the NDR during the RESET-process if a $n^+$-type and a $p^+$-type area emerges. **a)** Equilibrium condition, **b),c),d)** Direct tunneling, **c)** Maximum tunnel current, **e)** No tunneling possible – but thermal current flow possible if voltage is further increased.

The schematics in Figure 8-17 show that the current is maximized when the Fermi level of the $n^+$-region is aligned with the valence band of the $p^+$-region. If the voltage is further increases (nominally) the current decreases. When $E_V$ and $E_C$ of the $p^+$ and $n^+$ region respectively are aligned, no tunneling is possible. Only thermally assisted current flow is possible. Due to joule heating this process could set on earlier when the current is in the maximum where tunneling and thermal assisted current flow happen at the same time. Therefore the current doesn't decrease much further when the voltage is further increased (nominally).

### 8.1.6 Thickness dependence on the RS effect for STO films on Nb:STO

The I(V) measurements of the STO thin film for the pristine, HRS and LRS area show various characteristics that resemble Schottky contacts as well as pn-diode tunnel junctions. To determine which conduction mechanism is most likely and which mechanism leads to the low and high resistance state is extremely difficult. It is assumed that oxygen vacancies and their movement towards the Schottky-like contact determines the resistance state by influencing the charge carrier emission due to variation of the potential barrier i.e. Schottky barrier $\phi_{SBH}$.
Therefore extremely thin STO films with a thickness of only 2u.c. deposited on Nb:STO are investigated for their I(V) characteristics. Also, the LRS is mimicked by doping the STO with oxygen vacancies. The results are shown below.

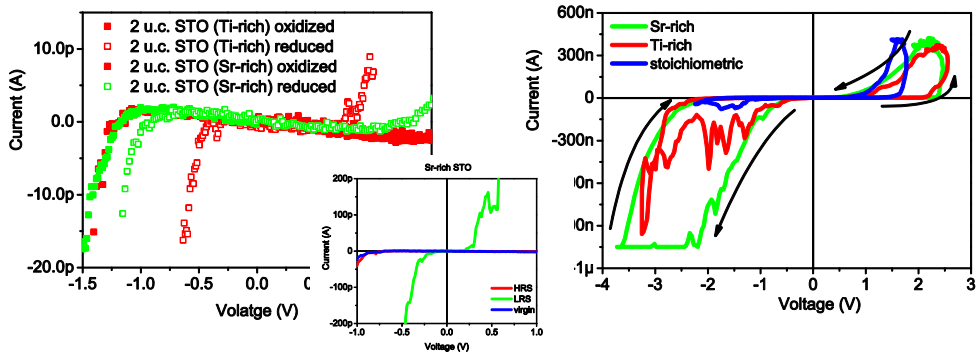


**Figure 8-18: a)** I(V) characteristics of pristine and reduced STO films with $d_{STO}$ = 2u.c. (~0.8nm). **b)** RS characteristics of thin STO films.

The I(V) measurements depicted in Figure 8-18 (a) show the same rectifying behavior of the pristine state as the thicker STO films in Figure 8-2. The reduced STO films show the same I(V) characteristics as the LRS state presented in Figure 8-12. Both observations indicate that the thickness of the STO films has apparently no effect on the electronic properties. Furthermore, the resistive switching characteristics of the thin STO films (2u.c.) shown in Figure 8-18 (b) are basically not different compared with films with 16u.c. thickness, see Figure 8-3.

Despite the thickness of the STO film (2u.c.) the RS-curves in Figure 8-18 (b) show deviations for the different stoichiometries which exemplifies that the stoichiometry of the STO influences the RS characteristics. Because of the STO-film thickness of only 2u.c., only electronic perturbations due to stoichiometric variations would come into effect. The dependence of the RS effect on the stoichiometric variations of the STO can be demonstrated by inscribing different resistance states into the 2u.c.-thick structures as presented below.

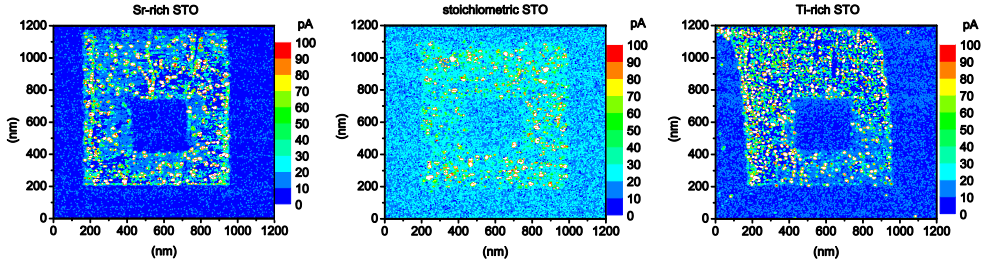


**Figure 8-19:** Inscribed resistance states into STO with $d_{STO}$ = 2u.c. deposited onto Nb:STO. **a)** Sr-rich STO, **b)** stoichiometric STO, **c)** Ti-rich STO.

The inscribed areas in Figure 8-19 demonstrate how the stoichiometry affects the exchange of charge carriers for different resistance states. Within 2u.c. STO, a re-arrangement of oxygen vacancies could be possible, however, a chemical gradient would be not sustainable because only 4 oxygen atom layers are stacked upon each other, see Figure 8-20. The resistive switching effect for such a system with 2u.c. STO must therefore stem from another entity.

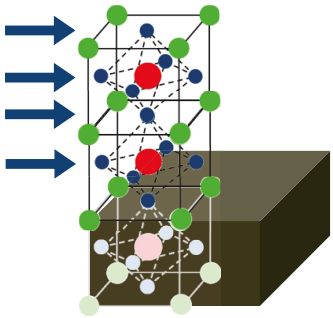

**Figure 8-20:** STO film with 2u.c. thickness on Nb:STO substrate. Ti-atoms – red, Sr-atoms – green, oxygen atoms – blue.

Nb:STO is used as the bottom electrode and known to have resistive switching properties [102] despite its metallic character due to a high Nb concentration. Its I(V) properties are discussed in the following.

The general I(V) characteristics of a Nb:STO (0.5wt% Nb) single crystal are shown below. Prior to the I(V) investigations the Nb:STO crystal was annealed for 4 hours at 950°C in air. Subsequently the crystal was vacuum annealed ($10^{-8}$ mbar) and investigated with LC-AFM and finally sputtered with $Ar^+$-ions and also investigated by LC-AFM.

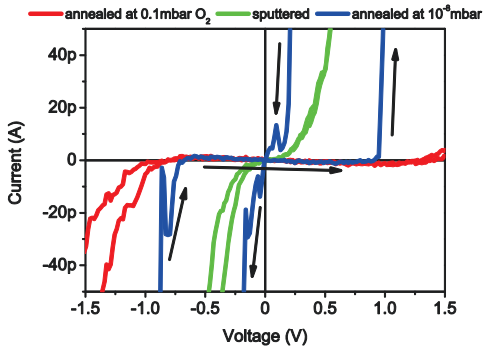


**Figure 8-21:** I(V) characteristics of Nb:STO (0.5wt%) for different treatments. Nb:STO with p-type characteristic after annealing in oxygen at 0.1mbar. Metallic or $n^-$ characteristics after sputtering. Strong RS characteristic after annealing in vacuum (doping with oxygen vacancies). I(V) scans were performed with 0V → +1.8V → -1.8V → 0V with 0.25Hz.

The I(V) characteristics of the Nb:STO single crystal are shown in Figure 8-21 for different treatments. Nb:STO (0.5wt%) annealed in 0.1mbar oxygen ambient at $T_S$ = 800°C shows the same rectifying p-type characteristic as the STO thin films, (red curve). When the crystal in annealed in vacuum it is doped with oxygen vacancies and exhibits even for small voltages a resistive switching effect, (blue curve). The resistive switching I(V) sweep reveals the same 8-wise hysteresis loop direction as the STO films shown in Figure 8-3 with a much more distinct LRS/HRS state which can be seen by the almost vertical slope for the LRS and the horizontal line for the HRS. The inscribed 2D resistance states are presented below and underline the good switching properties of the Nb:STO crystal. When the surface of the Nb:STO crystal is sputtered with $Ar^+$-ions the crystal depicts a typical metallic behavior, (green curve). This demonstrates that the metallic properties of Nb:STO lie deeper in the crystal.

To visualized the RS effect for Nb:STO, resistance states were inscribed into a Nb:STO (0.5wt%). The crystal was annealed at 0.1mbar in $O_2$ and treated with $V_{SET}$ = 3V, $V_{RESET}$ = -3V and $V_{READ}$ = 0.4V. The inscribed resistance states in Figure 8-22 for Nb:STO show the same RS behavior as for STO films.

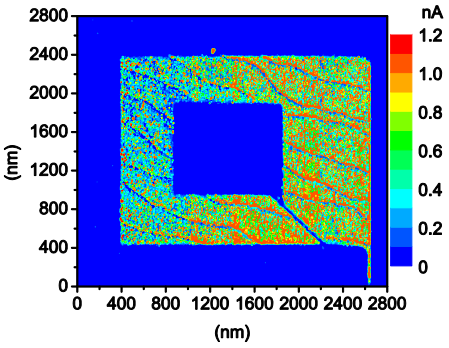


**Figure 8-22:** Inscribed LRS and HRS into Nb:STO annealed at 0.1mbar $O_2$. With voltages appied to the AFM-tip of $V_{SET}$ = +3V, $V_{RESET}$ = -3V, $V_{READ}$ = 0.4V

### 8.1.7 Discussion

The LC-AFM investigations of STO films with $d_{STO} \leq$ 16u.c. on Nb:STO revealed all a 8-wise switching mechanism. All pristine STO films show all a p-type characteristic with a Schottky contact between the AFM-tip and STO film. The p-type character could be a consequence of quenching the sample in a oxidizing environment where p-type conductivity dominates, compare with Figure 2-2 in chapter 2. It was also shown that a Nb:STO (0.5wt%) crystal surface exhibits the same properties as the STO film on Nb:STO. Deeper inside the Nb:STO crystal a n-type (metallic) conductivity can be observed.
The LRS of a STO/Nb:STO system can be regarded complete when the p-type STO and the p-type Nb:STO interface are both doped with oxygen vacancies ($V_O^{\cdot\cdot}$) and turned thereby into a ($n^+$) n-type system.

The resistive switching properties of $SrTiO_3$ were demonstrated by a reduced ($V_O^{\cdot\cdot}$ doped) STO single crystal. After doping the crystal with oxygen vacancies the crystal depicted a low resistance state compared with the pristine state. This low resistance state can be reversed into a high resistance state where a negative bias is applied. An attempt to explain this observation is shown in Figure 8-23.

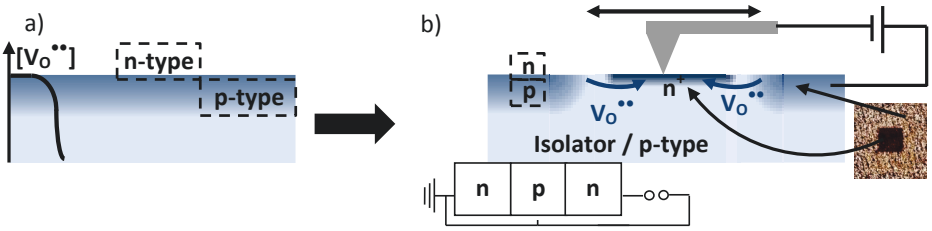


**Figure 8-23: a)** X-section of a STO single crystal doped with oxygen vacancies after annealing in vacuum. With $T_S$ = 800°C, $p_{O2} = 10^{-8}$mbar. **b)** Scanning with a negative AFM-tip bias which leads to a HRS.

The concentration of oxygen vacancies [$V_O^{\bullet\bullet}$] in the STO single crystal after annealing in vacuum increases towards the surface, see Figure 8-23 (a). In the very near surface region within the first few unit cells the concentration of $V_O^{\bullet\bullet}$ is extremely high and the oxide can therefore be regarded as n-type material. For low oxygen vacancy concentration the trapping of charge carriers from $h^{\bullet}$ dominate and therefore the STO demonstrates p-type character.
By applying a negative bias to the AFM-tip the positively charged oxygen vacancies are attracted to towards the tip. Thereby the concentration of oxygen vacancies in the vicinity of the tip is increased whereas the surrounding is depleted of oxygen vacancies. Thereby the connection between the $n^+$-type area and the counter electrode is interrupted by a isolating or p-type area. Thereby a HRS appears in the conductivity map.

The same principle is now applied to explain the resistive switching mechanism observed for STO films on Nb:STO.

***Pristine state***

The I(V) characteristic for the pristine state exhibits a Schottky diode-like rectifying behavior, see Figure 8-24 (a). The contact between the Nb:STO and the STO is considered as ohmic. With the forward direction for a negative polarization the STO exhibits p-type character. Due to the difference of the work functions between the AFM-tip and the oxide semiconductor the oxide requires electrons from the AFM-tip to sustain an equilibrated Fermi level. The electron concentration in the AFM-tip can be regarded as infinite and therefore doesn't exhibit a screening length. With the transfer of electrons into the oxide the concentration of holes in the oxide near the AFM-tip/oxide interface is depleted.
With the negative bias at the AFM-tip holes are attracted towards the junction and the depletion of holes is reduced which results in a reduced potential barrier in the forward direction and an increased net current. The potential barrier is increased for a positive bias to the AFM-tip.

The p-type behavior can be explained by charge carriers originating from holes $h^{\bullet}$ being trapped by acceptors / cation vacancies. The formation of holes can be due to the thermal oxidation reaction described above in a defect chemical reaction as shown in equation (8.1).
Both $V_O^{\bullet\bullet}$ and $h^{\bullet}$ act as donors whereas oxygen vacancies are near the conduction band and excited electrons are moved into the conduction band which is responsible for an n-type

conduction. Holes $h^{\bullet}$ on the other hand, can be found in the valence band and the corresponding electron is excited over the complete band gap $E_g$ to reach the conduction band. Deep laying acceptors such as $V_{Ti}^{''''}$ or $V_{Sr}^{''}$ could act as traps for the electron. By depleting the STO system of oxygen vacancies $V_O^{\bullet\bullet}$ the cation vacancies are then compensated by holes $h^{\bullet}$, see equation (8.1). This process introduces a p-type behavior of the STO film.

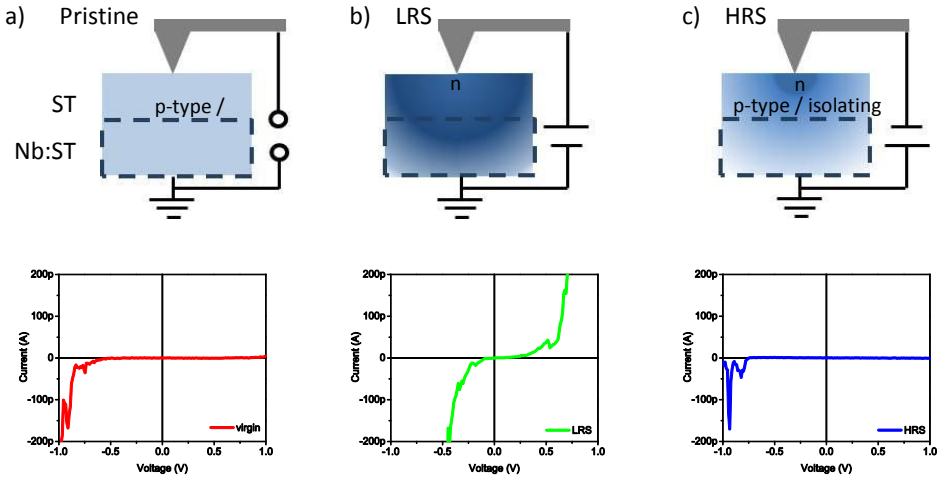


**Figure 8-24: a)** Pristine condition after deposition of STO on Nb:STO. **b)** SET-condition after positive bias to AFM-tip. **c)** RESET condition after negative bias to AFM-tip.

***SET-process & LR-state***

By applying a positive bias to the AFM-tip the positively charged oxygen vacancies are repelled by the electric field and oxygen ions ($O^{2-}$) with a negatively net charge are attracted towards the AFM-tip. Once the oxygen ions reach the surface the $O^{2-}$ ions are anodically oxidized by the positive AFM-tip and are thereby removed from the oxide, see the defect chemical equation (8.2) below.

$$O_O^x \leftrightarrow 2e^- + O_2(g) + V_O^{\cdot\cdot} \qquad (8.2)$$

In that way oxygen vacancies are incorporated in the surface region of the STO film and pushed by the electric field into the oxide, and the oxide gets chemically reduced. This process creates a high concentration of $V_O^{\bullet\bullet}$ in the STO surface region despite the drift of the oxygen vacancies away from the surface due to the electric field. Gas bubbles were observed by [103] beneath the electrode after a positive bias.

After the SET-process the system is in the low resistance state (LRS). The I(V) characteristics of the LRS are shown in Figure 8-12 and Figure 8-18 exhibit the same characteristics as the sputtered Nb:STO crystal, see Figure 8-25. When the n-type doping level of the semiconductor exceeds $10^{18}cm^{-3}$ the dominating conduction mechanism of a Schottky contact is via field emission. In the case of STO, the concentration of oxygen vacancies in the first few atomic

layers is extraordinarily high ($n^+$-type) due to the anodic oxidation process of oxygen ions and the associated implantation of oxygen vacancies, $V_O^{\cdot\cdot}$. This causes a very steep band bending that allows charge transfer via field emission which basically resembles an almost ohmic contact, which schematically shown in Figure 8-25. Due to the distribution of further oxygen vacancies in the STO film and the Nb:STO crystal (n-type bottom electrode) the I(V) curve basically resembles an almost ohmic characteristic.

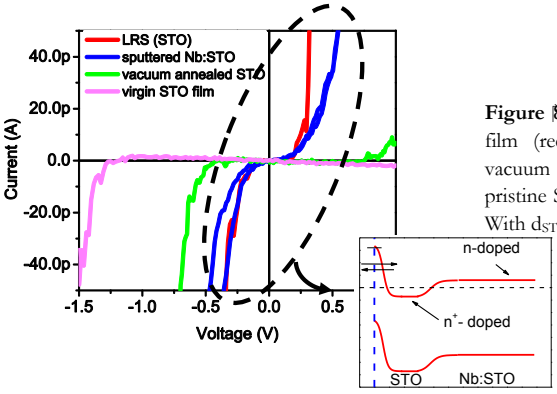


**Figure 8-25:** I(V) characteristics of a LRS of a STO film (red), a sputtered Nb:STO crystal (blue), a vacuum annealed STO film on Nb:STO (green), a pristine STO film after deposition on Nb:STO (pink). With $d_{STO}$ = 16u.c.

Figure 8-25 also demonstrates that the doping of STO by vacuum annealing is less effective than the anodic oxidation via the AFM-tip, compare green curve with the LRS (red). The conduction mechanism for the vacuum annealed STO film should be via thermionic-field emission which is typical for an n-type doping with $N_D \sim 10^{17}cm^{-3}$.
The pristine STO-film with p-type characteristic exhibits a conduction mechanism via thermionic emission which is typical for a doping concentration $<10^{17}cm^{-3}$.

***RESET-process & HR-state***

It was demonstrated above in Figure 8-5, Figure 8-7 and Figure 8-11 that the LRS can be reset into a HRS by applying a negative voltage to the AFM-tip. Due to the negative bias, oxygen vacancies are attracted. With this process the concentration of $V_O^{\cdot\cdot}$ in the oxide thin film is reduced giving the oxide its isolating or p-type character back, see Figure 8-24 (c). Therefore, only an accumulation of oxygen vacancies near the surface occurs giving it an $n^+$-type character. Because of the low oxygen vacancy concentration within the STO film it can be regarded as p-type or even isolating. This constitutes a $p^{(+)}n^{(+)}$junction which exhibits a (tunnel) diode-like rectifying behavior with the forward direction for a negative bias to the AFM-tip. The I(V) characteristics of the HRS also resemble the I(V) curve for the STO pn junction in [98].

## 8.2 STS analysis of resistive states in STO films and Nb:STO

The inscribed resistance states observed and described above give an idea about the quality of the resistance switching phenomenon in STO films. Because the resistance change requires the rearrangement of oxygen vacancies in the system it would be interesting to detect the

transformation of the local density of electronic states (LDOS) in the STO system. This would allow to conclude on the valence state of the system and the origin of the electrical characteristics.
Because the resistance state has to be inscribed into the STO first via LC-AFM the same AFM tip is utilized for the STS scans on the treated areas. Since such a LC-AFM tip with a tip radius ≥10nm is far from the atomic radius of a normal STM-tip the resulting tunneling currents are noisy and exhibit a wide statistical spread. Therefore quantitative results will be difficult to make but qualitative trends can be observed.

### 8.2.1 STS on STO thin films

For the STS analysis of STO films, two different films with varying stoichiometry were grown on Nb:STO. The parameters are listed in the table below.

| Parameter | Abrev. | Units | Sr-rich | Ti-rich |
|---|---|---|---|---|
| **Laser fluence** | $F_L$ | $J/cm^2$ | 0.8 | 2 |
| **Laser frequnce** | $f_L$ | Hz | 1 | |
| **Oxygen pressure** | $p_{O2}$ | mbar | 0.1 | |
| **Distance** | $D_{TS}$ | mm | 40 | |
| **Temperature** | $T_S$ | °C | 800 | |
| **Thickness** | $d_{STO}$ | u.c. | 2 | |

**Table 8-3:** PLD deposition parameters for the deposition of 2 STO films with different stoichiometry and $d_{STO}$ = 2u.c.

After deposition the films are cooled down to room temperature under the process pressure and then moved in-situ under UHV ($10^{-9}$mbar) to the SPM module. Subsequently, the resistance states were inscribed into the STO as described previously in chapter 8.1.4. These areas were then probed by the STS. Therefore the tip was moved to a specific spot and the voltage was swept from -3V to 3V and the tunneling currents recorded for a fixed distance of the AFM tip to the STO surface.

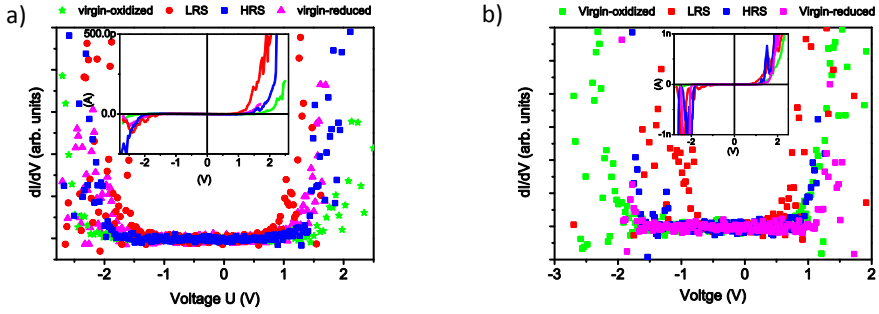


**Figure 8-26:** dI/dV – V curves of the pristine-oxidized state the LRS and HRS as well as the pristine-reduced state for different STO stoichiometries with $d_{STO}$ = 2u.c. **a)** Sr-rich STO, **b)** Ti-rich STO. The inset displays the I(V) curves of the tunnel current. With $V_{gap}$ = 2.8V.

Figure 8-29 presents the tunneling conductance with dI/dV vs. V for the two STO films. The insets show the tunneling currents. The up-turning points in positive and negative direction mark the conduction band maximum (CBM) and the valence band minimum (VBM) respectively. Figure (a) shows the dI/dV characteristics for a Sr-rich STO film (2u.c.). The band gap of the pristine oxidized state (0.1mbar $O_2$) is ~3eV which is close to the band gap of STO. The LRS depicts a smaller band gap (~2.4eV) with a small shift of the Fermi-level. The reduced (vacuum annealed) STO film depicts also a smaller band gap with ~2.7eV. The HRS resembles almost the pristine state with a band gap of ~2.9eV. For all 4 states no shift of the Fermi level is observed (shift of the dI/dV curve towards negative bias). In the case of the Sr-rich film the Fermi level is about 1.5eV below the CBM for the pristine state and 0.75eV below the CBM for the LRS.
The Ti-rich STO depicts a very similar behavior. The initial band gap of the Ti-rich is smaller with ~2.6eV compared with the expected band gap of 3.2eV. The LRS exhibits an extremely small band gap of ~1.3eV. The HRS also shows here a bigger band gap than the LRS with ~2.5eV. The Fermi level is at about 0.9eV below the CBM for the pristine state and about 0.5eV for the LRS.

### 8.2.2 STS on Nb:STO single crystal (0.5wt%)

Because it was demonstrated before in chapter 8.1.6 that Nb:STO also exhibits resistive switching properties different conditions of Nb:STO were investigated by STS.

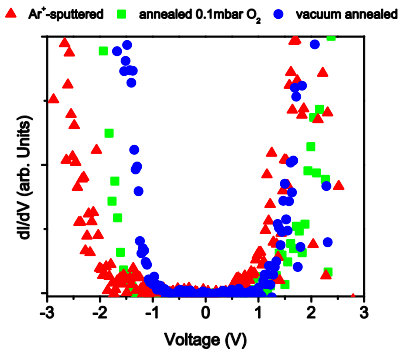


**Figure 8-27:** dI/dV – V curves for Nb:STO crystal (0.5wt%) and different conditions.

The dI/dV curve for a pristine Nb:STO surface after annealing in 0.1mbar $O_2$ ambient (T = 800°C) in Figure 8-27 reveals a band gap of ~2.7eV. After doping with oxygen vacancies in vacuum and T = 800°C the band gap of the crystal seem to be reduced to about 2.2eV. After sputtering, which was demonstrated before to cause a metallic surface the band gap is ~3eV and the Fermi level moved closer to the CBM.

### 8.2.3 Discussion

The transition of a transition-metal (TM) from insulting to conducting can be achieved by either band-gap closure and/or valence control, as described in [104]. The STS experiments show that the relocation of oxygen vacancies in the STO depict a change of the LDOS and indicate change of the band gap $E_g$. The LRS in both cases show a decrease of the band gap. Shrinkage of the band gap due to doping especially for high doping concentration with $N_D > 10^{18}cm^{-3}$ is possible due to an overlap of wavefunctions of the electrons from the dopants. This is because the average distance between the dopant-atoms decrease with concentration and is for $N_D = 10^{18}cm^{-3}$ about 10nm (25u.c. for STO). The shrinkage of the band gap $\Delta E_g$ can be determined with the following equation.

$$\Delta E_g(N) = -\frac{3q^2}{16\pi\varepsilon_S}\sqrt{\frac{q^2 N}{\varepsilon_S kT}} \qquad \textbf{(8-3)}$$

Where $q$ is the electronic charge of the dopant, $\varepsilon_S$ the dielectric constant of the material (which can also change with doping concentration). $N$ is the doping density and $k$ the Boltzmann constant and $T$ the temperature.

The STS measurements also reveal that the HRS area exhibits a bigger band gap than the LRS area. If the shrinkage of the band gap is due to a high doping concentration (oxygen vacancies) the increase of the band gap for a HRS area would indicate that the STO surface becomes oxidized or that the amount of oxygen vacancies is reduced after the reset process. The model proposed above in chapter 8.1.7 however, would argue for an even higher concentration of oxygen vacancies in the surface near region. This theory cannot be supported however by the STS measurements presented here.

Both films also show that the Fermi level shift with the doping by oxygen vacancies. For the LRS where the system contains a lot of oxygen vacancies the Fermi level is for both systems closer to the CBM than in the pristine or HRS. The fact the HRS shows almost the same distance of the Fermi level from the CBM than the pristine state, might be another hint that the theory of a high vacancy concentration near the STO surface for the HRS might be not totally correct.

## 8.3 In-situ chemical analysis of inscribed areas by PEEM (proof of concept)

For further analysis of the resistance states an additional technique is employed to study the effect of the resistive switching on the chemical properties of the STO film. The principle of the measurement was presented earlier in chapter 4.4. For the investigation of resistively switched areas with PEEM a STO film with 16u.c. was deposited onto Nb:STO (0.5wt%).

### 8.3.1 PEEM of inscribed areas

With in-situ LC-AFM technique, areas of LRS and HRS were inscribed into the surface of the STO film (8 x 8µm) and subsequently transferred to the PEEM under UHV atmosphere. PEEM is a surface sensitive technique where the emitted photoelectrons stem from a shallow interlayer of about 2 – 5nm into the material.

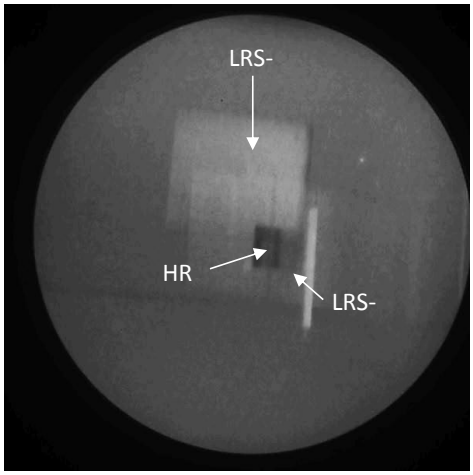


**Figure 8-28:** PEEM image of 2 resistively switched areas (overlapping). One with LRS only (LRS-I) and one with LRS and HRS area.

The PEEM image in Figure 8-28 shows that areas with different resistance states depict differences in their work functions. The LRS-I & LRS-II areas (bright) can be clearly distinguished from the HRS area (dark).

### 8.3.2 Discussion

The PEEM image clearly shows a work function contrast for switched areas. The variation of the work function could be explained by the shift of the Fermi level in the band gap due to doping with oxygen vacancies. For an n-type area ($V_O^{\cdot\cdot}$-doped) the Fermi level can be found according to [16] at ~0.21eV below the conduction band (CB) and it was shown in chapter 8.2.1 that for the LRS area the Fermi level is closer to the CBM than for the HRS or pristine state. This yields a work function of $\phi \sim 4.11$eV.

When the STO is depleted of oxygen vacancies it should exhibit a p-type behavior and the Fermi level moves back deeper into the band gap and could yield an average work function of $\phi \sim 6.11$eV. When the work function is small, more photoelectrons can be emitted. The bright field

in the PEEM image is therefore a clear indication of the smaller work function for the LRS area compared with the pristine or HRS area.
The fact that the HRS area appears darker than the LRS area in the PEEM image indicates that the Fermi level in the HRS area lays deeper within the band gap than for the LRS area. Because PEEM isn't necessarily a surface sensitive technique where only photoelectrons from the surface are collected the detected photoelectrons can also stem from below the surface where the STO area is depleted of $V_O^{\bullet\bullet}$ and the work function is higher.

## 8.4 Resistive switching dynamics

Because the resistive switching effect depends on the drift of $V_O^{\bullet\bullet}$ the dynamics of this process is of particular interest. To probe for the dynamics an electrical testing system (*Aixacct*) was attached to the AFM setup as described in chapter 4.5. With this system, voltage pulses in the micro- and nano-second regime can be applied. To probe for the SET and RESET dynamics a stoichiometric STO film was treated with SET and RESET pulses. With read-pulses the current resistance state of the system can be analyzed. The results are shown below.

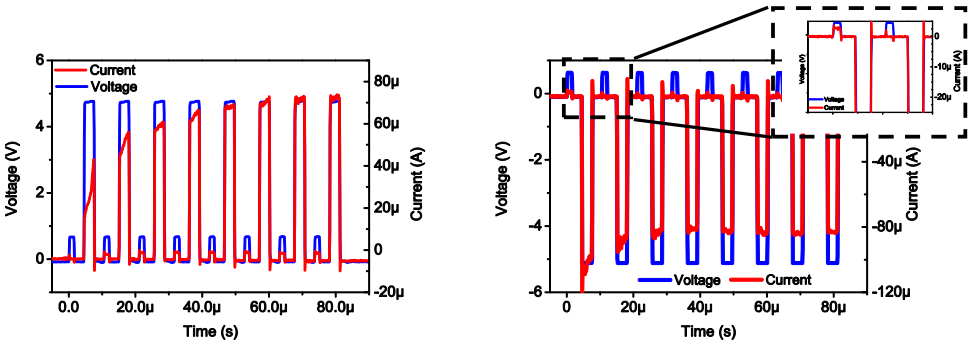


**Figure 8-29:** Current response of a STO film (20u.c.) on Nb:STO to short (3µs) voltage pulses contacted via a LC-AFM tip. **a)** SET-process. **b)** RESET-process

Figure 8-29 depicts the SET and RESET dynamics of a STO film ($d_{STO}$ = 20u.c.) with the applied SET-voltage pulses with $V_{SET}$ = +5V and $t_{SET}$ = 3µs (rise & fall time is set to 100ns). The read pulses in between the SET-pulses have an amplitude of $V_{READ}$ = +0.75V and $t_{READ}$ = 1.5µs. The delay between the READ and SET pulses is 2µs. The RESET-voltage pulses have the same characteristics with $V_{RESET}$ = -5V and $t_{RESET}$ = 3µs. The SET dynamics in Figure 8-29 (a) demonstrate the non-linear character of the system. The SET-current increases for each pulse. For the first 3 SET pulses the READ pulse shows an increase of the current. Although the current during the SET pulse increases further the current for the READ-pulse remains constant. After about 7 SET pulses the amount of $V_O^{\bullet\bullet}$ seems to reach a steady level. To create further oxygen vacancies a higher voltage is required.
The RESET process in Figure 8-29 (b) shows that the first READ pulse still exhibits a LRS with a current of ~2µA. After the first RESET pulse the read-out current is zero and therefore in a HRS. The current during the RESET pulse decreases in value until it saturates. This

demonstrates that the RESET process takes only one pulse whereas the SET process requires about 3 - 4 pulses to reach a steady state. This can be explained with equation (8.4) from [100] with L as the thickness of the oxide.

$$\tau_{write} \sim L/(\mu E) \qquad (8.4)$$

The electric field E is about the same for the first RESET pulse as for the first SET pulse. The mobility $\mu$ of the oxygen vacancies however, is different since it can be facilitated by joule heating. With $\mu_{RESET} > \mu_{SET}$ the write time $\tau_{write}$ is smaller for the RESET-process. Because of the additional joule heat during the pulse which facilitate the mobility of the oxygen vacancies. The saturation current during the RESET-pulse is essentially the current in forward direction of the Schottky diode-like pn-junction as demonstrated and explained in chapter 8.1 above.

## 8.5 Resistive Switching of MIM structures

For a real device the oxide will be eventually sandwiched in between two micro- or nano-structured electrodes. To test for the performance of the STO film in such a so called MIM (metal-isolator-metal) structure the STO film ($d_{STO}$ = 20nm) was deposited onto Nb:STO and Pt-electrodes with 10 x 10µm were sputtered on top. The MIM structure was then probed by contacting the Nb:STO and the top of the Pt-electrode.
After deposition the thin film were not quenched but cooled down slowly. The deposition of the top electrode was done ex-situ by sputtering.

### 8.5.1 I(V) characteristics of $SrTiO_3$ thin films

Since it was shown before in chapter XY that the stoichiometry and the defects in a STO film can be varied by the deposition parameters, three different STO films were deposited, namely, Sr-rich STO, stoichiometric STO and Ti-rich STO. The deposition parameters are shown below.

| Parameter | Abrev. | Units | Sr-rich | stoichiometric | Ti-rich |
|---|---|---|---|---|---|
| **Laser fluence** | $F_L$ | J/cm$^2$ | 0.9 | 1.4 | 2.2 |
| **Laser frequnce** | $f_L$ | Hz | | 5 | |
| **Oxygen pressure** | $p_{O2}$ | mbar | | 0.1 | |
| **Distance** | $D_{TS}$ | mm | | 44 | |
| **Temperature** | $T_S$ | ºC | | 800 | |
| **Thickness** | $d_{STO}$ | nm | | 20 | |

**Table 8-4:** PLD deposition parameters for the deposition of 3 STO films with different stoichiometry

After deposition of the STO film the top electrodes (Pt) were deposited to create a MIM structures which was subsequently probed for the pristine I(V) characteristics. Therefore, a small voltage (±0.5V) was applied by contacting the Pt-pad with a needle and the current response detected (*Keithley 2611A* Source Meter). The results are presented below.

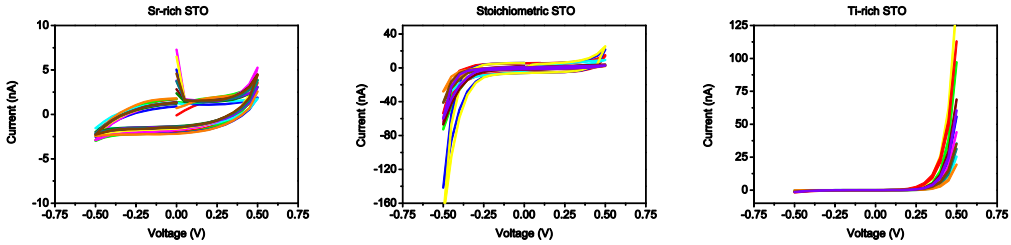


**Figure 8-30:** Pristine I(V) characteristics of a MIM structure, Pt / STO / Nb:STO with different stoichiometries of the STO film and Pt as the top electrode. **a)** Sr-rich STO film, **b)** Stoichiometric STO film, **c)** Ti-rich STO film. With $d_{STO}$ = 20nm. *Measurements performed by Chencheng Xu.*

In Figure 8-30 the pristine I(V) curves are shown for different MIM-pads for each stoichiometry. The STO films illustrate for every stoichiometry a different characteristic. The Sr-rich STO film (a) exhibits a very high resistance and seems very isolating. The stoichiometric STO film in (b) shows a rectifying behavior with forward direction for a negative bias to the top electrode. The Ti-rich STO film in (c) reveals also a rectifying behavior, however, with the forward direction for a positive bias to the top electrode.

Because the films are not equilibrated after deposition since the electrodes a applied by sputtering ex-situ the pristine states observed above are a result of the actual doping in the STO film and the contact with the sputtered top electrodes. After characterizing the pristine states the films were investigated for their RS properties.

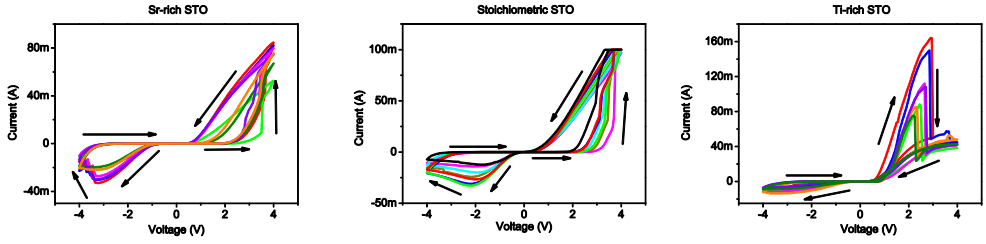


**Figure 8-31:** RS characteristics of MIM structures (Pt/STO/Nb:STO) for STO films with different stoichiometries. a) Sr-rich STO, b) stoichiometric STO, c) Ti-rich STO. With $V_{SET/RESET} = \pm 4V$. *Measurements performed by Chencheng Xu.*

The resistive switching performances of the STO films shown in Figure 8-31 show an 8-wise hysteresis loop for all the 3 different STO stoichiometries. Only the RS behavior of the Ti-rich STO film in (c) depicts a peculiarity. The I(V) response in the positive region shows a sudden drop of the current that resembles a so called uni-polar resistive switching nature which is characteristic for so called phase-change or thermo-chemical systems, but it could also be the onset of a filamentary type counter-8-wise switching.

The Sr-rich and stoichiometric system show similar results to the measurements presented in chapter 8.1 detected via LC-AFM. The currents are much higher than for the LC-AFM setup due to the increased contact area of the top electrodes (Pt). Both systems switch into the LRS for positive bias at ~3V and reset into the HRS for ~-3V with an obvious NDR characteristic.

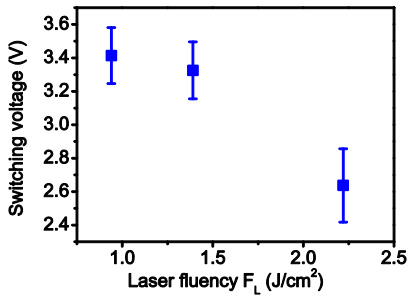


**Figure 8-32:** SET-voltage statistics for STO films with different stoichiometry.

The statistics of the resistance states for the MIM structures with different STO stoichiometries in Figure 8-33 reveal an immense variation of the resistance for the Sr-rich and the stoichiometric STO film.

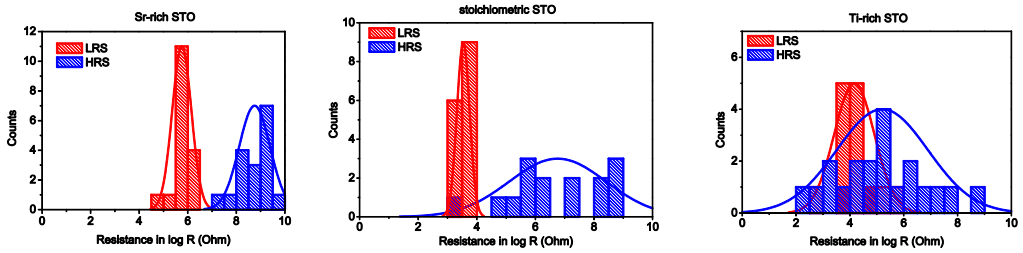


**Figure 8-33:** Statistics of the LRS and HRS values for different stoichiometries. **a)** Sr-rich STO with HRS/LRS ~1500, **b)** stoichiometric STO with HRS/LRS ~1800, **c)** Ti-rich STO with HRS/LRS ~11.

The stats also demonstrate that the HRS is less defined than the LRS and shows a bigger scatter compared with the LRS stats for all of the 3 different systems. Comparing all 3 of them, the Sr-rich STO film exhibits the best switching characteristics with the narrowest normal distribution of HRS and LRS.

### 8.5.2 I(V) characteristics of Fe:STO thin films

Fe doped STO was shown to change its defect composition with Fe concentration and laser fluence, see chapter 6. The effect of the defect composition on the RS properties is analyzed here. Therefore, two different Fe:STO films with 2wt% Fe are investigated for their I(V) characteristics, namely a film grown at a high laser fluence at 2.2J/cm$^2$, and at low fluence at 1.4J/cm$^2$.

| Parameter | Abrev. | Units | 1 | 2 |
|---|---|---|---|---|
| **Laser fluence** | $F_L$ | J/cm$^2$ | 1.4 | 2.2 |
| **Laser frequnce** | $f_L$ | Hz | 5 | |
| **Oxygen pressure** | $p_{O2}$ | mbar | 0.1 | |
| **Distance** | $D_{TS}$ | mm | 44 | |
| **Temperature** | $T_S$ | °C | 800 | |
| **Thickness** | $d_{Fe:STO}$ | nm | 20 | |

**Table 8-5:** PLD deposition parameters used for two different Fe:STO films (2wt%)

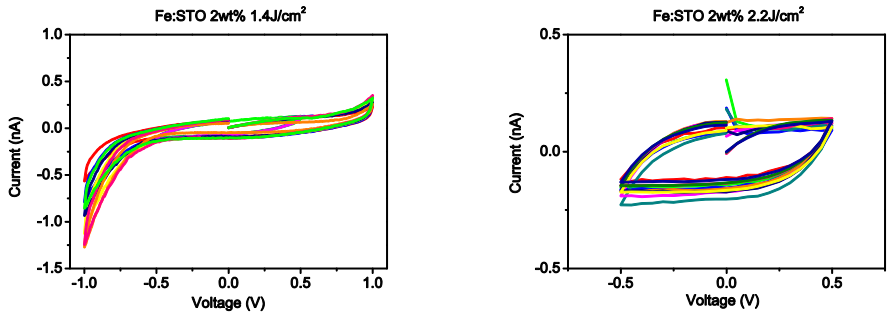


**Figure 8-34:** Pristine I(V) characteristics of Fe:STO (2wt%) films deposited at **a)** 1.4J/cm² and **b)** 2.2J/cm². *Measurements performed by Chencheng Xu.*

The Fe:STO films in Figure 8-34 show a highly insulting behavior with a p-type behavior for an increased negative bias, see figure (a). Despite the Fe-doping, the Fe:STO films depict a lower conductivity than the undoped stoichiometric STO film, see Figure 8-30.

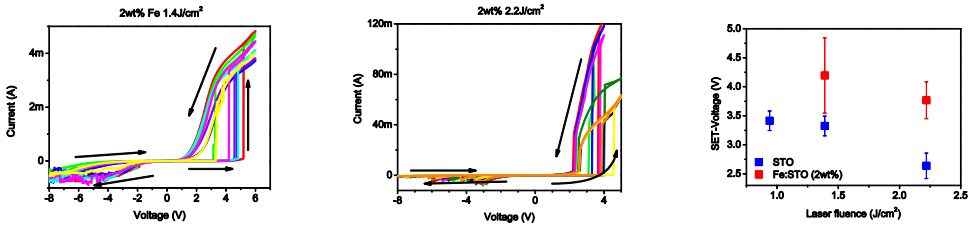


**Figure 8-35:** RS characteristics of MIM structures (Pt/Fe:STO/Nb:STO) for 2wt% Fe:STO deposited at different laser fluence. **a)** 1.4J/cm², **b)** 2.2J/cm², **c)** Set-voltage statistics. *Measurements performed by Chencheng Xu.*

The resistive switching characteristics are also slightly different compared with the un-doped films. Both Fe:STO films show in the plots in Figure 8-35 a very abrupt change from the pristine into the low resistance state upon a positive bias. By applying a negative bias the system switches back into the HRS with a very faint NDR characteristic. Both hysteresis loops show an 8-wise direction indicating that the system switches in the LRS by applying a positive voltage to the ion-blocking electrode. The SET-voltages are depicted in figure (c) and compared with the SET-voltages of the STO systems. The Fe:STO films need a higher bias to switch in to the LRS.

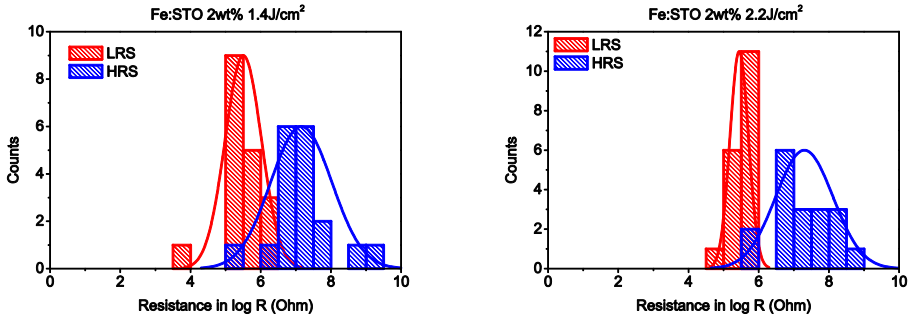


**Figure 8-36:** Statistics of the LRS and HRS values for Fe:STO films deposited at different laser fluence. **a)** 1.4J/cm² with HRS/LRS ~130, **b)** 2.2J/cm² with HRS/LRS ~130.

The switching statistics in Figure 8-36 show despite the abrupt switching characteristics a lower ratio of HRS/LRS than the un-doped STO films. Nevertheless, a clear resistive switching characteristic can be observed and the normal distribution of the resistance states better defined than the a stoichiometric or a Ti-rich STO film.

### 8.5.3 Discussion

The swift overview of the I(V) characteristics of the MIM structures with different stoichiometries of the active $SrTiO_3$ thin film demonstrates the impact of the stoichiometry and the defect structure respectively for the resistive switching phenomenon.

The pristine I(V) measurements reveal different rectifying behavior than detected by LC-AFM measurements. The reason for this deviation could be a consequence of the missing post annealing step, the ex-situ treatment of the specimen and the sputtering of the top electrode (Pt) on top of the STO film. Also the wetability of platinum to the oxides might affect the contact quality and therefore the pristine resistance which is due to the low affinity of Pt towards oxygen. All I(V) curves in Figure 8-30 suggest the existence of a Schottky diode-like contact between the oxide and the top electrode. The RS behavior of the STO films are similar to the loops detect via LC-AFM. The currents are much higher though due to the bigger contact area. In principle the same mechanisms as portrayed for the LC-AFM switched specimen can be applied to explain the observed switching characteristics of the MIM samples.

## 8.6 Discussion

It was demonstrated in these chapters that STO thin films could be successfully deposited for resistive switching investigations and transferred in-situ to various tools to study the RS mechanism. Via LC-AFM resistance states were effectively inscribed into the STO film without handling the specimen in ambient and subsequently transferred in-situ to further tools. Technologies like (LC)-AFM, STS or PEEM (XPS is theoretically possible as well but doesn't obtain the necessary spatial resolution) were successfully employed for examining the resistive switching characteristics.

It was shown that STO as well as Nb:STO (0.5wt%, bottom electrode) exhibits resistive switching properties. Also a STO single crystal could be resistively switched after doping with oxygen vacancies.

Basically all investigations the low resistance state (LRS) indicate a strongly n-type behavior arguing that oxygen vacancy incorporation reduces the resistance of the oxide and lowers the Schottky barrier of the top contact (AFM-tip/oxide film) which yields an almost ohmic behavior of the I(V) characteristic.

The interpretation of the high resistance state (HRS) is more controversial. The I(V) characteristics of the LC-AFM measurements demonstrate that the HRS and pristine state have the same properties. A diode like np contact, with the $n^+$-type doping near the surface due to enrichment of oxygen vacancies and a p or $p^+$-type doping within the oxide film due to a depletion of oxygen vacancies would be applicable to explain the I(V) characteristics. STS and PEEM measurements however would suggest a re-oxidation of the STO surface for the HRS, because the band gap and the work function seems to be increased compared with the LRS. Both observations would argue for a reduction of the oxygen vacancy concentration near the STO film surface after the reset process i.e. the HRS area in the case of inscribed resistance states. For a re-oxidation process of the thin film oxide however, the necessary oxygen gas is unfortunately missing in the UHV environment where the LC-AFM measurements were carried out. In the case of ex-situ measurements e.g. of MIM structures the oxygen could be taken either from the ambient or the oxygen is captured anyway in between the oxide and the electrode (which would cause a bad retention of the LRS since the oxygen would re-oxidize the LRS over time. Much better would be an oxygen storing conducting oxide as top electrode material with a big work function). It is possible however, that even in a UHV environment water molecules adsorbed on the specimen surface and AFM-tip could be used for a re-oxidation. By applying a negative bias to the AFM-tip the water splits into $H_2(g)$ and $OH^-$-ions at about 1.23V. The $OH^-$ can then be used for the re-oxidation process of the surface region.

Such a re-oxidation process would explain why there is a threshold for this process as shown in Figure 8-15 and why the HRS area also shows an increase of the resistance after a negative bias sweep.

Since the I(V) characteristics depicted a rectifying behavior with a forward direction for a negative bias to the top electrode, the oxidation process must then take place in the complete STO thin film. If only the interface gets oxidized (p-type) and the oxide beneath would keep its n-type character the rectifying characteristic would exhibit a forward direction for a positive bias.

This wasn't observed and therefore the complete oxide must be re-oxidized during the reset process.

Theoretically the re-oxidation process requires a change of the oxygen vacancy concentration from $10^{19}cm^{-3}$ to $\leq 10^{17}cm^{-3}$ to switch the system from the n-type to the p-type behavior. In the case of a doping concentration of $10^{19}cm^{-3}$ every $11^{th}$ unit cell misses an oxygen ion. By reducing the doping concentration to $10^{17}cm^{-3}$ only every $53^{rd}$ unit cell misses an oxygen ion.

Applying this "Gedanken-experiment" to a volume of 10x10x20nm (128unit cells) only 11.6 unit cells miss an oxygen ion considering a doping concentration of $10^{19}cm^{-3}$ (LRS). For a doping concentration of $10^{17}cm^{-3}$ only 2.4u.c. of the 128 unit cells are missing an oxygen ion (HRS). This basically means that only 9.2 oxygen ions have to be incorporated to switch the system from a LRS into a HRS within a volume of 128 unit cells.

The experiments also demonstrated that the stoichiometry of the STO impacts the RS characteristics but does not impact the resistive switching mechanism. All films exhibit an 8-wise hysteresis loop. A counter 8-wise switching mechanism wasn't observed. It is assumed however, that due the formation of a "plug" as a result of joule heating could lead to a counter 8-wise mechanism. The plug extends into the oxide film and forms the seed for a virtual cathode. By applying a negative voltage to the plug oxygen vacancies are attracted and accumulate and eventually reaching the counter electrode forming a LRS. By applying a positive bias the system can be reversed into the HRS.

This however would only possible for thicker films due to the spatial dimensions of the plug. If the oxide is too thin the plug might reach to the bottom contact and shorten the oxide.

# 9 Conclusions

As it was shown in the past that defects in complex oxides i.e. $SrTiO_3$, used for resistive switching systems or other applications, have a profound impact on the device performance; the intention of this work is to investigate how defects can be incorporated into $SrTiO_3$ thin films in a controlled manner by so-called defect engineering and what their impact on the resistive switching performance is.

## 9.1 Defect engineering

The defect engineering is approached by controlling the process parameters of the PLD deposition process of the STO thin film.

**$SrTiO_3$**

It was found that the STO thin film stoichiometry can be modified by the variation of the laser fluence. The STO thin film composition shifts from Sr-rich to stoichiometric to Ti-rich with increasing laser fluence which was determined by XPS investigations of the STO film.
The origin of this effect was revealed to be the result of preferential scattering of lighter plume species (Ti) during their time of flight (ToF) due to collisions with the background gas and of preferential ablation of Ti-species with increasing laser fluence. This was achieved by OES of the plume with fast plume imaging and XPS analysis of the ablation spot on the STO target.
For a low laser fluence the initial plume composition is basically stoichiometric with Ti/Sr ~ 1 which results in a Sr-rich film however, because Ti-species are scattered to larger angles during the ToF towards the substrate. This effect can be compensated by increasing the laser fluence which increases the Ti/Sr ratio > 1 in the plume and eventually yields a stoichiometric STO film. When the laser fluence is further increased a Ti-rich film is the consequence.

Because the STO film stoichiometry is a result of scattering process during ToF, the background gas pressure and the target substrate distance play a crucial role. By decreasing $p_{O2}$ the scattering can be reduced and finally suppressed for $p_{O2} < 10^{-3}$mbar. The longer $D_{TS}$ the more scattering effects take place. It was demonstrated that by keeping $f_L$ constant and varying $D_{TS}$ only, at $p_{O2}$ = 0.1mbar, the film stoichiometry can be shifted from Sr-rich for large $D_{TS}$ to stoichiometric to Ti-rich for small $D_{TS}$. The substrate temperature $T_S$ turned out to have effectively no effect on the STO film stoichiometry.

Non-stoichiometric STO films were shown to depict a lattice expansion, determined by XRD, which was attributed to the formation of cation vacancies accompanying the non-stoichiometry. The lattice expansion is due to Coulomb repulsion between the negatively charged cation vacancy and the surrounding oxygen ions ($O^{2-}$) [16] [31]. Therefore non-stoichiometric STO films show a reduction of the lattice expansion with the incorporation of oxygen vacancies ($V_O^{\bullet\bullet}$) as observed for reducing conditions.

Cation vacancies within the STO film were identified by PALS, but the concentration of cation vacancies couldn't be determined because the positron annihilation was in saturation, meaning that all implanted positrons were trapped at vacancies.
The measurement revealed that both cation vacancy types are prevalent in a STO film. It is concluded that the main cause of the lattice expansion is because of $V_{Sr}''$. The concentration of $V_{Ti}''''$ seems to be too low to come into effect; this is why a stoichiometric film, which obtains in general low vacancy concentration, shows therefore a very small or no lattice expansion.
More specifically it was found that the ratio of strontium vacancies ($V_{Sr}''$) to titanium vacancies ($V_{Ti}''''$) increases for a Ti-rich system. Remarkably the same trend was found for Sr-rich systems, which is attributed to the formation of Ruddlesden-Popper (RP) like phases for Sr-rich STO films which is the result of the overcompensation of the Ti-deficiency in the STO film. Due to the formation of such anti-phase boundaries, Sr-rich films depict extended defects due to stacking faults and also nano-voids that were identified by TEM and PALS.

**Fe-doped $SrTiO_3$**

All Fe doped STO films (Fe:STO) with $0.1 \leq$ Fe-wt% $\leq 10$ depict a lattice expansion that increases with the Fe concentration and is independent of a prevalent lattice expansion due to non-stoichiometric STO. Although the ablation rate decreases with Fe concentration the plume dynamics is only slightly affected and Fe doping basically does not impact the film stoichiometry as much as e.g. laser fluence variation does. PALS investigations revealed that Fe doped STO films basically contain $V_{Sr}''$ and $V_O^{\bullet\bullet}$. Titanium vacancies are essentially suppressed and practically not detectable. When the Fe concentration approaches 10wt%, areas with aggregated Fe seem to form, that were detected by TEM.
In general, the Fe:STO films turned out to depict a more complex defect structure than predicted by defect chemical considerations for bulk reactions.
All Fe-doped STO films depict defect-complexes where cation vacancies are connected to two or more oxygen vacandies, such as $V_{Sr}''$-п $V_O^{\bullet\bullet}$, which can yield extended defects and nono-voids.

## 9.2 Resistive switching properties

The resistive switching (RS) mechanism for $SrTiO_3$ is based on the rearrangement of oxygen vacancies and depends strongly on given arrangement of cation defects. To further elucidate the resistance change mechanism upon an external voltage bias to a STO system with various defects on the nano-scale, the STO films were investigated in-situ by local conductivity AFM (LC-AFM) and ex-situ by a MIM structure assembly.

**In-situ LC-AFM investigations**

For the in-situ investigations of the resistive switching properties, the specimen was transferred under UHV conditions to the UHV LC-AFM after deposition.
The STO films (16u.c. ~ 6.4nm) revealed an apparent p-type conduction mechanism in the I(V) diagram Figure 9-2, after quenching in oxidizing environment, which can be attributed to strontium vacancies ($V_{Sr}''$) in the STO system. The strontium vacancies act as acceptors and are

compensated by holes. By quenching the system in reducing environment the STO films were shown to become n-type doped which is evidence of oxygen vacancies $V_O^{\cdot\cdot}$ in the system.
The p-type state depicted a low conductivity whereas the n-type state a high conductivity. A transfer from HRS to LRS was also observed by applying a positive bias to the STO film via the AFM-tip and grounding the bottom electrode (Nb:STO substrate). The system was reset into a HRS by applying a negative potential to the AFM-tip.
Based on these observations a theory was devised where positively charged oxygen vacancies are driven into the p-type STO by applying a positive bias to the AFM-tip; and thereby converting the STO into an n-type conductor. By applying a negative potential, $V_O^{\cdot\cdot}$ are accumulated near the STO surface, leaving behind a $V_O^{\cdot\cdot}$ -depleted STO film, and turning it into a p-type conductor again.

The STO stoichiometry was demonstrated to affect the resistance switching properties, however without altering the mechanism in general. It was shown that Sr-rich STO films depict a distinct I(V) characteristic with a defined LRS and HRS state. However, inscribed resistance states appeared less stable as shown by LC-AFM measurement.
Ti-rich films showed less pronounced I(V) characteristics however with very stable inscribed resistance states which can be attributed to the absence of extended defects but the necessary profusion of point defects due to the non-stoichiometry. A non-stoichiometric system with a higher concentration of acceptors than a stoichiometric contains naturally more oxygen vacancies and hence, can cause a more pronounced resistance change when rearranged by an electric field.
Stoichiometric STO depicted RS properties that were weakly pronounced compared to Ti-rich and Sr-rich STO films and showed stable but more softly inscribed resistance states which can be the result of the low defect concentration in a stoichiometric STO film.

**MIM structures**

$SrTiO_3$ films (20nm) with a MIM structure were prepared by depositing a metal electrode (10x10µm) ex-situ on top of the oxide. STO films within this arrangement depicted the same switching polarity as the films investigated by LC-AFM. The pristine I(V) characteristics reveal different conduction mechanisms of the oxide for the different stoichiometries of the STO film which differ from the LC-AFM results, which is attributed to the deposition of the metal contact on top.
Sr-rich STO depicted a pristine p-type conduction mechanism whereas the stoichiomtric STO depicted a very insulting behavior initially. Ti-rich films show an initial n-type conductivity due to the high concentration of oxygen vacancies as shown in Figure 5-24.
The RS properties were best for the initial p-type film and rather poorly defined for the initial n-type films. Therefore it is concluded that it is essential for a RS system to depict an initial p-type conductivity with a fair mobility for oxygen vacancies to be turned subsequently into a n-type conductor. The better this transformation can be defined the better are the RS properties.

## Concluding remarks with outlook

The controlled accommodation of point defects in $SrTiO_3$ via PLD was essentially achieved and the role of the PLD process parameters for point defects revealed.
Further investigations by PALS are necessary however, to further elucidate the actual concentration of cation vacancies in the STO films. Such analysis would provide the necessary conclusions to explain the zero-lattice expansion of a stoichiometric STO film although both types of cation vacancies were found to be present in the oxide.

Even though differences in the resistive switching behavior for films with different point defects were found, their role for the RS effect couldn't be specified.
The findings from the LC-AFM studies helped to device a theory where a conversion from p- to n-type is responsible for the resistance change which is achieved by the relocation of oxygen vacancies within the STO film. However, the the p-type condition in the STO system couldn't be disambiguously proofed and the consequential band formations in the thin oxide layer (~10nm) explicated. Therefore further investigations regarding the p-type STO have to be done as well as band bending scenarios in thin oxide films devised. This theory has to be further refined by simulation within a drift diffusion model.

# Bibliography


[1] T. Ohnishi, K. Shibuya, T. Yamamoto, and M. Lippmaa, Defects and transport in complex oxide thin films, *J. Appl. Phys.* **103**, 103703/1-6 (2008)

[2] T. Ohnishi, M. Lippmaa, T. Yamamoto, S. Meguro, and H. Koinuma, Improved stoichiometry and misfit control in perovskite thin film formation at a critical fluence by pulsed laser deposition, *Appl. Phys. Lett.* **87**, 241919/1-3 (2005)

[3] S. McGuire, D. J. Keeble, r. E. Mason, P. G. Coleman, Y. Koutsonas, and T. j. Jackson, Variable energy positron beam analysis of vacancy cluster defectrs in laser ablated STO thin films on STO, *J. Appl. Phys.* **100** (2006)

[4] A. Uedono, K. Shimayama, M. Kiyohara, Z. Q. Chen, and K. Yamabe, Study of oxygen vacancies in SrTiO3 by positron annihilation, *J. Appl. Phys.* **92** (2002)

[5] E. Breckenfeld, R. Wilson, J. Karthik, A. R. Damodaran, D. G. Cahill, and L. W. Martin, Effect of Growth Induced (Non)Stoichiometry on the Structure, Dielectric Response, and Thermal Conductivity of SrTiO3 Thin Films, *Chem. Mater.* **24**, 331-337 (2012)

[6] J. Son, P. Moetakef, B. Jalan, O. Bierwagen, N. J. Wright, R. Engel-Herbert, and S. Stemmer, Epitaxial SrTiO3 films with electron mobilities exceeding 30,000 cm(2) V-1 s(-1), *Nat. Mater.* **9**, 482-484 (2010)

[7] Y. Kozuka, Y. Hikita, C. Bell, and H. Y. Hwang, Dramatic mobility enhancements in doped SrTiO3 thin films by defect management, *Appl. Phys. Lett.* **97**, 12107/1-3 (2010)

[8] R. Waser, R. Dittmann, M. Salinga, and M. Wuttig, Function by defects at the atomic scale - New concepts for non-volatile memories, *Solid-State Electron.* **54**, 830-840 (2010)

[9] R. Waser, R. Dittmann, M. Salinga, and M. Wuttig, The role of defects in resistively switching chalcogenides, *Int. J. Mat. Res.* **101**, 182-198 (2010)

[10] K. Shibuya, R. Dittmann, S. Mi, and R. Waser, Impact of defect distribution on resistive switching characteristics of $Sr_2TiO_4$ thin films, *Adv. Mater.* **22**, 411-414 (2010)

[11] R. D. Leapman, L. A. Grunes, and P. L. Fejes, Study of the L23 edges in the 3d transition metals and their oxides by electron-energy-loss spectroscopy with comparisons to theory, *Phys. Rev. B: Condens. Matter* **26**, 614 (1982)

[12] D. M. Smyth, *The defect chemistry of metal oxides*, Oxford University Press (2000)

[13] F. A. Kroeger and H. J. Vink, Relations between the concentrations of imperfections in crystalline solids, *Solid State Physics* **3**, 307 - 435 (1956)

[14] F. A. Kroeger and H. J. Vink, Relations between the concentrations of imperfections in solids, *Journal of the Physics and Chemistry of Solids, UK* **5**, 208-223 (1958)

[15] A. B. Lidiard, Ionic Conductivity, *Springer Verlag* **20**, 246-275 (1957)

[16] Tomohito Tanaka, Katsuyuki Matsunaga, Yuichi Ikuhara, Takahisa Yamamoto, First-principles study on structures and energetics of intrinsic vacancies in SrTiO3, *PHYSICAL REVIEW B* (2003)

[17] R. Moos and K. H. Haerdtl, Defect Chemistry of Donor-Doped and Undoped Strontium Titanate Ceramics between 1000° and 1400°C, *J. Am. Ceram. Soc.* **80**, 2549-62 (1997)

[18] N. H. Chan and D. M. Smyth, Defect chemistry of $BaTiO_3$, *J. Electrochem. Soc.* **123**, 1584-5 (1976)

[19] Paul C. McIntyre, Equilibrium Point Defect and Electronic Carrier Distributions near Interfaces in Acceptor-Doped Strontium Titanate, *J. Am. Ceram. Soc.* (2000)

[20] Rotraut Merkle, Joachim Maier, How Is Oxygen Incorporated into Oxides? A Comprehensive Kinetic Study of a Simple Solid-State Reaction with SrTiO3 as a Model Material, *Angew. Chem. Int. Ed.* (2008)

[21] U. Balachandran and N. G. Eror, Electrical conductivity in strontium titanate, *J. Solid State Chem.* **39**, 351 - 359 (1981)

[22] Felix Gunkel, The role of defects at functional interfaces between polar and non-polar perovskite oxides (2013)

[23] P. Lupetin, Charge carrier defect chemistry of nanoscopic SrTiO3 (2012)

[24] I. Denk, W. Munch, and J. Maier, Partial conductivities in $SrTiO_3$: bulk polarization experiments, oxygen concentration cell measurements, and defect-chemical modeling, *J. Am. Ceram. Soc.* **78**, 3265-72 (1995)

[25] W. Luo, W. Duan, S. G. Louie, and M. L. Cohen, Structural and electronic properties of n-doped and p-doped SrTiO3, *Phys. Rev. B* **70**, 214109 (2004)

[26] Avner Rothschild, Wolfgang Menesklou, Harry L. Tuller, and Ellen Ivers-Tiffe, Electronic Structure, Defect Chemistry, and Transport Properties of SrTi1-xFexO3-y Solid Solutions, *Chem. Mater.* (2006)

[27] X. G. Guo, X. S. Chen, Y. L. Sun, L. Z. Sun, X. H. Zhou, and W. Lu, Electronic band structure of Nb doped SrTiO3 from first principles calculation, *Phys. Lett. A* **317**, 501-506 (2003)

[28] J. Maier, S. Prill, and B. Reichert, Space charge effects in polycrystalline, micropolycrystalline and thin film samples: Application to AgCl and AgBr, *Solid State Ionics* **28 - 30**, 1465 - 1469 (1988)

[29] R. A. DeSouza, The formation of equilibrium space-charge zones at grain boundaries in the perovskite oxide SrTiO3, *Physical Chemistry Chemical Physics* **11**, 9939 - 9969 (2009)

[30] E. Ertekin, V. Srinivasan, J. Ravichandran, P. B. Rossen, W. Siemons, A. Majumdar, R. R. Ramesh, and J. C. Grossman, Interplay bewtween intrinsic defects, doping, and free carrier concentration in SrTiO3 thin films, *Phys. Rev. B: Condens. Matter* **85** (2012)

[31] Daniel A. Freedman, d. roundy, and T. A Arias, Elastic effects of vacancies in strontium titanate: Short- and long-range strain fields, elastic dipole tensors, and chemical strain, *Phys. Rev. B: Condens. Matter* **80** (2009)

[32] T. Suzuki, Y. Nishi, and M. Fujimoto, Defect structure in homoepitaxial non-stoichiometric strontium titanate thin films, *Philos. Mag. A-Phys. Condens. Matter Struct. Defec* **80**, 621-637 (2000)

[33] R. Evarestov, E. Blokhin, D. Gryaznov, E. A. Kotomin, R. Merkle, and J. Maier, Jahn-Teller effect in the phonon properties of defective SrTiO3 from first principles, *Phys. Rev. B: Condens. Matter* **85** (2012)

[34] V. M. Goldschmidt, *Geochemistry*, Oxford University Press (1958)

[35] S. N. Ruddlesden and P. Popper, The compound Sr3Ti2O7 and its structure, *Acta Crystallographica* **11**, 54-55 (1958)

[36] C. Noguera, Theoretical investigation of the Ruddlesden-Popper compouns Srn+1TinO3n+1 (n = 1 - 3), *Philosophical Magazine Letters* **80**, 173 - 180 (2000)

[37] ITRS, The International Technology Roadmap for Semiconductors - ITRS 2011 Edition (2011)

[38] R. Waser, R. Dittmann, G. Staikov, and K. Szot, Redox-Based Resistive Switching Memories - Nanoionic Mechanisms, Prospects, and Challenges, *Adv. Mater.* **21**, 2632-2663 (2009)

[39] M. Hasan, R. Dong, D. S. Lee, D. J. Seong, H. J. Choi, M. B. Pyun, and H. Hwang, A Materials Approach to Resistive Switching Memory Oxides, *Journal of Semiconductor Technology and Science* **8** (2008)

[40] R. Muenstermann, T. Menke, R. Dittmann, and R. Waser, Coexistence of Filamentary and Homogeneous Resistive Switching in Fe-doped $SrTiO_3$ Thin-Film Memristive Devices, *Adv. Mat.* **22**, 4819 (2010)

[41] D. B. Chrisey and G. K. Hubler, *Pulsed Laser Deposition of Thin Films*, John Wiley & Sons, Inc. (1994)

[42] G. J. H. M. Rijnders, G. Koster, D. H. A. Blank, and H. Rogalla, In situ monitoring during pulsed laser deposition of complex oxides using reflection high energy electron diffraction under high oxygen pressure, *Appl. Phys. Lett.* **70**, 1888-1890 (1997)

[43] Ayahiko Ichimiya and Philip I. Cohen, Reflection high Energy Electron Diffraction, *Cambridge University Press* (2004)

[44] X. D. Zhu, Y. Y. Fei, X. Wang, H. B. Lu, and G. Z. Yang, General theory of optical reflection from a thin film on a solid and its application to heteroepitaxy, *Phys. Rev. B: Condens. Matter* **75** (2007)

[45] X. Wang, K. Jin, H. Lu, Y. Fei, X. Zhu, G. Yang, and, Movement of oxygen vacancies in oxide film during annealing observed by an optical reflectivity difference technique, *Appl. Phys. Lett.* **102** (2007)

[46] X. D. Zhu, H. b. Lu, G. Z. Yang, A. Y. Li, B. Y. Gu, and D. Z. Zhang, Epitaxial growth of SrTiO3 on SrTiO3 (001) using an oblique-incidence reflectance-diffrerence technique, *Phys. Rev. B: Condens. Matter* **57** (1998)

[47] S. Amoruso, R. Bruzzese, N. Spinelli, and R. Velotta, Characterization of laser-ablation plasmas, *J. Phys. B Atom. Mol. Opt. Phys.* **32**, R131-R172 (1999)

[48] I. Anisimov and B. S. Luk'yanchuk, Selected problems of laser ablation theory, *Uspekhi Fizicheskikh Nauk* **172**, 301 - 333 (2002)

[49] Guus Rijnders, The initial growth of complex oxides, *Ph.D. Thesis* (2001)

[50] G. Eres, J. Z. Tischler, C. m. Rouleau, P. Zschack, H. m. Christen, and B. C. Larson, Quantitative determination of energy enhanced interalyer transport in pulsed laser deposition of SrTiO3, *Phys. Rev. B: Condens. Matter* **84** (2011)

[51] S. Stoyanov and M. Michailov, Non-steady state effects in MBE: oscillations of the step density at the crystal surface, *Surface Science* **202**, 109 - 124 (1988)

[52] D. M. Holmes, J. L. Sudijono, C. F. McConville, T. S. Jones, and B. A. Joyce, Direct evidence for the step density model in the initial stages of the layer-by-layer homoeptaxial growth of GaAs, *Surface Science Letters* **370** (1997)

[53] A. Sambri, S. Amoruso, X. Wang, F. Miletto Granozio, and R Bruzzese, Plume propagation dynamics of complex oxides in oxygen, *J. Appl. Phys.* **104** (2008)

[54] A. Sambri, S. Amoruso, X. Wang, M. Radovic, F. Miletto Granozio, and R. Bruzzese, Substrate heating influence on plume propagation during pulsed laser deposition of complex oxides, *Appl. Phys. Lett.* **91** (2007)

[55] S. Amoruso, j. Schou, and J. G. Lunney, Multiple-scattering effects in laser ablation plume propagation in gases, *Europhys. Lett.* **76**, 436 - 442 (2006)

[56] F. Sanchez-Bajo and F. L. Cumbrera, The use of the Pseudo-Voigt function in the variance method of X-ray line-broadening analysis, *Journal of Applied Crytallography* **30**, 427 - 430 (1997)

[57] R. Krause-Rehberg and H. S. Leipner, *Positron Annihilation in Semiconductors*, Springer (1999)

[58] R. A. Mackie, S. Singh, J. Laverock, B. Dugdale, and D. J. Keeble, Vacancy defect positron lifetimes in strontium titanate, *Phys. Rev. B: Condens. Matter* **79** (2009)

[59] D. J. Keeble, R. A. Mackie, W. Egger, B. Loewe, P. Pikart, C. Hugenschmidt, and T. J. Jackson, Identification of vacancy defects in a thin film perovskite oxide, *Physical Review B* **81**, 64102/1- (2010)

[60] A. Gentils, O. Copie, G. Herranz, F. Fortuna, M. Bibes, K. Bouzehouane, E. Jacquet, C. Carretero, M. Basletic, E. Tafra, A. Hamzic, and A. Barthelemy, Point defect distribution in high-mobility conductive SrTiO3 crystals, *Phys. Rev. B* **81**, 144109/1-9 (2010)

[61] Henning Bubert and Holger Jenett, *Surface and Thin Film Analysis*, Wiley VCH (2003)

[62] C. M. Brooks, L. F. Kourkoutis, T. Heeg, J. Schubert, D. A. Muller, and D. G. Schlom, Growth of homoepitaxial SrTiO3 thin films by molecular-beam epitaxy, *Appl. Phys. Lett.* **94**, 162905/1-3 (2009)

[63] B. Jalan, P. Moetakef, and S. Stemmer, Molecular beam epitaxy of SrTiO3 with a grwoth window, *Appl. Phys. Lett.* **95** (2009)

[64] HISAO YAMADA, G. R. MILLER, Point Defects in Reduced Strontium Titanate, *J. Solid State Chem.* (1973)

[65] B. Dam, J. H. Rector, J. Johansson, J. Hujibregtse, and D.G. De Groot, Mechanism of incongruent ablation of STO, *J. Appl. Phys.* **83**, 3386 - 3389 (1998)

[66] B. Dam, J.H. Rector, J. Johansson, S. Kars, and R. Griessen, Stoichiometric transfer of complex oxides by pulsed laser deposition, *Appl. Surf. Sci.* **96-98**, 679-684 (1996)

[67] C. R. A. Catlow, Z. X. Guo, M. Miskufova, S. A. Shevlin, A. G. H. Smith, A. A. Sokol, A. Walsh, D. j. Wilson, and S. M. Woodley, Advances in computational studies of energy materials, *Philosophical Transactions of the Royal Society* **368**, 3379 - 3456 (2010)

[68] N.-H. Chan, R. K. Sharma, D. M. Smyth, Non-stoichiometry in SrTiO3, *J. EIectrochem. Soc.*, 1762 (1981)

[69] D. J. Keeble, B. Jalaa, L. Ravelli, W. Egger, and G. Kanda, Suppression of vacancy defects in epitaxial La-doped SrTiO3 films, *Appl. Phys. Lett.* **99** (2011)

[70] M. Hakala, M. J. Puska, and R. M. Nieminen, Momentum distributions of electron-positiron pairs annihilating at vacancy clusters in Si, *Phys. Rev. B: Condens. Matter* **57** (1998)

[71] R. Meyer, Modellierung transienter Vorgänge in donatordotiertem Strontiumtitanat, *PhD Thesis RWTH Aachen* (2001)

[72] T. T. Itina, W. Marine, and M. Autric, Monte Carlo simulation of pulsed laser ablation from two-component target into diluted ambient gas, *J. Appl. Phys.* **82** (1997)

[73] A. N. Khodan, S. Guyard, J.-P. Contour, D.-G. Crete, E. Jacquet, and K. Bouzehouane, Pulsed laser deposition of epitaxial SrTiO3 films: Growth, structure and functional properties, *Thin Solid Films* **515**, 6422 - 6432 (2007)

[74] R. F. Wood, K. R. Chen, J. N. Leboeuf, A. A. Puretzky, and D. B. Geohegan, Dynamics of Plume Propagation and Splitting during Pulsed Laser Ablation, *Phys. Rev. B: Condens. Matter* **79** (1997)

[75] S. Amoruso, A. Sambri, and X. Wang, Plume expansion dynamics during laser ablation of manganates in oxygen atmposphere, *Appl. Surf. Sci.* **253**, 7696 - 7701 (2007)

[76] K. Shimoyama, M. Kiyohara, A. Uedono, and K. Yamabe, Homoepitaxial Growth of SrTiO3 in an Ultrahigh Vacuum with Automatic Feeding of Oxygen form Substrate at Temperatures as Low as 370C, *Jpn. J. Appl. Phys.* **41**, 269 - 271 (2002)

[77] G. Z. Liu, Q. Y. Lei, and X. X. Xi, Stoichiometry of SrTiO3 films grown by pulsed laser deposition, *Appl. Phys. Lett.* **100** (2012)

[78] F. Gunkel, S. Hoffmann-Eifert, R. Dittmann, S.B. Mi, C.L. Jia, P. Meuffels, and R. Waser, High temperature conductance characteristics of LaAlO3/SrTiO3-heterostructures under equilibrium oxygen atmospheres, *Appl. Phys. Lett.* **97**, 12103/1-3 (2010)

[79] M. L. Scullin, J. Ravichandran, C. Yu, M. Huijben, J. Seidel, A. Majumdar, and R. Ramesh, Pulsed laser deposition-induced reduction of SrTiO3 crystals, *Acta Mater.* **58**, 457 - 463 (2010)

[80] X. D. Zhu, Weidong Si, X. X. Xi, and Qidu Jiang, Oxidation kinetics in SrTiO3 homoepitaxy on SrTiO3 (001), *Appl. Phys. Lett.* **78** (2001)

[81] R. Meyer, R. Waser, J. Helmbold, and G. Borchardt, Observation of vacancy defect migration in the cation sublattice of complex oxides by $^{18}O$ tracer experiments, *Phys. Rev. Lett.* **90**, 105901/1-4 (2003)

[82] R. A. De Souza, The formation of equilibrium space-charge zones at grain boundaries in the perovskite oxide SrTiO3, *Phys. Chem. Chem. Phys.* **11**, 9939-9969 (2009)

[83] D. Walton, Nucleation of Vapor Deposits, *J. Chem. Phys.* **37** (1962)

[84] S. Amoruso, A. Sambri, and X. Wang, Propagation dynamics of a LaMnO3 laser ablation plume in an oxygen atmosphere, *J. Appl. Phys.* **100** (2006)

[85] T. Menke, Investigation of the electroforming and resistive switching mechanisms in Fe-doped $SrTiO_3$ thin films (2010)

[86] Ch. Lenser, A. Kuzmin, J. Purans, A. Kalinko, R. Waser, and R. Dittmann, Probing the oxygen vacancy distribution in resistive switching Fe-SrTiO3 metal-insulator-metal-structures by micro-x ray absorption near-edge structure, *J. Appl. Phys.* **111**, 76101/1-3 (2012)

[87] X. Zhou, J. Shi, and C. Li, Effect of Metal doping on electronic structure and visible light absorption of SrTiO3 and NaTaO3 (Metal = Mn, Fe, Co), *The Journal of Physical Chemistry C* **115**, 8305 - 8311 (2011)

[88] H. Schroeder, Stress- and electromigration-induced voiding and its correlation to macroscopic stress changes [IC interconnects], *Warrendale, PA, USA: Mater. Res. Soc*, 237-48 (1998)

[89] Harald Brune, Karsten Bromann, Holger Roder, and Klaus Kern, Effect of strain on surface diffusion and nucleation, *Phys. Rev. B: Condens. Matter* **52** (1995)

[90] T. Hoshino, M. Hata, and M. Tsuda, Migration of Si adatom on strained Si(1 1 1) surfaces, *Surface Science* **481**, 205-214 (2001)

[91] E. J. Tarsa, E. A. Hachfeld, F. T. Quinlan, J. S. Speck, and M. Eddy, Growth-related stress and surface morphology in homoepitaxial SrTiO3 films, *J. Appl. Phys.* **68** (1996)

[92] P.R. Willmott, R. Herger, C.M. Schlepuetz, D. Martoccia, and B.D. Patterson, Energetic Surface Smoothing of Complex Metal-Oxide Thin Films, *Phys. Rev. Lett.* **96** (2006)

[93] K. Szot, R. Dittmann, W. Speier, and R. Waser, Nanoscale resistive switching in $SrTiO_3$ thin films, *Phys. Status Solidi-Rapid Res. Lett.* **1**, R86-R88 (2007)

[94] J. Robertson and C. W. Chen, Schottky barrier heights of tantalum oxide, barium strontium titanate, lead titanate, and strontium bismuth tantalate, *Appl. Phys. Lett.* **74**, 1168-70 (1999)

[95] S. M. Sze and Kwok K. Ng, *Physics Of Semiconductor Devices*, Wiley (2007)

[96] Shriram Ramanathan, *Thin film Metal-Oxides*, Springer (2010)

[97] T. Higuchi, T. Tsukamoto, N. Sata, M. Ishigame, Y. Tezuka, and S. Shin, Electronic structure of p-type SrTiO3 by photoemission spectroscopy, *Phys. Rev. B: Condens. Matter* **57** (1998)

[98] Q. L. Zhou, K.J. Jin, H.B. Lu, P. Han, Z.H. Chen, K. Zhao, Y.L. Zhou, and G.Z. Yang, Transport property in SrTiO3 p-n junction, *Europhys. Lett.* **71**, 283 - 289 (2005)

[99] L.O. Chua and S.M. Kang, Memristive devices and systems, *Proc. IEEE* **64**, 209-223 (1976)

[100] D. B. Strukov and R. S. Williams, Exponential ionic drift: fast switching and low volatility of thin-film memristors, *Appl. Phys. A-Mater. Sci. Process.* **94**, 515-519 (2009)

[101] A. S. Alexandrov, A. M. Bratkovsky, B. Bridle, S. E. Savel'ev, D. B. Strukov, and R. S. Williams, Current-controlled negative differential resistance due to Joule heating in $TiO_2$, *Appl. Phys. Lett.* **99**, 202104-3 (2011)

[102] J. Lee, E. M. Bourim, D. Shin, J. S. Lee, D. j. Seong, J. Park, W. Lee, M. Chang, S. Jung, J. Shin, and H. Hwang, Analysis of interface switching for Nb doped SrTiO(3) single crystal device using complex impedance spectroscopy, *Curr. Appl. Phys.* **10**, E68-E70 (2010)

[103] J. J. Yang, F. Miao, M. D. Pickett, D. A. A. Ohlberg, D.R. Stewart, C. N. Lau, and R. S. Williams, The mechanism of electroforming of metal oxide memristive switches, *Nanotechnology* **20**, 215201 (2009)

[104] A. Fujimori, Electronic structure of metallic oxides: Bang-gap closure and valence control, *J. Phys. Chem. Sol.* **53**, 1595 - 1602 (1992)

# Acknowledgments

At last I would like to thank and express my respect to the people who supported and helped me to accomplish this work.

I would like to express my great gratitude to Prof. Dr. Franz Faupel for taking me on as his Ph.D. student regardless of the hurdles involved. I am truly thankful and appreciate his trust. I also want to give special thanks to Prof. Dr. Regina Dittmann and Prof. Dr. Rainer Waser for giving me the chance to work at the Peter-Grünberg-Institute and their trust with the installation and operation of the oxide-cluster system. Regina as my supervisor provided me with scientific guidance and made international collaborations possible to broaden my scope of work and understanding.

This leads me to say thank you to Prof. Dr. David Keeble (University of Dundee, Scotland) and Dr. Alessia Sambri and Prof. Dr. Salvatore Amorusso (University of Naples, Italy) for their extremely productive collaborations and fruitful contributions to my research.

Daily research and work would not have been possible without the support and help from Georg Pickartz and Marcel Gerst who were there to install and maintain scientific machinery and solve daunting technical issues. Moreover I would like to pay my respect to Rainer Bruchhaus, Rene Borowski, and Tobias Menke who helped me to keep my sanity when research appeared disheartening and showed me that there is more to life than work.

Special thanks also go to my dear Ph.D. colleagues who made this work not only fun but also engaged in helpful discussions and were true friends. Thank you Anja, Anne, Katharina, Ninet, Alex, Chencheng, Christian, Christoph, Florian, Marcel and Thomas.

A special hug goes to Felix Gunkel and Paul Meuffels who are great friends and were great colleagues and were there throughout.

Finally I want to thank my family for their understanding and support throughout all the years of this endeavor:
My understanding wife, Rebecca, who relentlessly endured the burden of a long-distance relationship and short weekends. My parents Martin and Gabriele and sisters Anna and Lisa who made the home visits warm and loving. My parents-in-law Bob, Laura and Carleen for their support and understanding keeping their daughter abroad for such a long time. A special thanks goes to my best man Alex who supported me every step of the way and beyond.

Thank you to every one of you!

Sebastian

Band / Volume 21
**Optical and electrical addressing in molecule-based logic circuits**
M. Manheller (2012), XIV, 183 pp
ISBN: 978-3-89336-810-5

Band / Volume 22
**Fabrication of Nanogaps and Investigation of Molecular Junctions by Electrochemical Methods**
Z. Yi (2012), 132 pp
ISBN: 978-3-89336-812-9

Band / Volume 23
**Thermal Diffusion in binary Surfactant Systems and Microemulsions**
B. Arlt (2012), 159, xlvi pp
ISBN: 978-3-89336-819-8

Band / Volume 24
**Ultrathin Gold Nanowires - Chemistry, Electrical Characterization and Application to Sense Cellular Biology**
A. Kisner (2012), 176 pp
ISBN: 978-3-89336-824-2

Band / Volume 25
**Interaction between Redox-Based Resistive Switching Mechanisms**
C. R. Hermes (2012), iii, 134 pp
ISBN: 978-3-89336-838-9

Band / Volume 26
**Supported lipid bilayer as a biomimetic platform for neuronal cell culture**
D. Afanasenkau (2013), xiv, 132 pp
ISBN: 978-3-89336-863-1

Band / Volume 27
**15th European Workshop on Metalorganic Vapour Phase Epitaxy (EWMOVPE XV) June 2-5, 2013, Aachen, Germany**
A. Winden (Chair) (2013)
ISBN: 978-3-89336-870-9

Band / Volume 28
**Characterization, integration and reliability of $HfO_2$ and $LaLuO_3$ high-κ/metal gate stacks for CMOS applications**
A. Nichau (2013), xi, 177 pp
ISBN: 978-3-89336-898-3

Band / Volume 29
**The role of defects at functional interfaces between polar and non-polar perovskite oxides**
F. Gunkel (2013), X, 162 pp
ISBN: 978-3-89336-902-7

Band / Volume 30
**Parallelisation potential of image segmentation in hierarchical island structures on hardware-accelerated platforms in real-time applications**
S. Suslov (2013), xiv, 211 pp
ISBN: 978-3-89336-914-0

Band / Volume 31
**Carrier mobility in advanced channel materials using alternative gate dielectrics**
E. Durğun Özben (2014), 111 pp
ISBN: 978-3-89336-941-6

Band / Volume 32
**Electrical characterization of manganite and titanate heterostructures**
A. Herpers (2014), ix, 165 pp
ISBN: 978-3-89336-948-5

Band / Volume 33
**Oxygen transport in thin oxide films at high field strength**
D. Weber (2014), XII, 115 pp
ISBN: 978-3-89336-950-8

Band / Volume 34
**Structure, electronic properties, and interactions of defects in epitaxial GaN layers**
P. H. Weidlich (2014), 139 pp
ISBN: 978-3-89336-951-5

Band / Volume 35
**Defect Engineering of $SrTiO_3$ thin films for resistive switching applications**
S. Wicklein (2014), xi, 145 pp
ISBN: 978-3-89336-963-8

Information / Information
Band / Volume 35
ISBN 978-3-89336-963-8

JÜLICH
FORSCHUNGSZENTRUM